DISSERTATION

CHARACTERISTICS OF CURVILINEAR FLOWS OVER TILTING WEIRS: LABORATORY, COMPUTATIONAL, AND FIELD INVESTIGATIONS

Submitted by
Joseph E. Pugh
Department of Civil & Environmental Engineering

In partial fulfillment of the requirements
For the Degree of Doctor of Philosophy
Colorado State University
Fort Collins, Colorado
Summer 2025

Doctoral Committee:

Advisor: Subhas Karan Venayagamoorthy
Co-Advisor: Timothy K. Gates

Marie Rastello
Jeffrey D. Niemann
Bret C. Windom

ABSTRACT

CHARACTERISTICS OF CURVILINEAR FLOWS OVER TILTING WEIRS: LABORATORY, COMPUTATIONAL, AND FIELD INVESTIGATIONS

The phenomenon of flow over a hydraulic control structure, such as a weir, is a cornerstone of open-channel hydraulics. These structures help regulate water levels in channels and reservoirs, measure discharge, and can even be used as grade control structures to manage channel morphology. The structural configurations that form the basis of centuries of research and application are the vertical sharp-crested weir and the rectangular free overfall. Tilting weirs, which span the range between these classical limits through an adjustable inclination angle, are increasingly being used in engineered systems for stage regulation and more recently, flow measurement. However, current rating methodologies for these structures are limited in scope and overly empirical. Furthermore, a unifying physical framework for the discharge coefficient of weirs that accounts for the constituent aspects influencing discharge characteristics is currently lacking. An investigation of the underlying fluid dynamics, including boundary layer development, flow separation, non-hydrostatic pressure distributions, and local energy loss has thus far seen limited application for weir flows.

Motivated by the need for more accurate and physically interpretable discharge predictions and reliable control of water surface elevations, this dissertation seeks to revisit the classical weir discharge problem under the new light of advanced experimental techniques, apply this knowledge to the general case of the tilting weir, and work to close key knowledge gaps in the application of laboratory-derived rating equations to prototype-scale structures operating in the field. This research combines laboratory experimentation, computational fluid dynamics, and field-scale observations to construct a robust and generalizable framework for understanding the hydraulics of tilting weirs.

Laboratory flume experiments were conducted using high-resolution velocity measurements from particle-image velocimetry (PIV) and acoustic-Doppler velocimetry (ADV), and were complemented by Reynolds-Averaged Navier-Stokes (RANS) computational fluid dynamics (CFD) simulations to examine flow field dynamics in detail across a generous range of flow cases. These efforts informed a new discharge equation for tilting weirs that accounts for the inclination angle of the structure, and was calibrated based upon more than 400 observations of flow over physical models at two unique laboratories. Practical limitations for flow measurement, concerned with scale effects occurring at low inertial states and the transition from weir to sill flow at high inertial states, were examined and accessible measurement recommendations were set forth to enhance accuracy. PIV results in conjunction with computational simulations helped elucidate the underlying fluid dynamics influencing these discharge characteristics. Finally, the laboratory-derived equation was applied to prototype-scale weirs operating within an irrigation system in Northern Colorado and adapted to reflect field-scale variability, such as approach channel conditions and localized energy losses due to flow separation.

The key contributions of this work are as follows. The theoretical framework for the classical weir discharge coefficient (C_d) is revisited and new physical insight is provided by decomposing C_d into its contributing components, which are shown to account for the combined effects of kinetic energy, contraction, and local energy loss and together inform an understanding of C_d as a type of Froude number. Furthermore, a clear delineation of the transition from weir flow to the sill flow which occurs in the limit of the rectangular free overfall, is explained. This transition in regimes of discharge characteristics is analyzed in light of practical constraints for accurate flow measurement, and to inform the rating equation of the tilting weir, which operates within the physical limits of the vertical sharp-crested weir and rectangular free overfall.

A generalized rating equation for tilting weirs is established, incorporating k_θ as an inclination angle correction factor to the head term. This allows for the accurate prediction

of discharge across the full spectrum of inclination angles observed in practice, harmonizing with classical theory at both operational limits. Laboratory results demonstrated consistent accuracy under different experimental configurations. Flow field analysis from experimental PIV and computational simulations revealed that boundary layer separation, turbulent mixing characterized by Reynolds stresses, vertical pressure gradients, and regions of high shear caused by large mean velocity gradients are the major factors influencing the discharge characteristics.

Field application of the tilting weir discharge equation framework, with the addition of the field characteristics correction factor, k_F, showed strong agreement with measured flows, indicating the robustness of the laboratory-derived approach and charting a path forward for future adaptions of lab-derived discharge relationships to field settings. A discussion of the k_F correction factor reveals the viability of physical model experiments of weir flows to accurately capture the governing physics observed in the field, with the need for slight calibration and modification due to site-specific characteristics.

Opportunities for future research include further validation of these results with additional physical models and computational simulations, investigating tilting weir blade characteristics such as curvature and surface roughness on the discharge characteristics to enhance functionality, and leveraging the tilting weir towards ecological goals such as a mechanism for sediment transport management and fish passage. This work advances the theoretical and practical understanding of flow measurement in general and tilting weirs specifically, laying the groundwork for further innovation in water resources engineering.

ACKNOWLEDGEMENTS

The process of completing a doctoral degree can be long and arduous, and the names of those which have supported me along my way these last four years deserve the utmost gratitude and recognition. Without them, this endeavor would have floundered long ago.

Firstly, thank you to Professor Karan Venayagamoorthy, who has been my teacher, mentor, and now trusted friend, over the course of my studies at CSU. His passion, faith in the power of perseverance, drive for excellence, and belief in me have been priceless gifts that I will cherish for a lifetime. I recognize that sound mentorship and an enthusiastic investment in the development of a student's career are by no means guaranteed in a student-advisor relationship. I do not take that blessing for granted, and hope to carry the same level of support I've received into my future mentorship opportunities. In that respect, I was fortunate to have not only one, but two excellent advisors for the duration of my six years of graduate study. Thank you as well to Professor Tim Gates, whose kindness, integrity, love for hydraulics, and brilliant mind both as an educator and engineer have been of immense benefit to me. His keen eye for excellence in research and technical communication have sharpened me immensely. I also thank both of these men of faith for edifying me not only as a researcher, engineer, and educator - but also more holistically as a disciple of Christ.

Thank you to Dr. Marie Rastello and Dr. Céline Berni for hosting me in France for six months in the beginning of 2023, during which major work was completed for Chapters 6 and 7 of this dissertation. This was easily one of the most challenging, yet simultaneously rewarding and growth inducing seasons of my life. The opportunity to live temporarily in a foreign country had always been a dream of mine, and I was fortunate to do it while researching in world-class facilities among some of the warmest and talented people I have met. Professor Jeff Niemann and Professor Bret Windom also were invaluable members of my dissertation committee, serving as a sounding board during my proposal process, and a source of academic rigor during the qualification and final defense portions of my degree. The funding sources for this work: the Colorado Agricultural Experiment Station under grant no. COL00424, and the Chateaubriand Fellowship in STEM are also gratefully acknowledged.

I was also fortunate throughout this process to work alongside some extremely brilliant and good-natured colleagues in the Environmental Fluids Mechanics Laboratory. How glad I am that I had a common research space to come back to each day where I found mutual support, and the occasional but much-needed diversion from research with a coffee break or walk around campus. Most significantly, I would like to thank my friend Dr. Harshit Mishra for his companionship and inspiration throughout this journey. Our tenures at CSU overlapped closely and I feel fortunate to have grown with him over these last six years. We had the fortune of co-chairing the Water and Engineering Science Seminar during the Spring of 2024, which was an accomplishment I am proud to have completed together. Other EFML members who deserve my sincerest acknowledgment are: Dr. Jessica Baker, Dr. Matthew Klema, Dr. Oladapo Aseperi, Joey Sinclair, Daniel Sanchez, Kasun Aluthwalage, Khem Bhattarai, Kiarash Nayeb Pashaei, and Faisal Alsultan. Your friendship and memories of adventures attending the APS-DFD annual meeting I will hold close to my heart for many years to come.

I also have many to thank within the broader Civil and Environmental Engineering Department, especially graduate student advisor Susheela Mallipudi, whose initial email in 2018 put CSU on my radar and eventually got me to Fort Collins. Her continued kindness and service has been a great boon to my graduate experience. I also thank those members of the Environmental and Water Resources Institute student group. Thank you for your companionship through coursework, lending a helping hand with research work, or just unwinding with a beer over happy hour.

Throughout this process, I was also blessed to have a wide support circle. First and foremost, from my family: my parents, Michael and Catherine; and my siblings: Tom, Madeline, and Mary Cate. Thank you for encouraging me in the low times with your prayers and for celebrating with me when long-awaited benchmarks were met. Thank you as well to my close friends throughout this process: Jake and Kaylan Leohr, Cody and Martha Suzor, Jon Fisher, Ryan Benson, Brayden Petersen, Shane Solberg, Aubrey Kruse, and other members of the Citylight Fort Collins Church community - especially those of the Monday night Midtown "city group". These friendships have enriched my life beyond measure and helped me to stay balanced through the course of my studies. The spiritual support and prayers of each of the aforementioned also deserve recognition.

Above all, I thank the triune God revealed to us in Christ Jesus. I thank Him for the unmerited outpouring of grace He has bestowed on my life, and the perseverance and skills necessary to complete this degree. It is unto His Glory and Kingdom that this work is dedicated.

TABLE OF CONTENTS

LIST OF TABLES

LIST OF FIGURES

Chapter 1

Introduction

1.1 Motivation

The flow of water past a static control or check structure in an open channel is one of the most ubiquitous and long-studied phenomena in the world of engineering. This is owed to the direct relevance of this problem towards controlling, diverting, and measuring water flows for the benefit of society. These endeavors help establish flourishing communities through projects related to transportation, irrigation, flood control, and the promotion of ecological health. For many centuries, simple hydraulic structures known as weirs were used as a means of controlling the direction and depth of water flow - such as creating a diversion from a river or a pool for fishing. Due to the scientific revolution and the advancement of a mathematical understanding of fluid flow, in the last three centuries weirs have evolved not only as practical stage-control devices, but into dual-purpose mechanisms that additionally allow for estimations of flow for water measurement. The tilting weir is a type of weir that represents a translational case between two limiting classical structures: the vertical sharp-crested weir and rectangular free overfall. The structure can be inclined to various degrees with respect to the horizontal in response to changing needs in the upstream water depth - making them especially effective as gates on dam spillways, or flood control structures in channels. Over the past several decades the tilting weir has also been developed as a flow measurement device, although a robust understanding of the effect of the tilting weir inclination on the flow dynamics is lacking and current methodologies result in prediction of the flow to only ± 10% (Wahlin and Replogle, 1994; Zeng et al., 2019). It also remains to be seen what considerations must be taken when applying lab-derived relationships for use in the field. Furthermore, an in-depth understanding of the important physical mechanisms which influence the discharge characteristics is lacking. Investigation into these aspects of the tilting weir represents the central goal of this dissertation, with the broader goal being to promote more equitable and reliable water management and the advancement of new hydraulic structures that meet 21st century design needs.

1.2 Background

In the most basic sense, a weir can be defined as any nominally rectangular object placed within the cross-section of a channel that represents some obstruction to the flow path of a fluid. (Rao, 1975). Over the centuries, there have been numerous iterations and modifications to this basic design of a weir. For the purpose of this dissertation, the primary focus will be on two limiting cases that represent some of the simplest and most widely implemented types of weirs.

First, the sharp-crested weir, which is the simplest and oldest type of weir consisting of a thin flat plate situated perpendicular to the direction of flow (see Figure 1.1). The second limiting case is the rectangular free overfall, which is akin to a weir of zero height

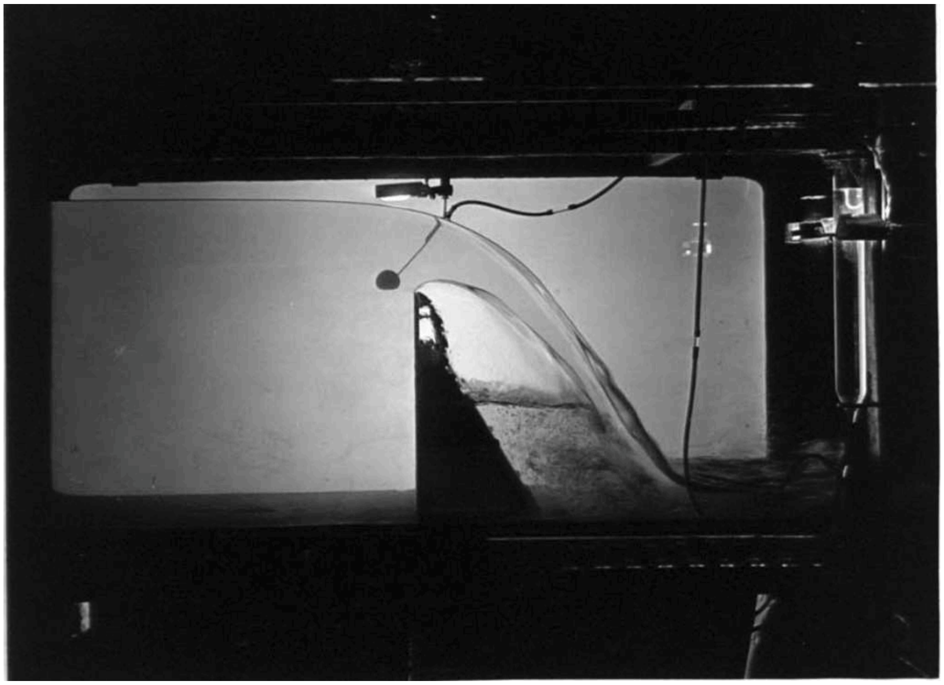

Figure 1.1: Sharp-crested weir at Massachusetts Institute of Technology laboratory, discharging 125 L/s/m. Photo courtesy of Rouse (1932).

(see Figure 1.2). In practice, this represents an abrupt perpendicular drop where the issuing jet is supported only by atmospheric pressure. Weirs of very low height, approaching the free overfall limit, are also sometimes referred to as sills. The discharge characteristics for flow over sills are slightly different than that for classical weirs where the height of the obstacle is at least the same order of magnitude as the flow depth, and the transition between weir-type and sill-type discharge characteristics is one of the questions addressed in this dissertation.

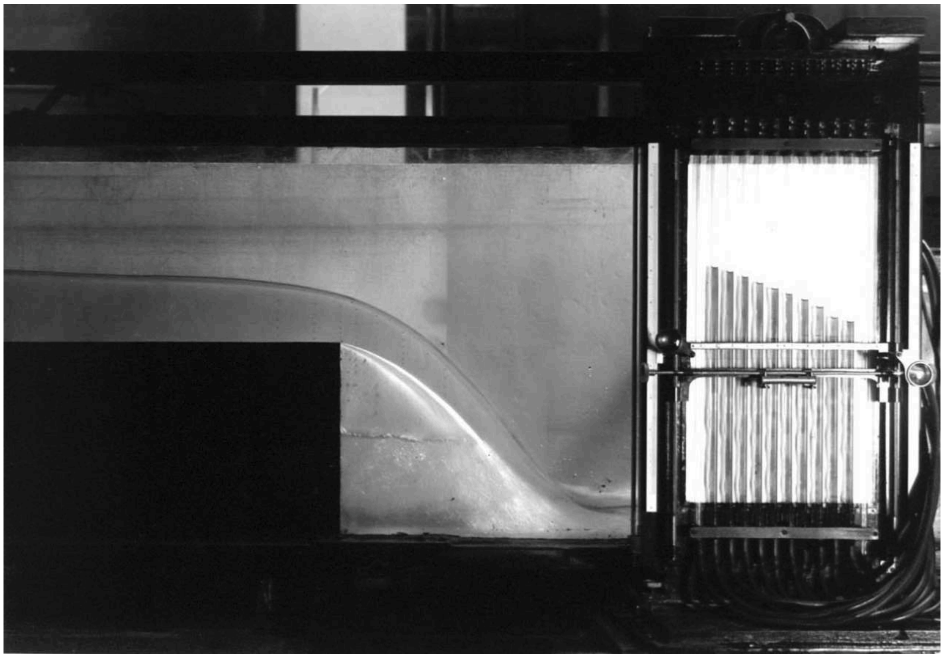

Figure 1.2: Ventilated rectangular free overfall discharging 125 L/s/m, courtesy of Rouse (1932).

The tilting weir (also referred to as a pivot weir or an overshot gate in the literature) can be thought of as a single structure that operates in the range between the two limiting cases of the sharp-crested weir and free overfall. Here, the inclination angle of the tilting weir with respect to the horizontal channel bed is given by θ. When $\theta = 90°$, the tilting weir is a sharp-crested weir. When $\theta = 0°$ the tilting weir is a free overfall. Tilting weirs are a relatively novel type of hydraulic structure developed in the late twentieth century and are now used for a myriad of purposes concerning the management of water levels in engineered systems; from flood control, ecosystem services, irrigation, water storage, and diversion. For irrigation systems in particular, tilting weirs were first implemented to be a more reliable and efficient replacement for older check structures, such as stop-log checks or sluice gates (Stringam and Gill, 2012). They can also reduce the required response time water managers must have when adapting to dynamic conditions, such as those caused by a flood event.

1.3 Objectives

This dissertation research aims to utilize a combination of results garnered from laboratory experimentation on scaled physical models, computational fluid dynamics simulations, and field-scale observations to study the fundamental nature of the flow over tilting weirs as it relates to the following objectives:

1. **Clarify the physical meaning of the discharge coefficient** for weir-type flows using dimensional analysis, decompose it into constituent flow parameters, and quantify their magnitude from flow field observations to identify the dominant mechanisms that govern flow behavior over weirs. Provide further insight on the transition between weir and sill flows.

2. **Extend the classical weir rating equation to apply to tilting weirs.** Define a correction factor to the weir discharge coefficient that is a function of the inclination angle of the weir, and determine the proper operating parameters that avoid scale and aeration effects to ensure optimal measurement accuracy.

3. **Characterize the underlying flow dynamics that influence tilting weir discharge behavior**, including boundary layer growth, shear stress development, vertical pressure gradients, and regions of flow separation and energy dissipation, using a combination of high-resolution laboratory measurements and Reynolds-Averaged Navier-Stokes (RANS) simulations.

4. **Bridge the gap between laboratory research and field implementation** by evaluating the applicability of the proposed tilting weir discharge equation to prototype-

scale hydraulic structures. Define a secondary correction factor to account for field-scale variability, including channel geometry, approach flow non-uniformity, and imperfect nappe aeration.

1.4 Dissertation Layout

The remainder of this dissertation is laid out in the following chapters:

- Chapter 2 lays a foundation of the fundamental mathematical principles relevant for understanding the problem of flow over tilting weirs.
- Chapter 3 presents background information on curvilinear free-surface flows over weirs, and a broad overview of the types of research questions previously investigated concerning the topic.
- Chapter 4 details the experimental facilities and measurement techniques, numerical methods, and field-scale observation capabilities utilized in this work.
- Chapter 5 Presents a re-examination of the weir discharge coefficient as it is classically understood, including its derivation, first and second-order influences on its behavior, and practical operational regimes for vertical sharp-crested weirs.
- Chapter 6 Develops a discharge equation for tilting weir flow and provides an understanding of how it relates to the classical rating equation for a sharp-crested weir.
- Chapter 7 Examines aspects of the underlying flow field dynamics influencing the discharge characteristics of tilting weirs.
- Chapter 8 Applies the lab-derived discharge equation for tilting weirs to prototype-scale structures for practical use in the field.
- Chapter 9 Summarizes the major findings of this dissertation and discusses avenues for future research.

Chapter 2

Governing Equations

This chapter presents the fundamental mathematical equations governing the flow of fluids. These equations form the basis from which all subsequent analyses of tilting weir flow in this dissertation will be made, and provide context for the research questions discussed in Chapter 3. The exact solution of the governing equations presented here is possible in theory. However, the richness of time and spatial scales present in practical turbulent flows necessitates simplifying assumptions and numerical approximations, which are also discussed in this chapter.

2.1 Fundamental Frameworks for Analysis

A fluid can be thought of as a large number of well-packed molecules undergoing constant collisions (Kundu et al., 2016), and can therefore in the most discrete sense be analyzed by classical Newtonian mechanics at the microscopic level. However, at least for engineers, it is impractical to study the motion of individual particles. Therefore, an assumption about the nature of fluid motion, called the continuum hypothesis, is made. This principle states that, if the region of interest of fluid motion is large enough and the molecular density is great enough, then average quantities concerning the properties of individual fluid molecules within the continuum are sufficient to describe the macroscopic properties of the motion. One such property that is of great importance to the problem of analyzing flow over hydraulic structures is the fluid velocity.

This vector quantity is a first-order tensor, having both magnitude and direction in three dimensions (see Figure 2.1). Knowledge of velocity is crucial in determining the volumetric flow rate (i.e., discharge) over a hydraulic structure. When the discharge and all other channel characteristics are held constant, the relative magnitude of velocity in an open channel is inversely related to the cross-sectional area occupied by the flow. In Cartesian

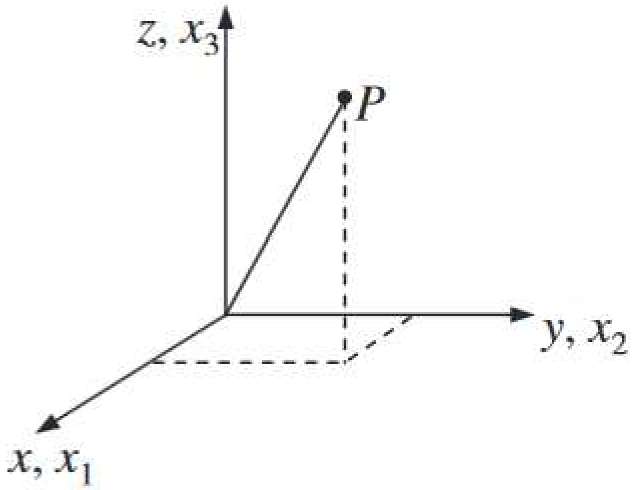

Figure 2.1: The Cartesian coordinate system used in this text, where P is located by the coordinate triplet (x,y,z) or (x_1,x_2,x_3). From Kundu et al. (2016)

coordinates, the fluid velocity has three components which can be defined for any point in space within the fluid, as well as any point in time.

$$\mathbf{u}(\mathbf{x},\mathbf{t}) = u_i = u\hat{\mathbf{i}} + v\hat{\mathbf{j}} + w\hat{\mathbf{k}}\,. \tag{2.1}$$

Here, i represents the repeating index in the Einstein-summation (or indical) notation convention. In a Cartesian system, i can be one of three indices (i.e., $i = 1, 2, 3$). Furthermore, for flow through an open channel we take u to be the fluid velocity in the stream-wise x-direction, v to be that in the transversal y-direction, and w to be that in the vertical z-direction. This convention will be used consistently throughout this work.

There are two approaches for studying aspects of fluid motion. The first, a Lagrangian approach, tracks the properties of an individual fluid particle (or continuum) as it moves through space and time. Many of the fundamental mathematical principles governing fluid flow are most elegantly expressed using this framework, but it is less practical to use as it requires a moving frame of reference. More realistically, practicing hydraulicians take an Eulerian approach. Here, fluid motion is analyzed as it passes through a fixed control volume. Rather than tracking individual fluid particles, the Eulerian approach is concerned with how macroscopic fluid properties such as pressure, velocity, and density change through time and within the spatial bounds of the control volume. The Reynolds Transport Theorem allows for a translation between the Lagrangian and Eulerian approaches. For a discrete and continuously deformable differential volume of fluid:

$$\frac{D\mathbf{B_{sys}}}{Dt} = \frac{d}{dt}\int_{V_*(t)} \rho\beta dV = \int_{V^*(t)} \frac{\partial(\rho\beta)}{\partial t} dV + \int_{A^*(t)} \rho\beta(\mathbf{u}\cdot\hat{\mathbf{n}})dA\,. \tag{2.2}$$

Here, β is the generic, intensive (i.e., per unit mass) property of some system quantity $\mathbf{B}$, ρ is the fluid density, $\mathbf{u}$ is a first-order tensor representing the velocity along the boundary of the system, and $\hat{\mathbf{n}}$ is the unit normal vector, which acts perpendicular to and outward from the control surfaces ($A^*(t)$) of the control volume ($V^*(t)$) that is coincident with the boundaries of the system. For a fixed control volume, Eq. (2.2) states mathematically that the material derivative (D/Dt) measuring the rate of change of some extensive quantity $\mathbf{B}$ within a system can be defined as the sum of the time rate of change of that quantity within the control volume, and the net flux of that quantity through non-deformable control surfaces. A re-writing of Eq. (2.2) using a Lagrangian perspective can be achieved with the Gauss divergence theorem and assuming an infinitesimal system volume:

$$\frac{D\mathbf{B_{sys}}}{Dt} = \frac{\partial(\rho\beta)}{\partial t} + \nabla\cdot(\rho\beta\mathbf{u}). \tag{2.3}$$

Eq. (2.3) is known as the definition of the total, or material, derivative.

2.2 Conservation Laws

2.2.1 Conservation of Mass

Mass is the first property of interest concerning an understanding of fluid motion. Here, the intensive parameter in Eq. (2.3) is $\beta = 1$ so that:

$$\frac{\partial\rho}{\partial t} + \nabla\cdot(\rho\mathbf{u}) = 0\,. \tag{2.4}$$

The right-hand side of Eq. (2.4) is 0 because the law of mass conservations states that the total amount of mass within a closed system must remain constant over time. Therefore, the material change in density within the control volume will be equal and opposite to the net flux of mass through the control surfaces.

2.2.2 Conservation of Momentum

The principle governing the conservation of momentum for fluid motion is Newton's second law, which states that the net sum of forces acting on a system will be equal to the time rate of change in the momentum of that system (i.e., $\mathbf{F} = m\mathbf{a}$). In the integral form of Eq. (2.2) with $\beta = \mathbf{u}$, Newton's second law can be written as:

$$\begin{aligned}\frac{D\rho\mathbf{u}}{Dt} = \frac{\partial}{\partial t}\int_{V^*(t)} \mathbf{u}\rho dV + \int_{A^*(t)} \mathbf{u}\rho(\mathbf{u}\cdot\hat{\mathbf{n}})dA = \\ -\int_{A^*(t)} P\hat{\mathbf{n}}dA + \int_{V^*(t)} \rho\mathbf{g}dV + \int_{A^*(t)} \hat{\mathbf{n}}\cdot\tau_{ij}dA\,. \quad (2.5)\end{aligned}$$

Here, the three terms on the right-hand side of the equation correspond to the forces contributing to a change in the momentum of the fluid system. They are: pressure (P), body forces ($\mathbf{g}$), and viscous shear (τ_{ij}). Pressure and viscous shear are surface forces, acting as normal and tangential stresses, respectively, integrated over an area. The body forces act through the center of mass of the control volume without physical contact, arising from gravitational or electromagnetic force fields (Kundu et al., 2016). Fictitious body forces, such as the Coriolis force, can also arise in accelerating or rotating frames of reference. For the class of flows examined in this dissertation, we will assume the only relevant body force is gravity, acting in the negative z-direction, where the z-axis points vertically upward (i.e., $\mathbf{g} = -g\hat{\mathbf{k}}$) and g is the coefficient of gravitational acceleration, 9.81 m/s^2.

Considering a differential volume of fluid and applying the Gauss divergence theorem, the conservation of momentum equation can be written per unit volume as:

$$\rho \frac{D\mathbf{u}}{Dt} = -\nabla P + \rho\mathbf{g} + \nabla \cdot \tau_{ij} \; . \tag{2.6}$$

Together, Eqns. (2.4) and (2.6) represent a system of four equations for which there are ten unknowns (if ρ is assumed constant). The symmetric viscous strain rate tensor (τ_{ij}) consists of six unknowns (i.e., $\tau_{ij} = \tau_{ji}$), and there are three unknown components of the velocity field ($\mathbf{u}$), in addition to the unresolved pressure field (P). The imbalance in the number of unknown quantities and available equations to solve the resulting system of equations creates a closure problem. Because of this, it is necessary to relate τ_{ij} to the velocity field using Stokes' hypothesis, which assumes a linear relationship between viscous stress and strain for a Newtonian fluid. This allows us to define the constitutive relationship:

$$\tau_{ij} \equiv 2\mu S_{ij} \; , \tag{2.7}$$

where $S_{ij} = \frac{1}{2}\left(\frac{\partial u_i}{\partial x_j} + \frac{\partial u_j}{\partial x_i}\right)$ is the strain rate tensor and μ is the dynamic viscosity of the fluid. For the class of flows in this dissertation, we will assume that the fluid of interest (i.e., water) is incompressible, so that Eq. (2.4) can be re-written as:

$$\frac{\partial \rho}{\partial t} + \mathbf{u} \cdot \nabla \rho = 0 \; . \tag{2.8}$$

Eq. (2.8) states that the fluid density will remain constant with changes in the pressure field. We will further assume that temperature and salinity effects are negligible within our control volume, so that the fluid density across the entire flow field can be assumed constant. Substitution of Eq. (2.7) into Eq. (2.6) yields the well-known Navier-Stokes momentum equations for incompressible fluids.

$$\rho \frac{D\mathbf{u}}{Dt} = -\nabla P + \rho\mathbf{g} + \mu \nabla^2 \mathbf{u} \; , \tag{2.9}$$

and Eq. (2.8) becomes:

$$\nabla \cdot \mathbf{u} = 0\,. \tag{2.10}$$

Together, Eqns. (2.9) and (2.10) allow for a complete description of motion for incompressible Newtonian flows of nearly constant viscosity. Furthermore, if viscous effects are negligible, which is commonly taken to be true in exterior flows away from solid boundaries (such as the case of weir flows), then Eq. (2.9) can be further simplified to the inviscid Euler equations:

$$\rho \frac{D\mathbf{u}}{Dt} = -\nabla P + \rho \mathbf{g}\,. \tag{2.11}$$

2.3 Reynolds Decomposition

In theory, Eqns. (2.9) and (2.10) offer a full description of the fluid velocity and pressure field at any point in the four dimensions of space and time. However, translating the mathematical equations of fluid flow into numerical approximations by discretizing Eqns. (2.9) and (2.10) becomes a challenging task due to the wide disparity of the length and time scales present in practical turbulent flows. The computational cost required to resolve the flow field at each and every time step and across all spatial domains becomes exponentially larger as the geometric scale and inertia of the flow of interest grow. This issue necessitates a decomposition of the turbulent flow field into mean and fluctuating quantities for all but very weakly turbulent cases. Using indical notation for the first-order velocity tensor u_i, the Reynolds decomposition of the velocity and pressure field is:

$$u_i(x,t) = \langle U_i(x,t) \rangle + u_i'(x,t)\,, \tag{2.12}$$

$$P(x,t) = \langle P(x,t) \rangle + P'(x,t)\,, \tag{2.13}$$

where the term on the left-hand side of the equation is the instantaneous field quantity at any position x_i or time t. The brackets $\langle\rangle$ indicate temporal averaging for a point in space, and u_i', P' are the fluctuating (i.e., turbulent) velocity and pressure.

Substituting these decomposed quantities into the instantaneous Navier-Stokes equations (Eqns. (2.9) and (2.10)) yields the Reynolds-Averaged Navier-Stokes (RANS) equations in summation notation:

$$\rho_0 \frac{D\langle U_i\rangle}{Dt} = -\frac{\partial \langle P\rangle}{\partial x_i} - \rho_0 g \delta_{i3} + \frac{\partial}{\partial x_j}\left[\mu \frac{\partial \langle U_i\rangle}{\partial x_j} - \rho_0 \langle u_i' u_j'\rangle\right] , \tag{2.14}$$

subject to the continuity constraint:

$$\frac{\partial \langle U_i\rangle}{\partial x_i} = 0 \, . \tag{2.15}$$

In Eq. (2.14) we have defined a constant reference density, ρ_0 under the assumption of negligible temperature and salinity effects. For incompressible flows, the instantaneous, mean, and fluctuating velocity fields all remain divergence-free. The Kronecker delta (δ_{ij}) is used to indicate that the gravitational body force acts only in the negative z-direction. It can also be seen that Eq. (2.14) appears as the direct analog to Eq. (2.9), with the addition of the turbulent fluctuation term $-\rho_0\langle u_i' u_j'\rangle$, called the Reynolds stress tensor. These are apparent stresses, in the sense that they do not represent any additional physical mechanism that is not represented in Eq. (2.9), but rather are a mathematical result of the Reynolds decomposition procedure. This tensor can be thought of as the stress experienced by the mean flow as a result of momentum transfer by turbulent fluctuations. In turbulent flows, Reynolds stresses are often much larger than viscous stresses, except very close to the wall where the turbulent fluctuations go to zero and mean-flow gradients dominate. The Reynolds stress tensor is symmetric, containing six independent Cartesian components. The diagonal components are normal stresses that augment the mean pressure, while the off-diagonal components act as shearing stresses (Kundu et al., 2016). Unfortunately, the Reynolds decomposition of the Navier-Stokes equations results in six new unknown quantities comprising the Reynolds stress term in Eq. (2.14). This creates the infamous turbulence closure problem for solving the RANS equations. Therefore, the Reynolds stresses must be parameterized to make the turbulence closure problem tractable. These methods will be further discussed in Chapter 4.

2.4 Turbulent Kinetic Energy Budget

Inherent to an understanding of the parameterization of the Reynolds stress terms is the turbulent kinetic energy (TKE) budget. TKE is defined as half the trace of the Reynolds stress tensor: $k = \frac{1}{2}\langle u_i' u_i' \rangle$. As will be shown in Chapter 4, these parameterizations rely on an approximation of the diffusive nature of turbulent transport as being analogous to molecular diffusion. Further motivation for understanding the TKE budget is given by the need of hydraulic engineers to understand the mechanisms for dissipation of kinetic energy by hydraulic structures to protect critical infrastructure and understand the potential for power generation and improved energy efficiency. The process of TKE transport in turbulent flows involves the loss of kinetic energy by the mean flow to the fluctuating turbulent field through the process of shear stresses, which was initially described by Richardson (1922). In other words, the dissipation term of kinetic energy for the mean field is analogous to the kinetic energy production term for the turbulent field. The process of TKE transport and dissipation can then be explained by the turbulent energy cascade. Here, the largest eddies in a system, defined by the boundary geometry, contain the most energy. This energy is then transported down through smaller and smaller eddies though an intermediate scale called the inertial sub-range. Finally, TKE is irreversibly dissipated into internal heat through the action of viscosity at the smallest (i.e., molecular) spatial and time scales, which are referred to as the Kolmogorov scales after their initial conception by Kolmogorov et al. (1941). The spatial scale of the smallest eddies in a turbulent flow is defined by:

$$\eta \equiv \left(\frac{\nu^3}{\varepsilon} \right)^{1/4} , \tag{2.16}$$

where η is the Kolmogorov length scale, ν is the fluid kinematic viscosity ($\nu = \mu/\rho$), and ε is the TKE dissipation rate with dimensions of [$\mathrm{L}^2\mathrm{T}^{-3}$]. Neglecting the presence of temperature fluctuations, the production, transport, and dissipation of TKE is defined by:

$$\frac{Dk}{Dt} = \frac{\partial k}{\partial t} + \langle U_j \rangle \frac{\partial k}{\partial x_j} = \mathcal{T} + \mathcal{P} - \varepsilon \,, \tag{2.17}$$

where $\mathcal{T}$, $\mathcal{P}$, and ε are the respective transport, production, and dissipation terms defined by:

$$\mathcal{T} \equiv -\frac{\partial}{\partial x_j} \left[\frac{1}{\rho_0} \langle P' u_j' \rangle + \langle k u_j' \rangle - 2\nu \langle u_i' s_{ij}' \rangle \right] \,, \tag{2.18}$$

$$\mathcal{P} \equiv -\langle u_i' u_j' \rangle \frac{\partial \langle U_i \rangle}{\partial x_j} \,, \tag{2.19}$$

$$\varepsilon \equiv 2\nu \langle s_{ij}' s_{ij}' \rangle \,, \tag{2.20}$$

and $s_{ij}' = \frac{1}{2}\left(\frac{\partial u_i'}{\partial x_j} + \frac{\partial u_j'}{\partial x_i}\right)$ is the fluctuating strain rate tensor. The three terms within the brackets of the transport term represent the transport of k through the respective processes of pressure fluctuations, turbulent stresses, and viscous diffusion. (Kundu et al., 2016). As previously mentioned, the equation for $\mathcal{P}$ is given by the shear-production term, representing the loss of kinetic energy by the mean flow field to the turbulent (i.e., fluctuating) field, and ε is the irreversible conversion of TKE into internal heat.

Chapter 3

Literature Review

3.1 Curvilinear Flow Over Weirs

3.1.1 Basics of Open-Channel Flow

A discussion of weir flows must necessarily begin with an understanding of the broader class of flows within which weirs are a type - that being open-channel flow. These types are flows are by strict definition two-phase, in the sense that they feature the interaction between two fluids: air and water. However, the primary concern of this dissertation will be for flows where little mixing occurs between the two fluids, and a distinct separation between air and water is present in the form of the free-surface with an atmospheric boundary condition. For this reason, weir flow can be treated as a single-phase phenomenon. However, fascinating multi-phase flow phenomena are present in open-channels, such as hydraulic jumps, flow down stepped-spillways, and cavitation in non-pressurized diversion tubes.

The types of flow observed in open channels can be generally described as either gradually-varied or rapidly-varied. Gradually-varied flow (GVF) occurs over long reaches of open channels where the rate of change in flow depth with respect to the longitudinal direction is small. In GVF, the streamlines are nominally horizontal so that the pressure distribution within the fluid column can be well-approximated to be hydrostatic. This allows for a decoupling of the elliptic pressure term from the velocity terms in the partial differential Navier-Stokes equations (Eqns. (2.9) and (2.10)), so that the velocity field can be solved for independently of the simplified pressure field (i.e., $dP/dz = -\rho g$).

The analytical solution for gradually-varied flow invokes the work-energy principle of mechanics (i.e., first law of Thermodynamics), which states that for an isothermal system, the work done by component forces acting on a fluid volume must be equal to the rate of change of internal energy within the control volume. An equation describing this law can be essentially derived by multiplying the equation for conservation of momentum (see Eq. (2.9)) by the flow velocity $\mathbf{u}$. For GVF, the assumption is made that the flow is steady, one-dimensional, and hydrostatic - so that the following equation can be accurately used as a description of the work-energy principle:

$$\frac{dH}{dx} = -S_f \ , \tag{3.1}$$

where

$$H = \alpha \frac{U_0^2}{2g} + D \cos \Theta + z_b \ . \tag{3.2}$$

Eq. (3.2) has dimensions of length (L), or energy per unit weight of fluid. Here, H is referred to as the total hydraulic head, U_0 is the cross-section averaged streamwise velocity, α is the kinetic energy correction factor (accounting for non-uniform distributions of the velocity head), D is the flow depth, Θ is the angle of the channel bed with respect to the horizontal, and z_b is the bed elevation above a reference datum. S_f is the friction slope, representing the resistance to fluid motion in the channel caused by viscous shearing forces occurring at the boundaries and is defined as $S_f \equiv \tau_b/\gamma R$, where τ_b is the shearing stress exhibited on the fluid by the boundary, γ is the specific weight of the fluid, and R is the hydraulic radius (Jain, 2001). In practice, the friction slope is often estimated using the uniform flow formulas of Manning-Strickler or Chézy (Julien, 2018).

Another important parameter used for describing open-channel flows is the specific energy (E), defined as the sum of the pressure and kinetic energy head terms for steady, 1D flows:

$$E = D \cos \Theta + \alpha \frac{U_0^2}{2g} \ . \tag{3.3}$$

Crucial to an understanding of open-channel flow transitions is the concept of the critical energy state, which occurs when the specific energy is at a minimum (E_c). For any given condition of specific energy, there exist two alternate depths that the flow can occupy (see

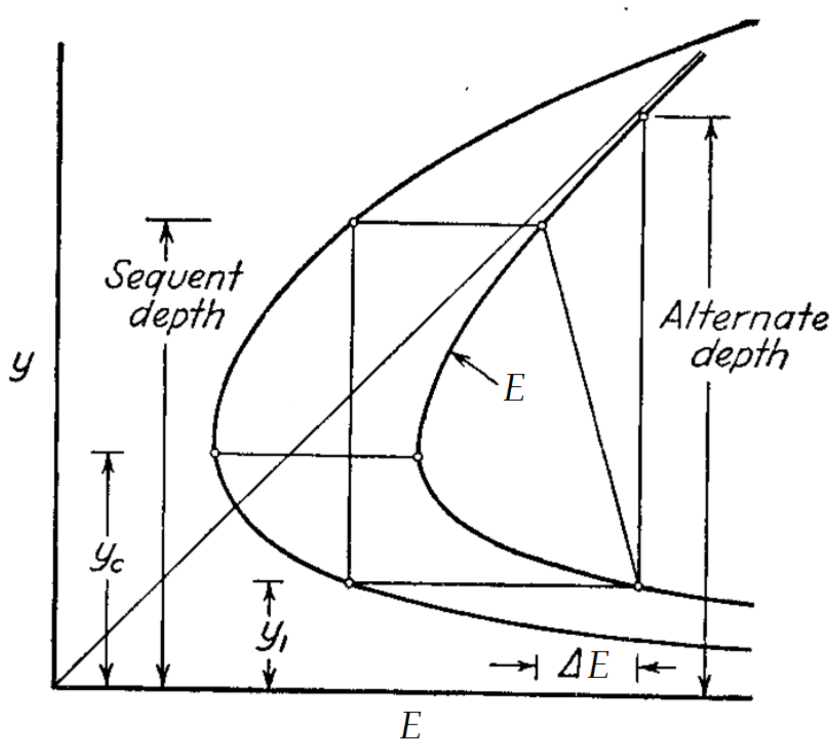

Figure 3.1: Specific energy diagram, courtesy of Ippen (1950).

Figure 3.1). The separation between these two states of flow is given by the dimensionless Froude number (Fr). Fr represents the ratio of inertial effects to gravitational effects in open-channel flows.

$$Fr = \frac{U_0}{\sqrt{gD}} \,. \tag{3.4}$$

Here, D is the hydraulic depth, defined as the cross-sectional area of the flow (A) divided by the channel top-width (T_w). $\sqrt{gD}$ is known as the speed of surface waves, or celerity. Subcritical flow occurs when $Fr < 1$ and represents the condition when the inertial effects of the flow are dominated by gravitational effects. Subcritical flow, generally speaking, is slower moving, deep, and does not feature many surface fluctuations. Supercritical flow occurs when $Fr > 1$ and the inertial effects of the flow dominate the gravitational effects. Supercritical flows are shallow and faster moving, featuring many fluctuations in the free surface caused by waves.

3.1.2 Curvilinear Rapidly-Varied Flow

A much more difficult case to solve for analytically is that of rapidly-varied flow (RVF). Changes to the flow depth are abrupt in RVF, and a discontinuity in the free surface may exist - as in the case of the hydraulic jump where the flow transitions from supercritical to subcritical. RVF occurs at sharp transitions in the channel geometry, such as channel width constrictions or expansions, or the introduction of steps. The flow over a weir is also an instance of RVF. Under these circumstances, significant curvature is present in the streamlines as the flow navigates the channel transition, so that the pressure distribution no longer is hydrostatic. This reduction in the pressure head from the hydrostatic condition is paired with an acceleration of the flow around the obstacle, and a transition from subcritical to supercritical flow occurs.

3.2 Weirs as Flow Measurement Devices

Since weirs constrict the flow path of the fluid, causing the flow to transition from subcritical to supercritical, they are referred to as artificial channel controls. This feature was realized by early pioneers in the field of hydraulics so that the weir could be developed beyond a stage control structure and also as a flow measurement device. If the obstructive effect of the weir is large enough to create a stagnation point on the upstream side of the obstacle, the weir will act as an artificial channel control because the depth of flow upstream of the weir will be directly proportional to the discharge passing over the structure. This depth-discharge relationship is beneficial to the hydraulician because the subcritical nature of the flow upstream of the weir is conducive to accurate depth measurement. In the development of a theoretically sound depth-discharge relationship, the knowledge of a transition in the flow criticality can be utilized in one of two ways. If the location of the critical section is known and fixed, then mathematical relationships can be derived to calculate the discharge at the critical section. This is the fundamental theory utilized in the flow rating equation of a free overfall, broad-crested weirs, and long-throated flumes (Bos et al., 1984;

Wahl et al., 2005). However, for the case of the sharp-crested weir, the flow does transition from subcritical to supercritical, but the location of the critical section is not known *a priori* and can change location based upon the flow condition. Here the critical section is the point where the lower nappe surface profile reaches its maximum elevation (Rouse, 1932), and this location will change based upon the weir geometry and discharge conditions. Because of this, a different theoretical basis is needed to elucidate the sharp-crested weir as a flow measurement device.

Flow over sharp-crested weirs represents a case of curvilinear rapidly-varied flow where significant vertical inertia is present, causing the pressure distribution to become non-hydrostatic. The complex nature of the coupled pressure and velocity field present for rapidly-varied flow requires several simplifying assumptions to be made in order to practically implement the sharp-crested weir as a flow measurement device. The fundamental theory that governs these flow-rating equations relies on the knowledge that the flow transitions from subcritical to supercritical in the vicinity of the weir crest, and that over short channel reaches the flow can be approximated as being inviscid and irrotational. Under these considerations, the sharp-crested weir is treated similar to a free jet issuing from a sharp-edged orifice supplied by a large static reservoir of potential energy, and the Torricelli principle is leveraged to obtain an estimation of volumetric discharge over the weir. This approach is further discussed in Chapter 5.

Due to the convergent nature of the flow field and the assumed negligibility of the viscous boundary layer on the overall flow characteristics, the weir flow problem has been well-positioned for study using inviscid flow theory. In that case, the application of numerical approximations to this problem is beneficial because without needing to incorporate a turbulence model, the flow pattern over the weir can be solved to a high degree of accuracy as long as viscous boundary layer effects are of an order of small magnitude. Significant work taking this approach has been completed to analyze the flow field over classical structures such as the sharp-crested weir and free overfall (McNown et al., 1955; Strelkoff, 1962;

Clarke, 1965; Ali and Sykes, 1972). Recent advances have applied more efficient numerical methods to investigate the flow fields of different types of weirs, such as the tilting weir (Castro-Orgaz and Hager, 2017; Zerihun, 2022). However, since both the sharp-crested and free overfall have primarily been of interest to engineers due to their practical application as a flow measurement structure, the vast majority of recent studies on the topic has focused not on detailed analyses of the flow field, but rather on using a simplified weir discharge equation for a broad category of weirs, and making the necessary empirical adjustments as complexities arise due to differences in weir characteristics, channel conditions, and fluid properties.

3.3 Factors Influencing Weir Flow

The factors affecting the flow over weirs were organized by Rao (1975) into four broad general categories: i) Flow Conditions, ii) Channel Characteristics, iii) Fluid Properties, and iv) Weir Characteristics. We will discuss each here systematically in the following sections.

3.3.1 Flow Conditions

The study of weir flow has thus far been primarily focused on laboratory experimentation to determine the discharge characteristics of certain types of structures under variable geometries and flow conditions. Primarily, hydraulicians have focused their analyses on mean flow properties, such as the discharge coefficient, and to a lesser extent, profiles of mean velocity and pressure distributions. Of primary importance has been the quest to define the empirical relationship between the discharge coefficient over the weir crest and the inertia of the flow. It has long been recognized that the velocity head in the approach channel, itself a quantification of the flow inertia, plays a significant effect in the rating equation of weirs (Engel and Stainsby, 1958). The initial pursuit of researchers on the sharp-crested weir was to define an empirical relationship between the discharge coefficient and some measurement of the flow inertia, often given by the ratio h/p.

A profound amount of work on developing a discharge formula for the sharp-crested weir was completed throughout the nineteenth century and is well summarized by Horton (1906). Much of this work was completed in French and German, and so its significance is often obscured to English-speaking audiences. One of the most well-known of these works is that of Bazin (1898), who examined a wide variety of phenomena concerning flow over weirs: the discharge formula, the shape of the nappe profile, the effect of inclining the weir plate, spillway design, and velocity and pressure measurements made internal to the nappe. These early and extremely detailed experiments, completed over the course of nearly a decade, laid the foundation for much future work on weirs.

As the results of early European pioneers were translated into English, many researchers in the United States made subsequent observations on this discharge characteristics of the sharp-crested weir in the years following Bazin (1898). This great proliferation of research on the topic created some disagreement within the literature as to which discharge-rating approach was most appropriate. The study of Schoder and Turner (1929) represented a seminal contribution to this discussion. The authors collected much new data, including measurements of the velocity profile in the approach section. This publication generated a productive discussion piece on the topic that featured the opinions of some of the most well-renowned hydraulicians of the day. One formula proposed in the discussion section that has proved its enduring power over other approaches is that of Theodor Rehbock of the Karlsruhe Institute of Technology in Germany. Rehbock published the majority of his work in German, but presented a summary of his findings in English in the discussion piece, King et al. (1929), published by the American Society of Civil Engineers. The formula of Rehbock published in King et al. (1929) is likely to be found as the standard weir equation in today's fluid mechanics and hydraulics textbooks, likely because it was verified by the experiments of Rouse (1932) and Kandaswamy and Rouse (1957). Rouse published several textbooks on the topic in his career, many of which have gone on to be the foundational material for today's textbooks (Rouse, 1938, 1946b).

Returning to a discussion of the other limiting case for the tilting weir, the seminal study on the free overfall discharge equation was also performed by (Rouse, 1936). In this study, Rouse showed that for smooth rectangular channels, the end-to-depth ratio would be a constant value, since the critical depth is always known to be at the crest of the overfall. From this study, the discharge coefficient for a zero-height weir (i.e., free overfall) was found from theory, and confirmed by experiment, to be 0.715. Other experimenters have confirmed the initial result of Rouse (1936), showing that it only deviates from a constant value under especially low heads, where scale effects are present (Rajaratnam and Muralidhar, 1968; Hager, 1983).

For tilting weirs, much preliminary work was done as early on as Bazin (1898), who found that if the standard vertical sharp-crested weir is tilted downstream, the discharge capacity is increased systematically. Bazin hypothesized that a constant amplification factor could be applied to the discharge coefficient of a sharp-crested weir to account for the effect of the inclination angle. This indicates that for the tilting weir, the same discharge can pass at a lower head if the weir is tilting downstream. Bazin (1898) reported that the maximum value of this amplification occurred at an inclination angle of 30°. Beyond this threshold value, at least for tilting weirs located in the mid-section of a channel reach (rather than at the end of a channel), the tilting weir was no longer able to function as a free-flowing device due to the influence of the tailwater on the pressure condition at the crest. A more thorough study on the topic wasn't carried out until a century later by Wahlin and Replogle (1994), who utilized a correction factor for the discharge coefficient of the vertical sharp-crested weir to account for the effect of the inclination angle.

3.3.2 Channel Conditions

The resistance to fluid motion caused by roughness elements along the channel boundary is known to be an important factor in developing a full understanding of open-channel flows. However, very little research has been completed to understand how the empirically calibrated discharge equations for weir flow, developed in laboratory flumes with smooth channel boundaries, translate to more realistic environments with channel boundaries that have irregular geometries and variable roughness.

In their seminal paper, Schoder and Turner (1929) utilized a complex system of baffles to examine the effect that a nonuniform velocity distribution had on the discharge coefficient for sharp-crested weir flow. They saw that extreme variations from a uniform velocity distribution in the approach channel could result in deviations from the predicted discharge condition by as much as 26%. The authors developed an empirical equation to predict the discharge that relied upon measurements of the velocity distribution both above and below the weir crest. However, this approach received criticism due to its impracticality for the practicing hydraulician at the time in that it required a priori knowledge of the channel velocity profile. In their discussion piece, Rehbock argued that in most cases of weir flow observed during laboratory experiments, the velocity distribution is nominally uniform. However, Schoder and Turner replied in their closure to the piece that this assumption is likely not to hold for weirs in operational field conditions (King et al., 1929). It still remains to be seen fully seen how variations observed in the field from the classical open-channel velocity profile measured in the laboratory can be incorporated into the weir flow equations.

Taking a slightly different approach to this topic, studies have also been completed on the effect of roughness on the free overfall in the laboratory (Rajaratnam et al., 1976; Sterling, 1998; Shubing and Sheng, 2019). Generally, the presence of boundary roughness is known to decrease the discharge coefficient of flow over the weir. What is still left obscured is an understanding of how the increased flow inertia occurring in flow over field-scale structures interacts with the more variable channel roughness caused by vegetation and sediments.

3.3.3 Scale Effects

An additional important consideration in weir flow is a proper understanding of the problem from a dimensional analysis perspective. Here, the empirical equations that can be developed for dimensionless parameters, such as the discharge coefficient, are only valid when certain scale effects related to the fluid viscosity and surface tension can be neglected. Important studies on this topic are those of Matthew (1963); Sarginson (1972); Ranga Raju and Asawa (1977); Johnson (1996); and Swamee et al. (2001). Primarily, this work on scale effects has focused on defining the lower limit of experimental scales. Generally, the threshold hold for when scale effects have been shown to be prominent for flow over vertical weirs is at low heads where $h <\sim 0.05$ m (Kindsvater and Carter, 1959).

3.3.4 Weir Characteristics

The surface roughness of the weir is also a notable factor influencing the flow dynamics (Pařílková et al., 2012; Ghobadian et al., 2013; Lau and Afshar, 2013; Alboresha and Hatem, 2021; Qian et al., 2021). Generally, surface roughness on the face of the weir has been shown to decrease the discharge coefficient of flow over the weir, and some corrective factors have been established to adjust for this effect in the weir discharge equation.

3.4 Investigation of the Flow Field Characteristics

3.4.1 Pressure, Velocity, and Free Surface Profiles

In addition to more hydraulically minded investigations into the influence of a number of factors on the discharge characteristics of weirs, a less voluminous but still significant body of work has also been developed to investigate the phenomena of weir flow on a deeper level. These studies have focused on the shape of the nappe profile, velocity and pressure distributions, and the location of the critical section with respect to the crest. For the sharp-crested weir, this was first completed by Bazin (1898), and followed up with additional thorough observations by Rouse (1932), Bureau of Reclamation (1948), and Rajaratnam and Muralidhar (1971). Advances in numerical modeling have also provided new insights into the flow characteristics of sharp-crested weirs, as shown by Ferrari (2010) and Sinclair et al. (2022). For the free overfall, descriptions of the pressure and velocity profiles were initially completed by Rouse (1932, 1936) and advanced by Rajaratnam and Muralidhar (1968) and Hager (1983).

The flow characteristics of the tilting weir have received less attention, except for the work of Bazin (1898) and Bureau of Reclamation (1948) to determine the influence of the inclination angle on the nappe profile of weir flow. Additional work is needed to investigate the velocity and pressure distributions of the tilting weir and how these relate to the well-established profiles of the sharp-crested weir and the free overfall.

3.4.2 Boundary Layer Characteristics

One of the interesting aspects of weir flow concerns the implicit assumptions in the discharge equation, namely that the flow is inviscid and irrotational. The validity of these assumptions has been only preliminarily investigated for different cases of weir flow. The primary questions for these investigations have been to determine the regions of the flow field where these assumptions are valid, and identify the regions where they are not. The regions where these assumptions do not hold will be near the boundary of the flow in which viscous effects are present. For the case of the sharp-crested weir, it has been well-observed that a region of separation exists on the upstream side of the structure (see Figure 3.2).

Typically, researchers have been interested in investigating flow problems where separation occurs downstream of an object, and analyzing the reattachment length. Much work has been done on a similar type of structure, the canonical backward-facing step (Butté and Pichon, 1970; Armaly et al., 1983). However, for the case of weir flow, the separation occurs upstream due to the adverse pressure gradient along the bottom boundary created by the weir acting as a stagnation point. Kindsvater and Carter (1959) introduced a preliminary discussion of the boundary layer displacement thickness (δ_*) as a way to understand the overfall influence of viscous effects on the flow in comparison to the assumed condition of inviscid flow. Rouse (1960) also offered a discussion on the distribution of turbulent kinetic energy in the flow field, with an analysis of two canonical cases of symmetrical flow past a

Figure 3.2: Study of stream filaments over a spillway, showing the converging streamlines at the crest section and the turbulent zone of separation at the base of the structure. Photo courtesy of Rouse (1932).

sharp-edged pipe-inlet, and over a bluff-edged body. The type of flow separation that occurs in these cases is similar to that of a broad-crested weir.

Without the ability to make more detailed measurements, Rouse still postulated that the region of dissipation of turbulent kinetic energy occurred near the boundary in the viscous zone of separated flow. Following the conceptual framework of Prandtl (Anderson, 2005) to analyze the flow field as an outer inviscid region and an inner viscous boundary layer, Rouse (1960) postulated that the most production of turbulent kinetic energy would occur due to the presence of large velocity gradients in the shear layer between these two regions. A more detailed study to verify the hypotheses of Rouse (1960) with physical measurements has yet to be done for cases of weir flow, although similar studies have been completed for other engineering applications (Delafosse et al., 2011).

Other studies, such as Kirkil et al. (2008), have examined the time-dependency of large-scale flow structures of certain canonical flow problems, such as that past a circular bridge pier. If one considers the time variability present within turbulent flow, then coherent structures such as horseshoe vortices and turbulent bursts and sweeps can then be identified. This type of analysis has so far been very much lacking in the literature on flow over thin-crested weirs, likely because most researchers take a more hydraulics-informed perspective, where the primary object of importance is to see how the empirical discharge coefficient for a certain structure might be modified by certain influencing factors. However, the time-variability inherent to turbulent flow has been identified to cause fluctuations in the pressure condition of the nappe and level of the free-surface (Zachoval et al., 2012), which may lead to structural problems due to resonance.

3.5 Summary of Open Research Questions

In summary, there are several open research questions for the case of flow over tilting weirs. Some significant work has been completed to understand how the influence of the inclination angle might change the shape of the nappe profile and pressure condition at the crest (Bazin, 1898; Bureau of Reclamation, 1948). These analyses have led to studies on the discharge coefficient and what corrective factors can be employed to account for the effect of the inclination angle on the flow with respect to the perpendicular sharp-crested weir. However, open avenues of research for this problem of tilting weirs, and more generally the scope of flows containing sharp-crested and free overfall flow, can be identified to include:

- The effect of the inclination angle on the discharge coefficient for tilting weir flow, and how this can be best incorporated into existing flow measurement equations.

- The variability of the discharge coefficient with the inertial condition of the flow as measured by h/p and how this changes in the case of the sharp-crested weir, through the range of inclination angles represented by the tilting weir, and finally for the free overfall.

- The nature of the pressure and velocity profiles for the case of the tilting weir and how they related to the bounding cases of the sharp-crested weir and the free overfall.
- The identification of boundary layer and shear layer zones within the flow field of the sharp-crested weir, and how the changing inclination angle introduced by the tilting weir changes the spatial distributions of these zones as well as global budgets of TKE dissipation.
- How the combined influence of scale and channel roughness can be leveraged to examine the application of these types of flow measurement structures to field conditions.
- How to parameterize the influence of channel boundary roughness on the discharge coefficient and how this can be practically used in the field.
- The availability of higher-order approaches to developing the discharge equation for weir flow that allow for non-hydrostatic pressure effects caused by curvilinear streamlines near the crest.

Chapter 4

Experimental, Numerical, and Field Methodology

There are three main avenues of research in the field of hydraulics. As mentioned in Chapter 3, the majority of studies in the realm of weir flow have been situated within laboratories, where experiments are conducted on scaled physical models of prototype structures. However, in the laboratory the conditions are often idealized in a way that may not fully represent the complexity of phenomena observed in the field environment, and constructing physical models can be expensive. For this reason, it is also prudent to take observational data on operational field-scale structures. This, however, can prove difficult due to the lack of control on experimental variables and difficult conditions that researchers are faced with in the field.

In recent decades, with the advancement of more powerful computers and superior numerical methods, considerable knowledge advancement can also be accomplished through the use of numerical simulations. Once the start-up costs of hardware and proprietary codes are paid, the cost of executing numerical simulations is much smaller compared to laboratory experiments and field measurement campaigns. However, as alluded to in Chapter 2, the resulting equations used to model fluid flow numerically represent, at best, a close approximation to the actual nature of the flow that could be observed in the physical world. However, advances in numerical algorithms and spectral methods have allowed for the development of direct numerical simulations (DNS) that solve the governing equations of fluid flow (Eqns. (2.9) and (2.10)), albeit for relatively low Reynolds number (i.e., weakly turbulent) channel flows with simple geometries, due to the considerable computational cost of these efforts.

Due to the practical need of engineers to simulate more realistically turbulent flows with complex geometries, numerical approximations and parameterizations of turbulent Reynolds stresses, transport, and mixing are needed to solve fluid flow problems numerically. Ideally, these methods are validated using experimental data to ensure they accurately reproduce physical reality to an acceptable degree of accuracy. Numerical methods introduce some amount of artificial diffusion into the problem which can, if the method is unstable, grow unbounded. Regardless, even if the solution is stable, the numerical diffusion will mean the computed solution does not completely represent the actual fluid flow in all of its complexity as it occurs in nature. For these reasons, it is extremely beneficial to use a combination of techniques that combine experimental, numerical, and field observations. In this way, we gain a full picture of the flow problem as each method fills in the gap of observation not possible by the other methods. The available methodologies are discussed in the following sections.

4.1 Laboratory Measurements

The primary experimental facility for this study is the Environmental Fluid Mechanics Laboratory (EFML), under the supervision of Dr. Subhas Karan Venayagamoorthy at Colorado State University (CSU). Additional laboratory experiments were also conducted in collaboration with the Hydraulics and Hydromorphology Laboratory (HHLab) at the Villeurbanne-Lyon centre of L'Institut National de Recherche pour L'agriculture, L'alimentation et L'environnement (INRAE), under the supervision of Dr. Céline Berni and Dr. Marie Rastello during the Spring of 2023.

4.1.1 Laboratory Flume

The setting for laboratory experiments is in a recirculating flume which consists of an open channel with a smooth bed, smooth side walls, and a pump with a large water storage reservoir for maintaining the steady flow of a prescribed discharge. This set-up allows for the placement of physical models in the flume and observations of the resulting flow velocity field using highly accurate instrumentation. The prescribed discharge passing through the flume is measured using an electromagnetic flow-meter located in the pipe section upstream of the flume inlet. Other observational capabilities include measurement of the bed elevation and flow depth using a point-gauge (in the case of the EFML), or ultrasonic sensors (at HHLab).

4.1.2 Particle-Image Velocimetry

Laboratory measurements of the two-dimensional velocity field (u, w) are available using particle-image velocimetry (PIV). This is a non-intrusive method that utilizes the calculated displacement of neutrally buoyant plastic tracer particles seeded in the flow and then illuminated by a high-intensity laser. A high-speed camera captures the position of all particles in the field of view at a certain time instant, and then after a small time-step, another image is taken. Cross-correlation algorithms are then applied to calculate the displacement of the particles, and subsequently the velocity of the fluid itself. The maximum recording frequency of the images is 800 Hz. Typically, the 2D laser sheet is positioned in the center of the flume so that the velocity components in the streamwise (x) and vertical (z) directions can be computed. For most cases of weir flow, the velocity field is assumed to be uniform in the transversal (y) direction.

4.1.3 Acoustic-Doppler Velocimetry

Point measurements of the three components of the velocity field are also available using an Acoustic Doppler Velocimeter (ADV). This instrument utilizes a measured frequency shift in acoustic signals to estimate the velocity of tracer particles that act as passive scalars within the flow field. ADVs can measure on the order of $10^2 - 10^3$ Hz, allowing for an estimation of fluctuating turbulent quantities that occur on small time scales and comprise second-order moments of the velocity field. One drawback of ADV measurement in the laboratory is that it is an intrusive technique, resulting in local disturbances to the flow field around the probe (Rastello et al., 2022).

4.2 Numerical Simulations

The EFML research group has a robust history of seminal advances in the fields of experimental hydraulics and geophysical fluid dynamics through the use of high-resolution numerical simulations (Venayagamoorthy and Fringer, 2007; Mater et al., 2013; Zhou et al., 2017). This expertise can be leveraged to conduct numerical simulations of tilting weir flow that elucidate the more complex elements of the fluid dynamics beyond previous research. Computational facilities include access to the proprietary non-hydrostatic flow modeling code FLOW-3D, and high-processing computers with 40 cores, 256 GB of RAM, and a 3.10 GHz processor.

4.2.1 Reynolds-Averaged Navier-Stokes Models

As previously discussed in Chapter 2, the filtering of the instantaneous Navier-Stokes Equations into a mean and fluctuating field due to the practical constraint of being unable to capture the wide disparity of spatial and time scales present in fully turbulent flows with numerical simulations gives rise to the turbulent closure problem. There are zero, one, and two-equation models available as closure schemes for this problem, which are reviewed by Pope (2000). However, all turbulence closure schemes are founded on the same essential premise that the deviatoric Reynolds stress can be modeled as proportional to the mean shear rate using the turbulent-viscosity hypothesis (TVH):

$$-\langle u_i' u_j' \rangle \equiv \nu_t \left(\frac{\partial \langle U_i \rangle}{\partial x_j} + \frac{\partial \langle U_j \rangle}{\partial x_i} \right) - \frac{2}{3} \langle u_i' u_i' \rangle \, , \tag{4.1}$$

where ν_t is known as the turbulent viscosity and must be parameterized by the closure model. One of the most commonly used closure schemes for RANS simulations of free-surface flows is the two-equation k–ε model, which models ν_t using the equation:

$$\nu_t \equiv C_\mu \frac{k^2}{\varepsilon} \, , \tag{4.2}$$

where C_μ is a calibrated coefficient and two additional transport equations are introduced to model k and ε. Recent advancements on the calibration of C_μ can be found in Mishra and Venayagamoorthy (2024b). An extension of the k–ε model is the k–ω RANS model. In this model, ν_t is estimated as the ratio k/ω, where the specific dissipation rate, $\omega = k/\varepsilon$. The k–ω model typically performs better in near-wall regions where an adverse pressure gradient is present. Due to the desire to accurately model the flow separation zone upstream of the weir, the k–ω is used for the majority of RANS simulations in this dissertation.

4.3 Field Scale Observations

The opportunity for taking field measurements of existing operational tilting weirs is possible through existing collaborations with the Larimer and Weld Irrigation Company, as well as Obermeyer Hydro, Inc. Recent research published as a result of these collaborations can be found in Kutlu (2019) and Pugh et al. (2021). As previously mentioned, field observations are also critical to a complete understanding of any hydraulics problem, and investigations of this nature have been severely lacking in the literature on weir flow. When investigating the flow field of an operational prototype structure, there are several methods available for determining the velocity field. The two discussed here are some of the most commonly used techniques, but this section does not feature an exhaustive report of all the possible methods available.

4.3.1 Acoustic-Doppler Current Profilers

The Acoustic Doppler Current Profiler (ADCP) has been used over the past several decades and has revolutionized the procedure for taking measurements of flow discharge in the field (Mueller et al., 2013). The instrument utilizes the Doppler shift principle to calculate the velocity of suspended sediment particles contained within the fluid column. However, instead of light as the emitted signal, it is sound waves. The ADCP can measure at multiple points within the z direction along a water column profile, and thus is often used as a discharge measurement device because these several measurements of the fluid velocity along a vertical are then averaged and integrated to calculate the mass flux of water over a particular section in the transversal direction.

The ADCP is an immensely useful device, but suffers from significant limitations in measurement capabilities that can often be easily overlooked. Primarily, the maximum sampling frequency for most ADCPs on the market today is only 1-2 Hz. This may be sufficient for capturing first-order statistics, such as the mean velocity field, but is bound to be insufficient for capturing the full richness of time scales present in practical turbulent flows. Further, due to the underlying principle of Doppler-shift utilized by the ADCP, there are several regions of unmeasured flow in any ADCP discharge measurement. These unmeasured zones are the area near the fluid free-surface, the channel boundary, and the channel side walls. Issues with beam interference arise when measuring near the wall and channel boundary, and measurements near the free surface are limited by the necessary lag-time of the receiver. Recent developments by Pugh et al. (2021) and Díaz Lozada et al. (2021, 2023) have worked to reduce uncertainty and increase the accuracy of ADCP measurements, but significant work still remains to be done to investigate the gap in measurement capabilities, especially for higher-order turbulence metrics, that the ADCP possesses in comparison to more highly resolved instruments.

Chapter 5

Demystifying the Discharge Coefficient [1]

5.1 Introduction

5.1.1 Curvilinear Weir Flow

Free-surface flow over a vertical weir has been a problem of considerable practical as well as theoretical interest for many centuries (Eckert, 2024). It has proven useful for determining the efflux of water in hydraulic engineering applications, while also representing an amalgam of several canonical flows that are of interest to hydrodynamicists. Upstream of the weir, primarily one-dimensional hydrostatic open-channel flow is present, which transitions in the approach to the weir to convergent flow through a sharp-edged orifice (Perry, 1949), and finally to a gravity-driven free jet (Tuck, 1976). Additionally, a turbulent boundary layer subjected to an adverse pressure gradient, (Na and Moin, 1998; Kitsios et al., 2017) created by the stagnation along the vertical weir face, undergoes separation and results in a zone of recirculating flow at the base of the weir. The combination of phenomena in this flow field rewards it with the designation of being "an exceedingly complex problem at best" (Street et al., 1996) - making it a suitable candidate for fundamental research, and empirical simplifications when prudent.

The viability of the weir as a reliable device for measuring discharge is dependent on the following two main conditions: 1) the flow field can be well approximated as two-dimensional in the streamwise and vertical directions, and 2) the falling nappe is sufficiently ventilated so that atmospheric pressure is present along both the upper and lower free surfaces.

---

[1] The research presented in this chapter has been accepted for publication in the journal *Flow* under the title "Demystifying the Discharge Coefficient for Flow Over Thin Weirs and Sills" by J.E. Pugh, S.K. Venayagamoorthy, and T.K. Gates. This chapter is written to reflect and acknowledge the contribution of the co-authors.

The dynamic parameter describing a particular weir flow condition is given by the ratio h/p. This inertial condition with respect to the size of the weir obstacle is defined by the ratio of the pressure head (h) measured at the gauging section, which drives the flow over the weir, to the height of the weir crest relative to the channel bottom (p) (see Figure 5.1).

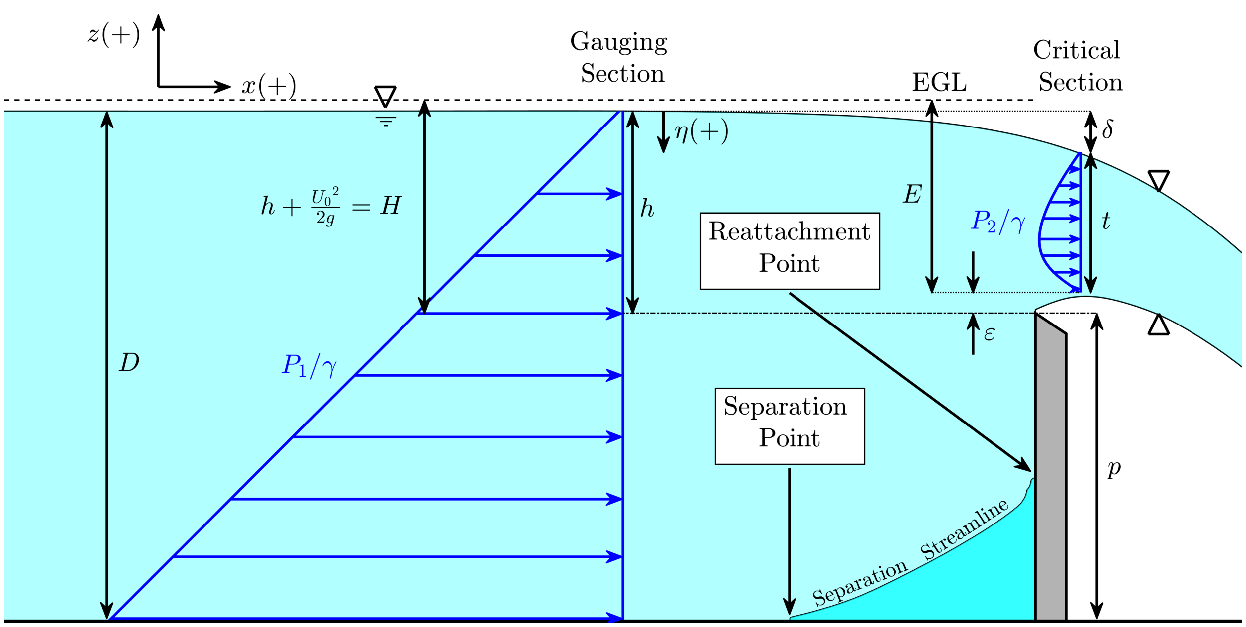

Figure 5.1: Schematic of curvilinear flow over a thin weir. It is assumed that the flow field can be approximated as two-dimensional, and that the overflowing nappe is fully supported by atmospheric pressure. All dimensions plotted are scaled from 3D numerical results for a specific flow case where $h/p = 0.68$ (case N0.68 in Table 5.2). A separation streamline is plotted to indicate the locations where the boundary layer becomes detached due to the adverse pressure gradient created by the weir, and where it then eventually reattaches. The shape of the separation zone will differ under varying flow conditions. EGL is the energy grade line, given by the dashed line.

Weir flow can be considered to have two bounding cases as defined by h/p. The wall overflow condition occurs in the limit as $h/p \to 0$, occasionally called an "infinitely high" weir, (Lauck, 1925; Rouse, 1932) and is applicable to when the structure is placed on the crest of a dam spillway. As $h/p \to \infty$, the obstructive effect of the weir vanishes and the flow becomes a free overfall (Rouse, 1936; Rajaratnam and Muralidhar, 1968). The obstacle is often described as a sill rather than a weir when approaching this upper limit (Ramamurthy et al., 1987). Typical weir channel flows observed in hydraulic engineering practice have

$h/p = \mathcal{O}(10^0)$ (Ackers et al., 1978). In the gauging section, the volumetric discharge per unit channel width is defined as q, with the characteristic velocity scale in this section being $U_0 = q/D$.

The critical section, or vena contracta, is the location of minimum specific energy (E), identified as the longitudinal position where the maximum elevation of the lower nappe surface occurs (Montes, 1998). This definition of the critical section necessarily differs somewhat from that used for hydrostatic open-channel flows. For curvilinear weir flow, the pressure is no longer hydrostatic in the transition from subcritical to supercritical and the velocity is no longer uniform. Therefore, the critical section cannot be simply defined here as where the mean flow speed equals the small wave celerity. Instead, it is defined more generally as the location where the derivative of specific energy with respect to flow depth equals zero. For weir flows, this has been shown to be where the elevation of the bottom boundary reaches a maximum (Castro-Orgaz and Hager, 2017).

The thickness of the nappe in this section is noted as t, and the average velocity in the nappe at this section is given by $\overline{u} = q/t$. The relative effects of draw-down on the upper nappe surface, and deflection of the lower nappe surface above the crest elevation, are given by δ and ε, respectively, so that $h = \varepsilon + t + \delta$. η is chosen as an arbitrary parameter to represent the vertical distance of a fluid layer below the free surface at the gauging section.

5.1.2 Governing Equations and Review of Previous Work

Hydrodynamics perspective

The physics governing the motion of fluid over a weir is described by the steady, incompressible Navier-Stokes equations. For purposes of determining steady discharge, an assumption of two-dimensional flow is made, meaning that the three-dimensional flow field is taken to be uniform in the transverse (y) direction (the dimension over which the crest spans the channel). This assumption allows boundary drag along the channel side walls to be neglected, along with lateral contraction and detachment of the nappe. This assumption is taken to be valid as long as the approach channel width (B) is at least eight times h (Bureau of Reclamation, 2001). With these simplifications, the coupled pressure-velocity field is given by:

$$\mathbf{u} \cdot \nabla \mathbf{u} = -\frac{1}{\rho} \nabla P - g\hat{k} + \nu \nabla^2 \mathbf{u} \,, \tag{5.1}$$

with the continuity condition:

$$\nabla \cdot \mathbf{u} = 0 \,, \tag{5.2}$$

where $\mathbf{u}$ is the two-dimensional velocity field ($\mathbf{u} = u\hat{\imath} + w\hat{k}$); P is pressure; ρ and ν are the fluid density and kinematic viscosity, respectively; and g is the gravitational constant (equal in this study to 9.81 $\mathrm{m/s^2}$).

It was recognized by early pioneers in hydrodynamics that the wall overflow case is a suitable candidate for analyses invoking the inviscid fluid assumption due to the convergent nature of the flow field and ability to assume the negligible effect of boundary friction. Approximate analytical solutions can be found via complex analysis of the potential velocity, which utilizes numerical integration methods to solve for the two-dimensional fluid velocity field described by the stream function (ψ) and velocity potential (ϕ). For steady, inviscid, incompressible, and irrotational flow, boundary conditions for this approach are given by the Bernoulli equation:

$$\frac{P}{\rho} + \frac{1}{2}(u^2 + w^2) + gz = \text{constant} \,. \tag{5.3}$$

Dias and Tuck (1991) provide a good formulation of the complex-potential flow analysis problem. Early notable advancements in the field taking this approach were those of Lauck (1925), who approximated the shape of the free-surface and estimated the contraction coefficient ($C_c = t/h$) for the wall overflow. For this case, Lauck (1925) found C_c to be the same as Kirchhoff's coefficient for a planar free jet issuing from a sharp-edged orifice ($\pi/\pi + 2 \approx 0.611$). Notably, Strelkoff (1964) expanded the complex-potential flow analysis for the weir problem by putting forward a formulation that proposed a solution for the free-surface profile and discharge characteristics for any value of h/p. Similar approaches have also been fruitfully applied to approximate the profiles of the free overfall (Tuck, 1976; Dias and Tuck, 1991), as well as subcritical (Vanden-Broeck and Keller, 1987) and supercritical (McLean et al., 2022) weir flows.

As elegant as these analytical solutions of potential flow are, it is not often that these results, and the assumptions of inviscid and irrotational flow implicit within them, are validated against experimental observations. The flow physics explored in these analyses can also sometimes lack practical value, such as imposing a supercritical upstream boundary condition for flow over a weir (McLean et al., 2022). It was noted by Rouse (1964) that the inviscid results of Strelkoff (1964) generally agreed well with experimental results for small values of h/p, but began to deviate as h/p increased towards the free overfall limit. This occurs because in this limit, the size of the turbulent boundary layer in relation to the overfall flow field renders invalid the assumptions of inviscid and irrotational flow. Here we are met again with the infamous injunction to resort to empirical investigations when dealing with the complexities of turbulent flows. In addition to this, the analytical methods previously described proved overly tedious for the hydraulic engineer, whose primary concern was a simple and reliable estimation of discharge. For these reasons, we will now trace the development of the weir and sill flow studies through the practice of hydraulics.

Hydraulics perspective

In the early days, the Italian marquis Giovanni Poleni formulated what is now known as the weir-discharge or Poleni equation by conceptualizing the flow over a thin vertical weir as an orifice flow capped by the free surface, and driven by an upstream reservoir of hydrostatic stagnation pressure head (h). Utilizing the Torricelli principle (see Eq. (5.3)) to estimate the velocity of fluid layers within the overflowing jet and integrating from the crest elevation, p, to $h + p$, the following equation (sometimes referred to as the Poleni equation) was eventually put forward as a means for estimating volumetric discharge per unit channel width (q) passing over the crest of a vertical weir:

$$q \approx \frac{2}{3}\sqrt{2g}h^{3/2} \rightarrow q = C_d \frac{2}{3}\sqrt{2g}h^{3/2} \,. \tag{5.4}$$

Like Eq. (5.3), Eq. (5.4) is derived from assumptions of inviscid and irrotational flow. It also neglects any contraction within the nappe, as well as the velocity head at the gauging section, ${U_0}^2/2g$. It is well-known in practice that these assumptions are not strictly true. For this reason, the introduction of the discharge coefficient (C_d) is found in Eq. (5.4) to account for these violated assumptions. A reliable empirical equation for C_d as a function of practically measurable parameters, h and p, was the goal of much of the previous hydraulics studies. Foundational early research can be credited to Bazin (1898) and Schoder and Turner (1929) for weir flows - the latter of which also examined the influence of the velocity distribution in the approach channel on the discharge characteristics. A robust empirical equation relating the magnitude of C_d to h/p for weir flows of $h/p = \mathcal{O}(10^0)$ was put forward by Theodor Rehbock at the Karlsruhe Institute of Technology, described in English in his discussion of the results of Schoder and Turner (1929) in King et al. (1929). Rouse (1936) extended the discharge-measuring capacity of these types of structures further by applying a similar analysis to the free overfall. Kindsvater and Carter (1959) also notably included a discussion of scale effects due to viscosity and surface tension at low values of h, suggesting that these can result in a greater than 2% variation in the prediction of discharge when $h < 5$ cm (assuming the fluid is water).

A link between the results of Schoder and Turner (1929) for weir flows and Rouse (1936) for the free overfall was first provided by Kandaswamy and Rouse (1957), who examined the discharge characteristics of weir and sill flows spanning the full range of h/p. A commonly used weir-discharge formulation found today is that of Kandaswamy and Rouse (1957), where for $h/p \leq 6$: $C_d = 0.611 + 0.075h/p$, and for $h/p \geq 16.66$: $C_d = 1.06(1 + p/h)^{3/2}$. This formulation features a non-monotonic relationship between h/p and C_d, which Kandaswamy and Rouse (1957) hypothesized was due to a maximum in the relative nappe thickness as the flow changes from a weir to sill regime. The reason for this phenomenon has so far not been elaborated on, and represents one of the main goals of this study.

Bridging the gap

Although the dependence of C_d upon h/p has received much attention in the literature, a physical description of C_d has remained elusive. It is not immediately apparent which of the aforementioned assumptions regarding irrotationality, contraction, and upstream velocity head are a fair approximation in the majority of cases of weir flow, the conditions under which these approximations might break down, and how this might inform a physical description of C_d. A survey of common textbooks used in undergraduate fluid mechanics courses in the United States reveals that C_d is described as a "lumped parameter", accounting for friction loss between the gauging section and crest section, contraction of the overflowing nappe, contribution of the upstream velocity head, and scale effects due to surface tension and viscosity (Sturm, 2001). However, we believe what has been lacking in the literature until this point is a cogent description of the contributing factors underlying the physical meaning of C_d through its decomposition from experimental and numerical results to show which of the aforementioned effects are most dominant. For this reason, we choose in this study to develop a new semi-empirical expression for weir discharge using dimensional analysis in hopes of demystifying the meaning of C_d.

Elucidation of the nature of C_d and its variability can be sought by examining the flow field dynamics - namely the pressure and velocity profiles at important sections. Earlier work on this was completed by Scimemi (1930) and Rouse (1932), who measured the free surface profiles for several cases of h/p, pressure profiles at various points using manometers, and velocity using Pitot tubes. These results have been critical for validating the output of numerical simulations and analytical approximations. This work was furthered by the results of Rajaratnam and Muralidhar (1968, 1971) and Ramamurthy et al. (1987). However, the flow field dynamics for the full h/p range from the wall overflow to free overfall have yet to be fully characterized and rightly contextualized for the practical weir flow problem. This represents the main goal of this study - a revised definition and understanding of C_d gained from new data that reconciles traditional insights from both hydrodynamics and hydraulics.

The need to rejoin these traditionally divergent fields of study was recently highlighted by Michael Eckert in his historical review of the more general efflux problem: "From an epistemic and historiographic perspective, this study calls for inquiries that combine the history of science with that of engineering. The history of fluid mechanics may not be approached from one or the other side alone, and specific cases such as the efflux problem provide suitable probes in this quest" (Eckert, 2024). In this study, we endeavor to do just that, through the following aims:

1. Revise the formulation of the weir-discharge equation to clarify the meaning of C_d.
2. Provide additional data on the discharge characteristics and flow field dynamics of viscous flow over weirs and sills, especially towards the upper limit of the free overfall.
3. Elucidate the reason for the non-monotonic trend between h/p and C_d observed by Kandaswamy and Rouse (1957) and Ramamurthy et al. (1987).
4. Clarify the delineation between the respective weir and sill flows, along with a description of other regimes to inform reliable flow measurement.

5.2 Dimensional Analysis for the Weir Flow Problem

Since the development of Eq. (5.4), the field of hydraulics has advanced through dimensional analysis using the Buckingham Π theorem. This methodology has been applied to the weir flow problem in the past (Kindsvater and Carter, 1959; Ackers et al., 1978), with insights informing the physical parameters influencing the non-dimensional discharge. For completeness, we show the dimensional analysis for fully ventilated weir flow again here. The relevant parameters for determining q are:

$$q = f(h, p, g, \rho, \mu, \sigma) \, , \tag{5.5}$$

where previously undefined parameters are the fluid properties of dynamic viscosity, μ; and surface tension, σ. In the classical dimensional analysis of weir flow, as found in Kindsvater and Carter (1959), h is chosen as the relevant dynamic flow parameter and length scale when predicting the discharge. This is because h is often readily measured from the hydrostatic pressure relationship, and for subcritical flows over a weir, $U_0 = f(h)$ (Vanden-Broeck and Keller, 1987). The value of h is typically measured at a longitudinal distance of approximately 3–4h upstream of the weir crest (Bos, 1976). The other important geometric parameter is p, representing the height of the obstruction. Physical fluid properties must be included to account for scale effects. The basic dimensions can be represented using appropriate scaling variables such that $M \equiv \rho h^3$, $L \equiv h$, $T \equiv h/\sqrt{gh}$, and $V \equiv \sqrt{gh}$. This scaling will result in the following Π terms: $\Pi_1 = Fr_h = q/\left(\sqrt{g}h^{3/2}\right)$, $\Pi_2 = h/p$, $\Pi_3 = Re_h = \rho\left(\sqrt{g}h^{3/2}\right)/\mu$, and $\Pi_4 = We_h = \left(\rho g h^2\right)/\sigma$.

Three common dimensionless numbers appear: the Froude number - Fr_h, the Reynolds number - Re_h, and the Weber number - We_h. These are given the subscript h to differentiate them from more common definitions for free-surface flow using other length and velocity scales. Assuming that fluid properties remain constant, it is seen that the only dynamic parameter in Π_3 and Π_4 is h. Since $We_h \propto Re_h^{4/3}$, only Re_h is necessary to account for scale effects at low values of h. If it is assumed these scale effects are negligible above a certain threshold value of Re_h, the simplified dimensionless equation for weir discharge becomes:

$$Fr_h = \phi(h/p) \text{ for } Re_h \gg 1 \,. \tag{5.6}$$

Thus, a simplified form of the weir discharge equation is:

$$q = \phi(h/p)\sqrt{g}h^{3/2} \,, \tag{5.7}$$

where the function $\phi(h/p)$ approximates Fr_h within a normal operating range of h/p in which scale effects are negligible. Previous studies have indicated that a suitable value for this threshold is $Re_h = 3.5 \times 10^4$ (Kindsvater and Carter, 1959; Pugh et al., 2024), equivalent to a minimum h of ≈ 5 cm to drive the water flow. By comparing Eq. (5.4) and Eq. (5.7), it can be seen that Fr_h is simply $(2\sqrt{2}/3)C_d$. We choose here to refer to Fr_h as a weir Froude number, intended to serve as an alternative to the classical weir discharge coefficient C_d. The result of this approach is that a physical understanding of the dimensionless coefficient on the front-end of the weir discharge equation is obtained, in that it is best understood as a ratio of inertial to gravitational effects. To our knowledge, the only other work to propose an understanding of the weir discharge coefficient as a type of Froude number is that of Street et al. (1996). With a fundamental definition of C_d as a ratio of inertial to gravitational effects now established, we will proceed to its derivation from Eq. (5.3) to reveal its constituent parts.

5.3 Revisiting the Discharge Coefficient

As discussed earlier, Poleni first derived his equation for weir discharge by envisioning the flow over a weir as an integrated sum of Torricelli's problem of flow through a sharp-edged orifice at the bottom of a reservoir, where the jet freely enters into the atmosphere and the flow is driven by a static pressure head (h') above a jet opening of width d. The unit volumetric discharge of the jet, q', is given by the general orifice equation (Streeter, 1985):

$$q' = \overline{u}'t' = ({C_v}'\sqrt{2gh'})({C_c}'d) \,, \tag{5.8}$$

where $\overline{u}'$ is the average velocity in the jet over thickness t'. The term $\sqrt{2gh'}$ is the theoretical velocity given by Eq. (5.3) from assumptions of steady, inviscid, and irrotational flow. ${C_v}'$ is then a correction coefficient for any local energy losses that occur due to separation as the flow navigates the orifice opening. As the jet exits the orifice and the streamlines become horizontal, the jet diameter contracts. Thus, the jet thickness in the vena contracta, t', divided by the height of the orifice opening, d is a contraction coefficient ${C_c}'$.

Returning now to the derivation of Eq. (5.4) and referring back to Figure 5.1, it can be seen that if Eq. (5.3) is applied between the free surface at the gauging section and the crest section, the velocity ($u(\eta)$) within the overflowing jet of a fluid layer at a distance η below the free surface can be estimated as:

$$h + \frac{{U_0}^2}{2g} = h - \eta + \frac{u(\eta)^2}{2g} \Rightarrow u(\eta) = \sqrt{2g}\left(\eta + \frac{{U_0}^2}{2g}\right)^{1/2} . \tag{5.9}$$

q is estimated by integration of the RHS of Eq. (5.9) from $\eta = 0$ to $\eta = h$:

$$q \approx \sqrt{2g}\int_0^h \left(\eta + \frac{{U_0}^2}{2g}\right)^{1/2} d\eta = \frac{2}{3}\sqrt{2g}\left[\left(h + \frac{{U_0}^2}{2g}\right)^{3/2} - \left(\frac{{U_0}^2}{2g}\right)^{3/2}\right] . \tag{5.10}$$

The theoretical average velocity in the jet, $\overline{u}_t$, predicted by Eq. (5.10) is then:

$$\overline{u}_t = \frac{1}{h}\frac{2}{3}\sqrt{2g}\left[\left(h + \frac{{U_0}^2}{2g}\right)^{3/2} - \left(\frac{{U_0}^2}{2g}\right)^{3/2}\right] , \tag{5.11}$$

and the orifice flow equation (Eq. (5.8)) can be written for the weir flow problem as:

$$q = C_v \overline{u}_t (C_c h) , \tag{5.12}$$

where:

$$C_v = \frac{\overline{u}}{\overline{u}_t}, \text{ and } C_c = \frac{t}{h} . \tag{5.13}$$

$\overline{u}_t$ is given by Eq. (5.11). As mentioned earlier, $\overline{u} = q/t$, and the correction coefficients in Eq. (5.12) are commonly lumped into a single coefficient so that the need for *a priori* knowledge of U_0 in Eq. (5.11) is eliminated. Thus, the relation between Eq. (5.12) and the commonly used Poleni equation (Eq. (5.4)) is given by:

$$q = (C_v C_c)\frac{2}{3}\sqrt{2g}\left[\left(h + \frac{{U_0}^2}{2g}\right)^{3/2} - \left(\frac{{U_0}^2}{2g}\right)^{3/2}\right] = C_d\frac{2}{3}\sqrt{2g}h^{3/2} . \tag{5.14}$$

Examining Eq. (5.14), it can be seen that C_d is then the product of three terms:

$$C_d = C_v K C_c \,, \tag{5.15}$$

where K is a correction factor incorporated to account for the missing gauging section velocity head (${U_0}^2/2g$) in Eq. (5.4) (Rouse, 1946b):

$$K = \frac{1}{h^{3/2}}\left[\left(h + \frac{{U_0}^2}{2g}\right)^{3/2} - \left(\frac{{U_0}^2}{2g}\right)^{3/2}\right] = \left[\left(1 + \frac{{U_0}^2}{2gh}\right)^{3/2} - \left(\frac{{U_0}^2}{2gh}\right)^{3/2}\right] . \tag{5.16}$$

Thus, for normal operating regimes where scale effects may be neglected, the discharge coefficient, C_d, can be understood as a correction factor that accounts for: viscous friction losses, upstream velocity head, and contraction. Returning to the dimensional analysis in section 5.2, the simpler characterization of dimensionless discharge, Fr_h, which retains the intuitive definition of being a ratio between inertial and gravitational effects, can also be easily decomposed as:

$$Fr_h = \left(\frac{2\sqrt{2}}{3}\right) C_v K C_c \,. \tag{5.17}$$

We will now examine the contribution of the three component terms on the right-hand side of Eq. (5.17) towards the overall behavior of Fr_h as h/p varies in pursuit of the proper form of the function $\phi(h/p)$ in Eq. (5.7).

5.4 Research Methodology

This analysis synthesizes previously published data on sharp-crested weirs, along with new experimental data collected by the authors. A summary of these data is provided in Table 5.1. In general, the experimental data sets of Table 5.1 were completed within laboratory flumes where the weir crest was placed on the downstream end of the flume to ensure full ventilation of the nappe. Flow depth measurements were typically made using a point gauge, hook gauge, or similar device. Discharge measurements were made using a

Table 5.1: Description of compiled historical discharge data for thin weir and sill flows, along with that of the current study. n is the number of observations in the dataset. The total number of historical observations is 436.

Study Name	Abbreviation	Study Type	b (m)	n	h/p	Re_h	Fr_h
Bazin (1898)	Ba1898	Experimental	1–2	19	0.14-1.14	7.67×10^4–7.27×10^5	0.60–0.67
Schoder and Turner (1929)	ST1929	Experimental	1.29	270	0.004-4.00	1.51×10^3–1.70×10^6	0.58–0.91
Scimemi (1930)	Sc1930	Experimental	0.5	3	0.13-0.38	2.58×10^4–1.34×10^5	0.60–0.61
Bureau of Reclamation (1948)	BoR1948	Experimental	0.62	69	0.03-0.96	2.38×10^4–6.63×10^5	0.57–0.63
Kindsvater and Carter (1959)	KC1957	Experimental	0.03–0.82	48	0.18-2.38	1.46×10^4–2.84×10^5	0.59–0.73
Kandaswamy and Rouse (1957)	KR1957	Experimental	0.31	9	5.00-25.00	1.48e+04-1.66e+05	0.96–1.13
Strelkoff (1964)	St1964	Numerical	NA	4	2.12-10.38	∞^* (inviscid flow)	0.72–1.10
Ramamurthy et al. (1987)	Ra1987	Experimental	0.6	14	1.12-33.24	4.11×10^4–1.08×10^5	0.66–1.13
Current Study	PVG2025E	Experimental	0.3–1	134	0.21-2.54	1.49×10^4–1.50×10^5	0.52–0.76
Current Study	PVG2025N	Numerical	1	11	0.27-∞	6.99×10^4–1.30×10^5	0.60–1.14

previously calibrated weir, a flow meter in the inlet pipe to the flume, or a weighing tank mechanism. New experimental and numerical results of the authors include supplemental results of the steady two-dimensional flow field, summarized in Table 5.2, produced using particle image velocimetry (PIV) for one case where $h/p = 0.68$ (E0.68), along with eleven numerical simulations using FLOW-3D (Flow Science, Inc., 2023).

5.4.1 Experimental Measurements

Initially, observations of head (h) and steady discharge (Q) were made over a physical model of a sharp-crested weir at the Environmental Fluid Mechanics Laboratory (EFML) at Colorado State University (see Figure 5.2a). The height of the model was $p = 150$ mm. The length of the flume was 5 m in total, with a width of 0.3 m and a horizontal slope. The weir was placed 3 m downstream of the inlet. PVC tubes were installed beneath the weir crest on the downstream side to provide proper ventilation of the nappe per specifications of Bos (1976). Flow straighteners and a boundary layer tripping tool at the flume inlet were also installed to achieve as-close-as-possible a fully developed turbulent flow profile. Flow depths were measured using a point-gauge placed 1 m upstream of the model, and steady discharges were measured using an electromagnetic flow meter installed in the inlet pipe of the flume.

Table 5.2: Details for numerical and experimental flow cases of the current study where the two-dimensional velocity and pressure field were analyzed. The numeric value in the case name corresponds to the h/p value for that case.

Name	Data Type	h (mm)	p (mm)	q (L/s/m)	b (m)	h/p	Fr_h	C_v	K	C_c (t/h)	ε/h	δ/h
N0.27	Numerical	106.9	399.0	65.59	1.00	0.27	0.60	0.95	1.01	0.66	0.09	0.24
N0.48	Numerical	119.9	249.0	80.39	1.00	0.48	0.62	0.94	1.03	0.68	0.09	0.23
E0.68	Experimental	102.7	150.0	66.67	0.30	0.68	0.65	0.96	1.05	0.68	0.13	0.19
N0.78	Numerical	101.8	150.0	64.61	1.00	0.68	0.64	0.94	1.04	0.69	0.09	0.22
N1.12	Numerical	111.5	100.0	77.81	1.00	1.12	0.67	0.95	1.08	0.69	0.09	0.22
N2.05	Numerical	102.5	50.0	75.11	1.00	2.05	0.73	0.95	1.14	0.71	0.07	0.22
N3.29	Numerical	82.4	25.0	66.39	1.00	3.29	0.90	0.97	1.26	0.78	0.07	0.15
N5.90	Numerical	88.5	15.0	89.56	1.00	5.90	1.09	0.99	1.43	0.81	0.06	0.13
N8.52	Numerical	85.2	10.0	89.11	1.00	8.52	1.14	0.98	1.50	0.82	0.02	0.15
N12.25	Numerical	85.7	7.0	88.42	1.00	12.25	1.12	0.99	1.51	0.79	0.01	0.20
N22.12	Numerical	88.5	4.0	86.58	1.00	22.12	1.05	1.02	1.49	0.73	0.01	0.25
NFO	Numerical	79.2	0.0	69.87	1.00	∞	1.00	1.01	1.48	0.71	0.00	0.29

Additional head-discharge measurements were completed at the Hydraulics and Hydromorphology Laboratory (HHLab) at INRAE Lyon, France by the first author. This experimental set-up featured an adjustable-crest weir at the end of an 18 m flume with a width of 1 m. A sharp-edged crest piece was affixed to the top of the weir to ensure springing flow (Figure 5.2b). The range of crest heights examined was 50–150 mm. Flow depth measurements were made using ultrasonic water-level sensors, and steady discharge was measured using an electromagnetic flow meter.

Two-dimensional planar PIV observations also were collected at the EFML using a dual head Nd:YLF 527 nm green laser (Photonics model no. DM-527-30), and a high-speed CMOS camera with a 2560 x 1600 pixel resolution, 12-bit depth, and maximum capture rate of 800 frames per second (Phantom model no. VEO-E 340L). A LaVision programmable timing unit (PTU 10) was used as a synchronizer, and the LaVision Davis 10 software was used for PIV velocity field calculations on a 16-core Supermicro machine with an Intel Xeon E5-2620 v4 processor and 64 GB of RAM. Pressure-from-PIV calculations also were performed using an in-house code that solved the Poisson equation implicitly, although these results were limited in accuracy due to the difficulty of correctly defining the boundary conditions.

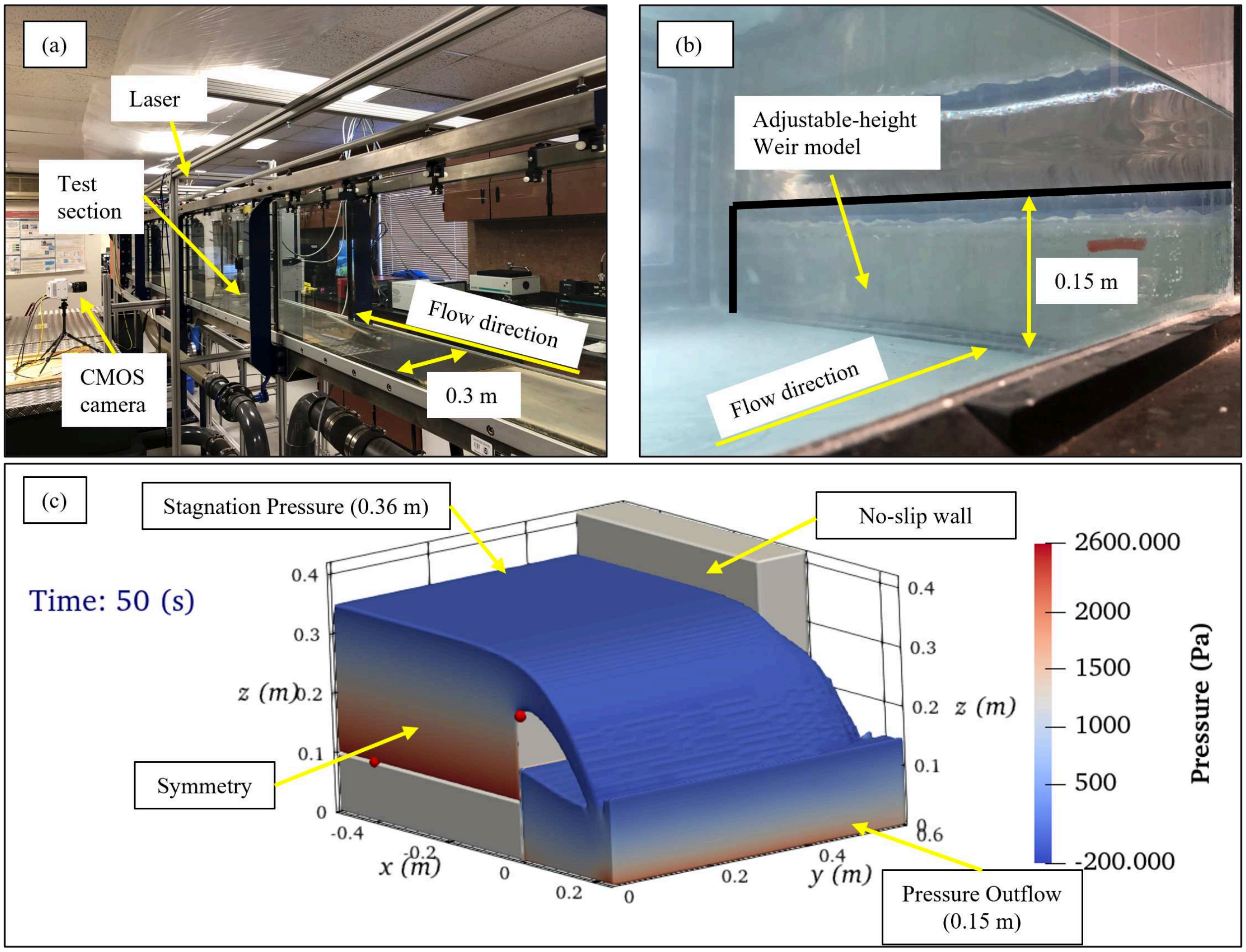

Figure 5.2: (a) Experimental facility at the EFML. (b) Weir model used at the HHLab facility. (c) Numerical domain for flow case N0.68. The upstream boundary of the domain in the x-direction has been truncated from -10 m to -0.5 m to show details of the near-crest region. Red dots represent pressure probes at the gauging section and just below the weir crest. Text boxes with arrows indicate boundary conditions.

5.4.2 Numerical Simulations

Numerical simulations of fluid flow were completed using FLOW-3D version 22.2 on a 32-core machine with an Intel Xeon E5-2680 v3 processor and 128 GB of RAM. A Reynolds-Averaged Navier-Stokes (RANS) modeling approach with the $k{-}\omega$ turbulence model (Wilcox, 1988) was chosen due to the desire to model viscous flow phenomena subjected to an adverse pressure gradient, and its cheaper computational cost compared to Large Eddy Simulation (LES). Flow development was achieved by allowing the simulation to run for at least 45 s of flow time, along a distance of 10 m in the approach to the crest. The width of the numerical domain was 0.6 m, with a rigid wall of width 0.1 m placed on one side of the domain to allow for a free-falling nappe (see Figure 5.2c). This resulted in an effective approach channel width of 1 m, due to a symmetry boundary condition being placed on the mesh face opposite the solid side wall. The longitudinal boundary conditions were an upstream stagnation pressure given by a fluid elevation that represented approximately 10.1 cm of head above the crest elevation, and a pressure outflow boundary condition with a fluid elevation of 0.15 m. For all simulations, the orthogonal grid size was 5 mm in the longitudinal (x) and vertical (z) directions and 10 mm in the transversal (y) direction. An additional mesh with 1 mm resolution in the x and z directions was included to enclose the weir geometry so that its sharp interfaces were well-resolved. Three-dimensional simulations were completed to ensure the numerical channel width was wide enough to neglect side-wall effects, and to allow for sufficient ventilation of the falling nappe. Analysis was completed on a two-dimensional ($x - z$) planar slice taken from the boundary opposite the channel side-wall. A grid sensitivity analysis for the resolution of the $x - z$ plane was completed for grid sizes of 20, 10, 5, and 2 mm; with sufficient convergence being seen at the 5 mm resolution.

The gauging section was located so that the magnitude of the longitudinal distance, x, from the crest was equal to: $4(D(x) - p)$, in accordance with measurement guidelines (Bos, 1976; Bureau of Reclamation, 2001). Measurements of D, and thus h, were made by evaluating the hydrostatic pressure head at the gauging section.

Numerical results were validated against the experimental results of Scimemi (1930); Rouse (1932); Rajaratnam and Muralidhar (1968) and case E0.68. Qualitative comparisons of the velocity field and nappe shapes between E0.68 and N0.68 showed good agreement (see Figure 5.3a and b). The values of Fr_h, along with the pressure (Figure 5.3c) and velocity (Figure 5.3d) profiles in the critical section produced from numerical simulations were found to be in good agreement with the available experimental data for similar cases of h/p. The normalized root mean squared error (NRMSE) values in the velocity profiles shown

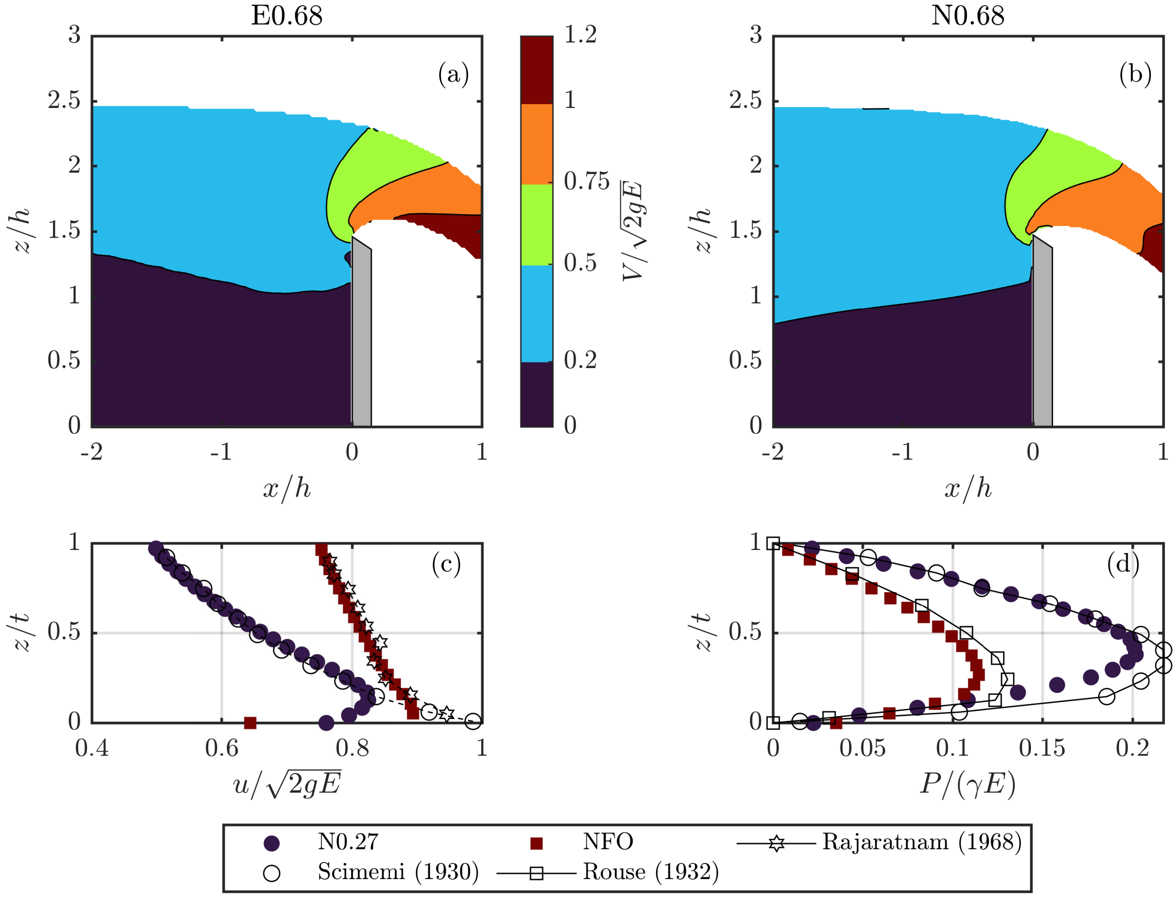

Figure 5.3: Comparison of dimensionless velocity magnitude field ($V = \sqrt{u^2 + w^2}$) from (a) PIV experiments (case E0.68) and (b) numerical simulation (case N0.68). (c) Comparison of streamwise velocity profiles in the critical section. (d) Comparison of pressure profiles in the critical section between experimental of previous authors and numerical results of the current study. For the data of Scimemi (1930) $h/p = 0.25$, and the data of Rouse (1932) and Rajaratnam and Muralidhar (1968) are both for the free overfall case.

in Figure 5.3c in comparison to the experimental profiles were 9.57% for case N0.27, and 8.17% for case NFO. In comparing the pressure profiles in Figure 5.3d, the NRMSE values were found to be 11.47% for case N0.27, and 9.08% for case NFO. It should also be noted that some deviation from the experimental velocity profile was seen in the numerical results near the lower nappe boundary. The location of maximum velocity for the numerical results tended to be slightly above the lower nappe boundary, whereas experimental and theoretical results have suggested that the maximum velocity in the profile should occur at this lower boundary. This discrepancy is likely due to the difficulty in reproducing numerically, and measuring experimentally, the shear layer that forms along the air-water interface of the lower nappe. However, these differences were confined to a thin region of the overall nappe. Overall, our numerical simulations did not produce significant deviations in the overall trend of results compared with the available experimental data.

5.5 Results

5.5.1 Revisiting the Weir-Discharge Equation

With a revised presentation of C_d as the weir Froude number, Fr_h, and the product of three component terms ($Fr_h = (2\sqrt{2}/3)C_v K C_c$) we now turn to the form of the function $\phi(h/p)$ in Eq. (5.7). Along with the current results from numerical simulation, we combine new experimental data with historical data found in the literature to examine the discharge-rating equation for thin weirs and sills. Figure 5.4 shows, quite remarkably, that a simple linear form of the weir-discharge equation provides an excellent fit to the data within the weir regime. This fit takes the form of the classical Rehbock equation without consideration of scale effects (Kandaswamy and Rouse, 1957), $C_d = 0.611 + 0.075h/p$, multiplied by $(2\sqrt{2}/3)$ so that:

$$Fr_h = \phi(h/p) \simeq 0.576 + 0.071h/p \, , \tag{5.18}$$

which is applicable in the range $Re_h > 3.5 \times 10^4$. A non-monotonic trend in Fr_h with h/p can be observed in Figure 5.4, with a maximum value of Fr_h occurring at $h/p = \mathcal{O}(10^1)$. The flow cases beyond this peak value and approaching the limit of the free overfall are considered to be in the sill regime. Kandaswamy and Rouse (1957) suggested a fit to the data in the sill regime, where $Fr_h \propto (h/p)^{-3/2}$. However, uncertainty in measurements is much greater in this regime due to variability in the water surface caused by friction losses, and surface waves.

The reason for the non-monotonicity in Fr_h with h/p is observed in Figure 5.4d to be due to the behavior of C_c, as was hypothesized earlier by Kandaswamy and Rouse (1957).

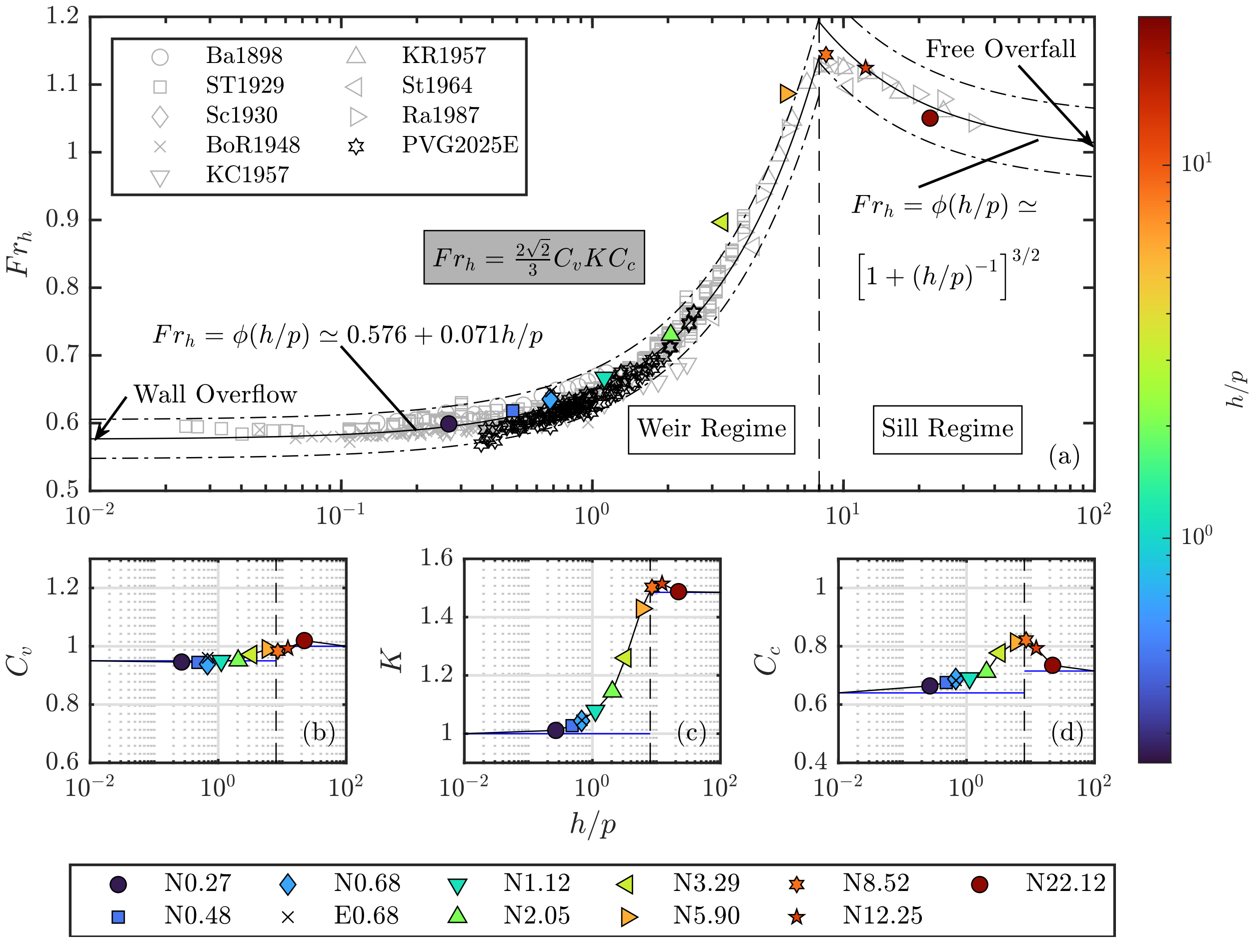

Figure 5.4: (a) Fr_h vs. h/p for the entire weir-sill range, with the historical data (Table 5.1) plotted. Classical empirical equations relating h/p and Fr_h are also shown by solid line, after Kandaswamy and Rouse (1957), with dash-dot lines representing ± 5% variation. For all data, $Re_h > 3.5 \times 10^4$. For cases shown in Table 5.2: (b) C_v vs. h/p, (c) K vs. h/p, and (d) C_c vs. h/p. Approximate values of C_v, K, and C_c for the upper and lower limits of h/p, representing the respective cases of the free overfall and wall overflow, are given by blue horizontal lines.

It is also seen that the coefficient K has the largest relative effect on the magnitude of Fr_h, and C_v the smallest. For planar orifice flows, C_v was found to range between 0.95-0.99, and accounts for local losses that occur in the shear layer formed near the sharp crest (Streeter, 1985). Thus, the value of C_v in the wall overflow limit shown in Figure 5.4b is taken to be 0.95. C_v in the free overfall limit is taken to be 1.0, which is akin to stating that local losses are negligible in this case. The trend in values shown in Figure 5.4b and Table 5.2 supports this. Rouse (1932) stated that the behavior of K in the wall overflow and free overfall limits should be 1 and 1.485 respectively, which can be shown to be true when it is recognized that the free overfall case is the critical flow condition where the channel Froude number, $Fr = q/\left(\sqrt{g}D^{3/2}\right)$, is unity.

From an analysis of orifice flows, it can be seen that for viscous fluids where $h/p \ll 1$, the value of C_c in the wall overflow limit should approach 0.64, so that $C_d = 0.611$ with $C_v = 0.95$ and $K = 1$. For the free overfall, Rouse (1936) showed that the value of this coefficient should be approximately 0.715, which again is derived from the assumption of critical flow conditions. Overall, the behavior of these three constituent coefficients from the results of the current study shown in Figure 5.4 agrees well with the current understanding in the literature.

5.5.2 Examining Flow Dynamics

To elucidate the data trends observed in Figure 5.4, pressure and velocity profiles within the critical section are shown in Figure 5.5 for flow cases given in Table 5.2. It can be seen in Figure 5.5(a) that a monotonic trend in streamwise inertia is observed with increasing h/p, which is the reason for the trend in K observed in Figure 5.4(c). The integral of the pressure profiles in Figure 5.5(b) exhibits a decreasing trend in response to the increasing velocity. It should also be noted that the velocity profiles become more uniform as h/p increases, and that an apparent self-similarity is present in both the velocity and pressure profiles for $h/p \leq\sim 2$. This fact has been recognized by earlier authors (Montes, 1998; Castro-Orgaz and Hager, 2017), who have shown that an analytical solution from potential flow theory is available for the coupled velocity and pressure profiles in the critical section for h/p values in this range. However, further experimental investigation is required to validate these preliminary findings.

To help explain the trends in C_c observed in Figure 5.4(d), Figure 5.6 plots the contours of the dimensionless vertical pressure gradient. Upon examination of Eq. (5.1), it can be seen for the convergent, steady and two-dimensional flow cases analyzed here, the greatest influence on the vertical pressure gradient ($\partial P/\partial z$) will come from the vertical inertia ($u\frac{\partial w}{\partial x} + w\frac{\partial w}{\partial z}$)

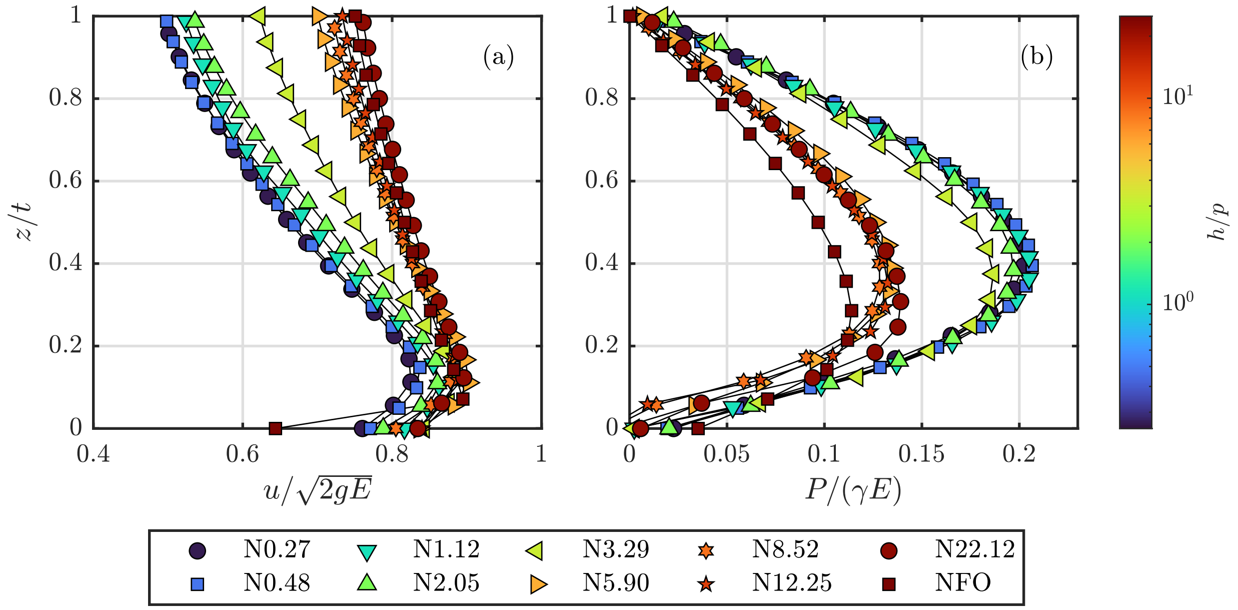

Figure 5.5: (a) Streamwise velocity profiles in the critical section. (b) Pressure profiles in the critical section. E is the minimum specific energy (see Figure 5.1).

terms. In the absence of vertical inertia, a hydrostatic pressure condition is present. When the sum of the vertical inertia terms is equal to the gravitational acceleration, the nappe falls as a zero-pressure-gradient (ZPG) jet. The transition from primarily 1D hydrostatic open-channel flow to a free-falling jet can be seen in Figure 5.6. Upstream of the weir and away from any boundaries, the velocity distribution is uniform, and horizontal streamlines result in a hydrostatic pressure distribution.

If the obstacle is large enough, flow separation occurs due to an adverse pressure gradient, creating a recirculation zone on the upstream corner formed by the channel bed and the weir. The boundary layer eventually reattaches along the vertical weir face, and then the fluid accelerates upwards toward the crest with significant vertical inertia. This, along with approach stagnation at the weir face, results in a zone of reinforced hydrostatic pressure just below the crest ($-(\partial P/\partial z)/\gamma > 1$). As the flow springs from the crest, gravitational effects work against the upward vertical inertia along the lower nappe surface, causing it to decelerate and create an adverse pressure gradient zone ($-(\partial P/\partial z)/\gamma < 0$). On the upper nappe surface, draw-down effects caused by the weight of the falling jet reduce the

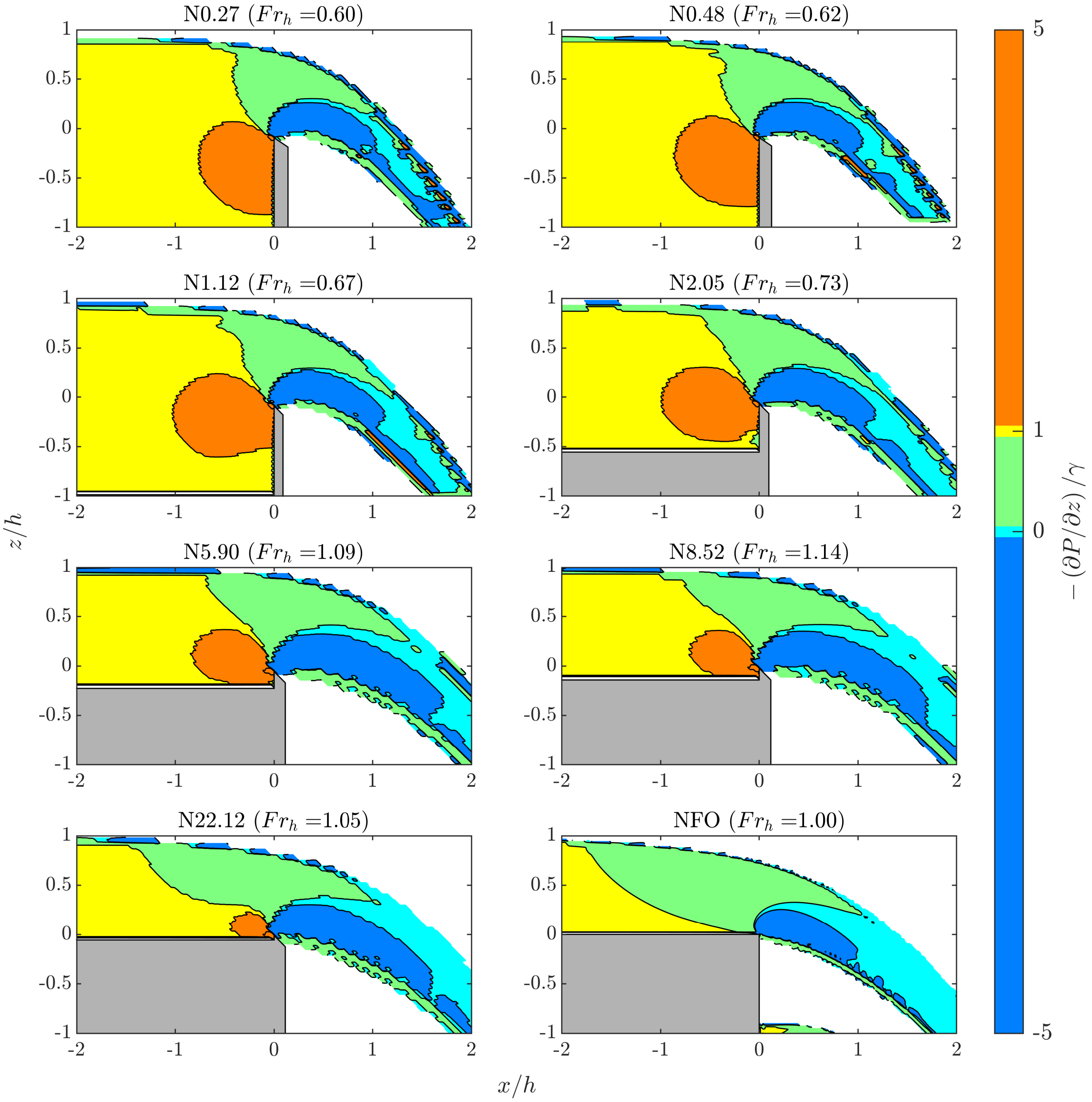

Figure 5.6: Dimensionless contour plots of the vertical pressure gradient for data summarized in Table 5.2.

hydrostatic pressure gradient ($-(0 < \partial P/\partial z)/\gamma < 1$). These two opposing gradients on the upper and lower surfaces of the nappe work against the remaining pressure until the flow becomes a free-falling jet with atmospheric pressure throughout its whole thickness.

Observing the trend in ε/h with h/p shown in Table 5.2 reveals that at small values of h/p contraction effects along the lower nappe surface are significant due to the relatively large amount of upward vertical inertia along the weir face that must be navigated around the sharp crest. This results in local losses, causing $C_v < 1$. As h/p increases towards the free overfall, the contraction is initially reduced as streamwise inertia increases and the streamlines in the approach flow become more horizontal. However, increased draw-down in the free surface (δ/h) occurs in the sill regime due to the insufficiency of the sill to cause any appreciable flow separation and stagnation near the crest, which in the weir regime allowed for the retainment of supportive pressure below the nappe. These combined effects explain the observed non-monotonic trend in Fr_h with h/p.

5.5.3 The Weir and Sill Regimes

With an understanding now established of the flow dynamics occurring within the wall overflow and free overfall limits, we turn to considerations for flow measurement. It should be noted that entrance into the sill regime comes with increased practical complications. As h/p grows, the relative influence of the turbulent boundary layer on the flow field also increases (Rouse, 1964), and increased mixing caused by turbulence results in a greater energy dissipation rate and friction slope. Eventually, the friction slope becomes appreciable enough that the free surface can no longer be assumed to asymptotically approach a horizontal line. Rouse (1936) recognized this, and noted that for the free overfall case, the critical depth, D_c (which for the free overfall is equivalent to the gauging depth) could be consistently located at an upstream distance from the crest equal to $4D_c$. However, it should be noted that this guideline must be met through successive iteration because q is not known *a priori*, and thus neither is D_c.

Figure 5.7 shows how the friction slope increases with h/p. Above a h/p value of $\sim$5, small deviations in the location of the gauging section measurement can lead to variations in the estimation of Fr_h greater than 2%. This is consistent with the findings of other authors (Kindsvater and Carter, 1959; Sinclair et al., 2022). Additionally, as Fr_h approaches unity, surface waves become more significant, further complicating a reliable measurement of h. It

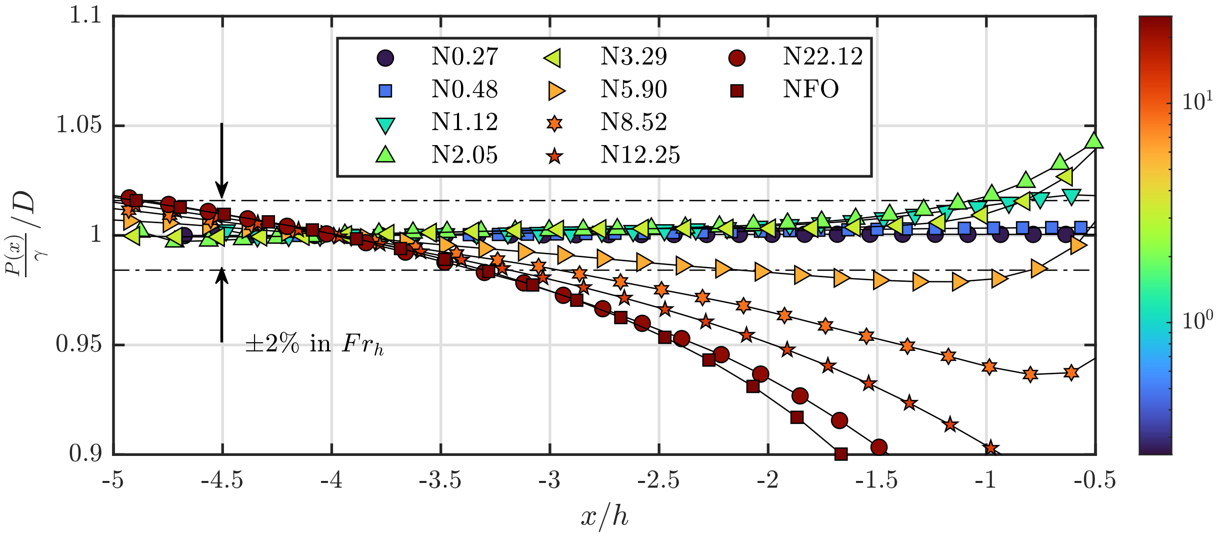

Figure 5.7: Pressure head on the channel bottom made dimensionless by the flow depth at the gauging section (located at a distance of $4h$ upstream of the crest), indicating changes in the flow behavior in the approach to the weir crest with varying h/p. Dash-dotted lines represent variation in the dimensionless flow depth that indicate a ±2% variation in the estimation of Fr_h.

can also be seen that for values of $h/p <\sim 8$, the bed pressure in the approach to the crest increases or at least is held constant, whereas for flow cases above this threshold, the bed pressure drastically begins to decrease towards the crest. This is evidence of flow separation and stagnation being present for $h/p <\sim 8$, and absent otherwise.

The previous studies of Kandaswamy and Rouse (1957) and Ramamurthy et al. (1987) implicitly suggest that the practical application range of weir flows with regard to h/p is unlimited, so long as a sufficiently large drop in the bed elevation is present to allow for full ventilation of the overflowing nappe. Ramamurthy et al. (1987) identified two regimes for these types of flows: for $h/p \leq 10$ the flow was considered weir flow, and for $h/p > 10$ the flow was considered sill flow. The maximum discharge capacity was found to be at the transition point of $h/p = 10$. However, defining this threshold based solely on h/p lacks a physical justification. To investigate this transition, we plot in Figure 5.8 the data summarized in Table 5.1, showing both Fr_h and h/p and against the channel Froude number, Fr.

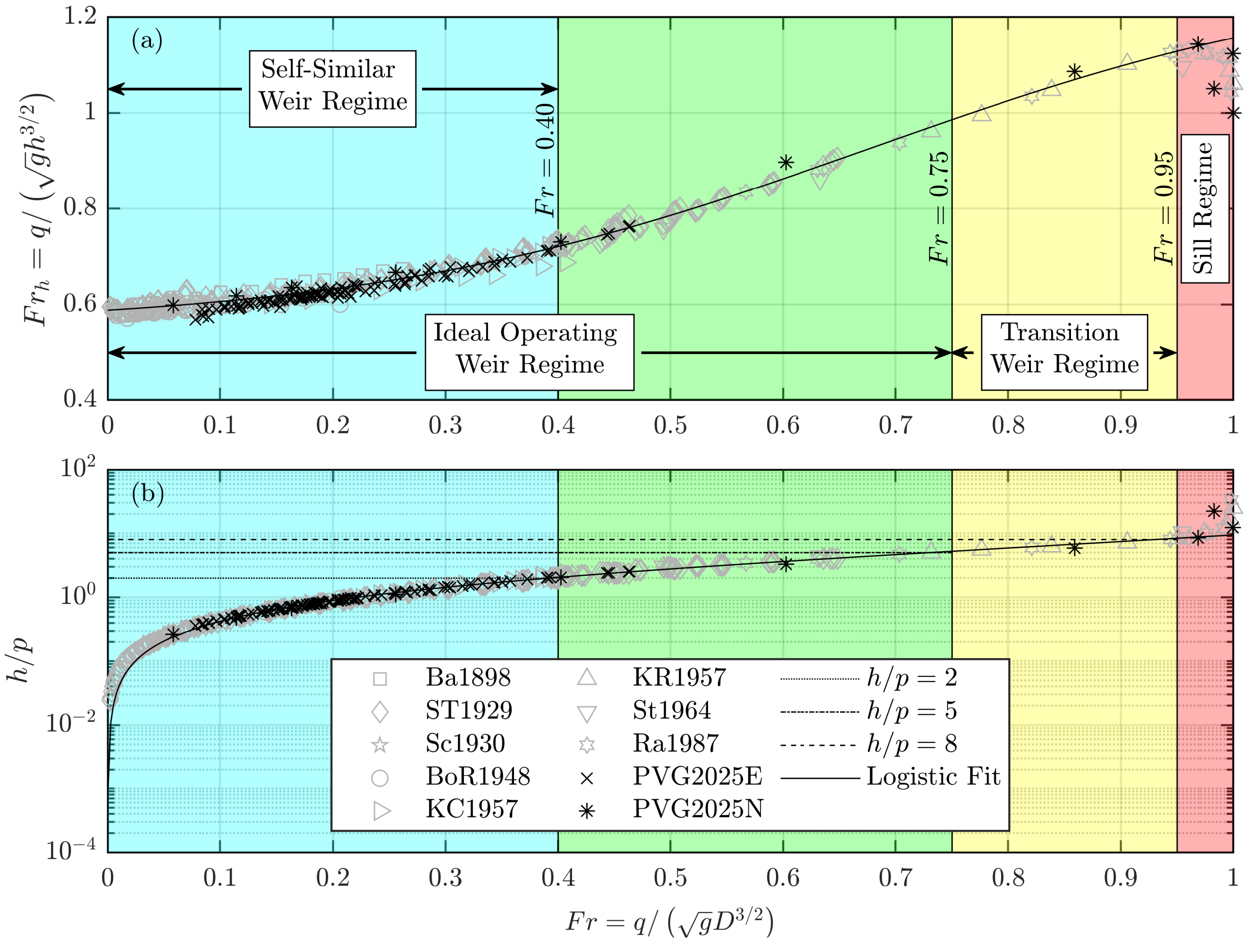

Figure 5.8: Dependency of (a) Fr_h and (b) h/p with the channel Froude number, Fr. The black trend line indicates a logistic relationship between the two variables. Respective limits for the self-similar, ideal operating, transition, and sill regimes are given.

5.6 Limitations and Practical Considerations

Figure 5.8 reveals that Fr_h and h/p exhibit a logistic relationship with the channel Froude number, $Fr = q/\left(\sqrt{g}D^{3/2}\right)$, until a distinct break point at approximately $Fr = 0.95$. From examining Figure 5.8(b), this value is equivalent to $h/p \simeq 8$. These trends reveal that the weir flow regime exists for up to 95% of the critical Fr, after which it enters into an unstable regime characteristic of sill flow. However, Figure 5.7 reveals practical limitations of accurately measuring h above a h/p value of 5. We therefore suggest that the ideal operating regime for weir flows be considered as $Fr < 0.75; h/p < 5$, with a transition regime between high-inertia weir flows and sill flows existing in the range $0.75 \leq Fr < 0.95$. A practical upper limit of $h/p = 5$ has been suggested by other authors (Kandaswamy and Rouse, 1957). However, in pursuit of even further precision, one could also suggest that weir flows used in practice should remain below the threshold of $h/p = 2$, equivalent to $Fr \simeq 0.4$, so that the velocity and pressure profiles within the nappe critical section remain self-similar - as was observed in Figure 5.5. This practical upper limit of $h/p = 2$ for accurate flow measurement is one that can be found in several previous reliable studies (Kindsvater and Carter, 1959; Castex, 1969; Ackers et al., 1978). Furthermore, other authors have suggested an upper limit of $Fr = 0.5$ for flow measurement using long-throated flumes to avoid wave action on the free surface that hinders an accurate measurement of h (Bureau of Reclamation, 2001; Bos et al., 1984). Finally, it should be noted that the sill regime ($Fr > 0.95$) does not represent a realistic condition for flow measurement due to the breakdown in the monotonic trend between h/p and Fr_h that renders the weir-discharge equation unusable, and the difficulty of defining the gauging depth due to a considerable friction slope and free-surface fluctuations.

5.7 Conclusions

Dimensional analysis has been well-leveraged in the past to develop functional and intuitive engineering solutions to classical hydraulics problems, such as for pressure losses in closed conduit flow. The weir discharge equation has thus far relied upon a derivation taken from its treatment as an orifice problem, but without much consideration for the relevant physical mechanisms at play. This has lead to ambiguity in a physical explanation of the weir discharge coefficient, C_d. We show how dimensional analysis using Buckingham Π theorem provides fundamental insights on the traditional weir-discharge equation, namely that C_d is most fundamentally a ratio of inertial to gravitational effects, represented by the dimensionless weir Froude number, Fr_h, equal to $(2\sqrt{2}/3)C_d$. Its behavior is governed by the combined effects of local friction losses, upstream flow inertia, and contraction in the overflowing nappe. The contribution of flow inertia to the overall discharge characteristics was found to be the most significant factor, with the non-monotonic trend in the contraction coefficient helping to delineate a transition between weir and sill flows. We investigate a physical explanation for the transition from weir to sill flow, finding that the growth rate of Fr_h with h/p is linear over a large range of the subcritical flow regime, until the channel Froude number, $Fr = q/\left(\sqrt{g}D^{3/2}\right)$ is approximately equal to 0.95. Above this threshold, the flow becomes unstable as it reaches criticality, with the stagnation pressure at the base of the weir diminishing so that increased free-surface draw-down of the overflowing nappe causes a marked increase in contraction and a reduction in discharge capacity. A practical upper limit of the ideal operating regime for weir flows is defined as $Fr = 0.75$ due to the increased effect of boundary friction and free-surface slope above this threshold, while $Fr \leq 0.4$ is found to be a threshold for self-similarity in the pressure and velocity profiles.

The results of this study can help inform practicing hydraulic engineers working with weirs on 1) a physical basis for the discharge capacity of a structure, and 2) regarding what effects are primary and secondary in determining C_d. A clear delineation between weir and sill flows helps ensure that flow measurement practices are completed in the most reliable regime. Together, these insights will help in providing engineers with practical guidance on the design, calibration, and operation of overflow structures to achieve accurate and dependable discharge measurement and regulation.

Chapter 6

Discharge Equation for Tilting Weirs [2]

6.1 Introduction

Tilting weirs (i.e., overshot gates or pivot weirs) have been in use since the late twentieth century for the purpose of regulating upstream water levels in open-channel flow, typically within the context of irrigation systems or spillway operation (Wahlin and Replogle, 1994; Stringam and Gill, 2012; Lee et al., 2014; Bijankhan and Ferro, 2017). These simple overflow structures operate as a flat rectangular plate that is hinged to the bottom of the channel and inclined from the horizontal through the use of pneumatic pressure vessels, a pulley mechanism, or a piston mechanism. It is generally assumed that the crest of these structures is thin, so that a springing jet (i.e., nappe) forms on the downstream side of the structure. In irrigation systems, tilting weirs allow for regulation of the stage upstream of the structure to provide the pressure head necessary to divert flow from a main supply canal into lateral canals. In spillway operation, these structures can be installed in parallel to allow for careful release of flows and regulation of the reservoir stage in response to varying supply and demand levels.

Tilting weirs require careful consideration of aeration demands for the underside of the plunging nappe to be supported by atmospheric pressure (Bos, 1976). If these structures are properly designed, the downstream channel bed elevation will be set low enough to allow for the energy of the supercritical plunging nappe to be dissipated, while also ensuring that a sufficient supply of fresh air is provided to the pocket of atmospheric pressure supporting

---

[2] The research presented in this chapter has been published in the *Journal of Hydraulic Engineering* under the title "A Novel and Enhanced Calibration of the Tilting Weir as a Flow Measurement Structure" by J.E. Pugh, S.K. Venayagamoorthy, T.K. Gates, C. Bérni, and M. Rastello. This chapter is written to reflect and acknowledge the contribution of the co-authors. A closure article in response to two discussion pieces submitted in response to our manuscript is also available at: https://doi.org/10.1061/JHEND8.HYENG-14420.

the nappe. For these reasons, tilting weirs offer the potential of being practical hydraulic structures that serve the dual functions of stage regulation and discharge measurement. The initial development of these structures as stage regulation devices has been well documented and widely implemented (Clemmens et al., 2001; Floodlist News, 2017). However, their use as flow measurement devices remains in need of further investigation.

6.1.1 Fundamentals of the Weir Rating Equation

The development of a method for predicting the volumetric discharge over tilting weirs begins with an understanding of Torricelli's principle of a jet at the base of a reservoir issuing from a small orifice. Here, the velocity (u) of the jet can be related to the potential energy in the static supply reservoir by the function $u = \sqrt{2gh}$, with h being the elevation of the water surface above the jet outlet. This principle assumes the flow is inviscid and irrotational, and that the pressure distribution over the crest is hydrostatic. In his 1717 publication "de moto aquae mixto", Giovanni Poleni applied Torricelli's principle to approximate the discharge of a fluid over a perpendicular weir as occurring in a series of horizontal elements, the velocity of each being proportional to the distance of the fluid element from the free surface (Rouse and Ince, 1963). From the resultant parabolic velocity profile, the depth-integrated unit discharge (q) can be approximated using what is known as Poleni's equation:

$$\int_0^h u \, \mathrm{d}h \approx \frac{2}{3}\sqrt{2g}h^{3/2} \approx q \, . \qquad (6.1)$$

However, it is known that because of the simplifying assumptions implicit in Eq. (6.1), a dimensionless correction factor must be applied to the idealized efflux to account for the contraction of jet at the crest of the orifice. This has typically been called the discharge coefficient (C_d) when referring to weir flow, but it is in effect a coefficient of contraction (Kindsvater and Carter, 1959). Its application to Eq. (6.1), with the addition of the crest length (b) to account for the transversal dimension, then yields the standard volumetric discharge rating equation for a sharp-crested weir:

$$Q = C_d \frac{2}{3}\sqrt{2g}bh^{3/2}\,. \tag{6.2}$$

This relatively simple equation forms the theoretical basis for the discharge equation of different types of sharp-crested weirs with variable geometries (Martínez et al., 2005). However, the simplifying assumptions of this approach should not be overlooked. As previously mentioned, this derivation approximates the flow between the upstream head measurement location and the crest as being inviscid and irrotational. A zero-pressure gradient is also assumed at the crest. For the case of accelerating flow over a weir, it is often taken to be a safe assumption that over the short reach from the measurement section to the crest, the energy loss due to internal rotational shear is negligible (Kindsvater and Carter, 1959).

The assumptions of inviscid flow and a hydrostatic pressure distribution can be best examined by considering the theoretical case of a sharp-crested weir of infinite height. Here the assumption of potential flow is valid because the effect of the boundary is negligible. For this case, the streamlines will approach the crest radially so that a significant vertical velocity component will be present in the flow. This causes the pressure distribution to decrease significantly from the hydrostatic condition. This pressure drop correspondingly results in an acceleration of the flow over the crest and a reduction in the depth of flow at the crest to satisfy the continuity principle (Rouse, 1932). The contraction coefficient of the water surface profile over the crest of an infinitely high weir has been shown from potential flow theory to be equal to Kirchhoff's coefficient for a jet issuing from a sharp-edged orifice, where $C_d = \frac{\pi}{\pi+2} = 0.611$ (Rouse, 1946c).

If a low weir is considered, so that the effect of the boundary cannot be neglected and the assumption of inviscid flow no longer holds, it can be observed that the flow separates near the base of the weir and a standing eddy forms. This phenomenon was briefly verified in this study by preliminary particle-image velocimetry analysis, as shown by Figure 6.1. A boundary layer is present due to viscous effects causing a deceleration of the flow near the channel bed, as well as the upstream face of the weir. The magnitude of these respective boundary layers can be described by the boundary layer displacement-thickness (δ^*) (Kindsvater and Carter, 1959). The effect of the flow separation on the streamlines upstream of the weir was described by Rouse (1932) as being akin to tilting the weir downstream, due to the fact that the streamlines above the separation zone retain more horizontal momentum. This results in less curvature of the streamlines at the crest and less contraction of the overflowing jet, so that the pressure at the vena contracta more closely approximates the hydrostatic condition. The result is that for a low weir, more discharge can be passed given the same upstream energy condition compared to that for an infinitely high weir (Rouse, 1932).

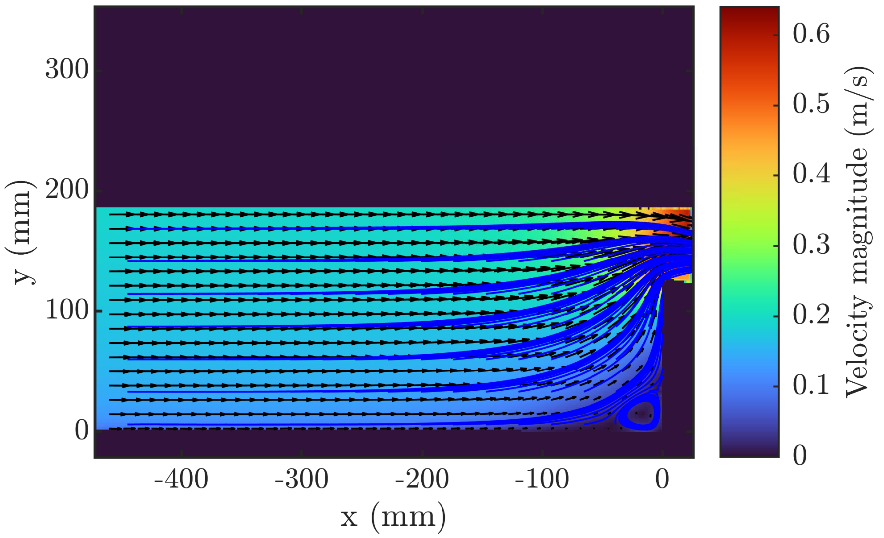

Figure 6.1: Velocity magnitude vector field computed from particle-image velocimetry, with streamlines shown in blue. A zone of separated flow is apparent at the base of the weir. Flow case is from Experiment O at the HHLab; with $\theta = 90°$, $p = 126$ mm, and $Q = 30$ Lps.

6.1.2 Dimensional Analysis

If the assumption is made that the tilting weir can be treated as a modified case of the classical sharp-crested weir, the general form of Eq. (6.2) can be applied to establish a head-discharge rating equation for the tilting weir by adding a term that accounts for the inclination angle (θ) of the weir with respect to the horizontal. In order to understand the relevant flow parameters and fluid properties that influence this equation, a dimensional analysis of the tilting weir is now considered.

Simplifying assumptions are made that the weir crest length (b) is equal to the width of the approach channel (B), and the velocity field is uniform in the transversal direction. The flow geometry can then be described by the parameters shown in Figure 6.2. Here, L is the vertical height of one weir when positioned perpendicular to the channel bed; p is the elevation of the weir crest above the channel bed at a given θ; and h is the piezometric head measured with reference to the crest elevation in the uniform flow section upstream from the weir. The total hydraulic head (H), is the sum of the piezometric head (h) and the kinetic energy head ($\alpha U_0^2/2g$), where U_0 is the velocity averaged over the channel cross-section in the approach, α is the kinetic energy correction factor, and g is the gravitational acceleration.

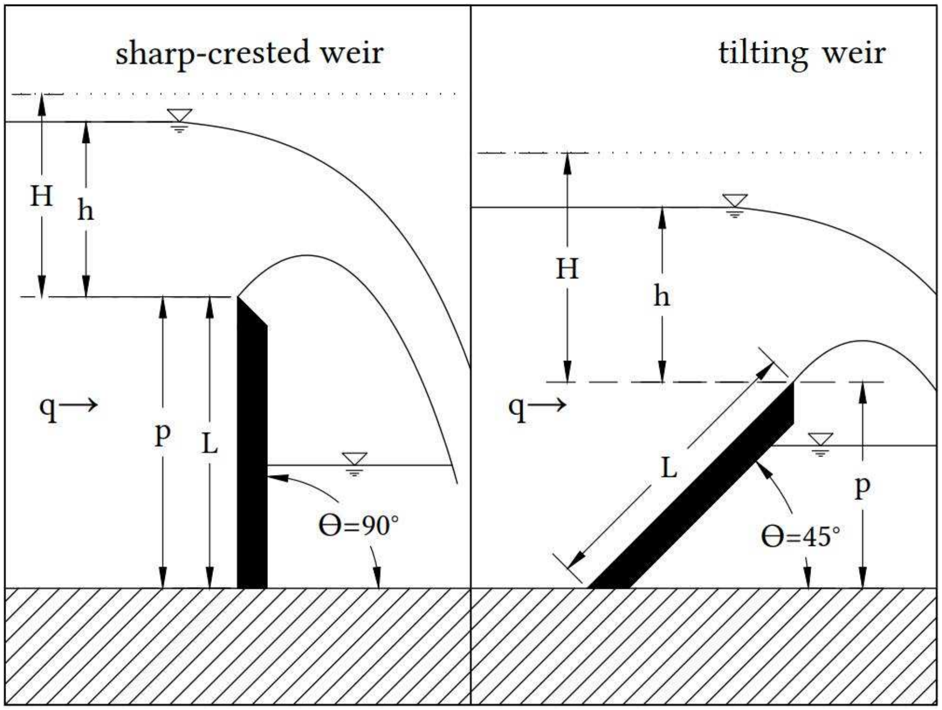

Figure 6.2: Schematic of flow over a weir.

The dimensionless term, $\sin\theta = p/L$ describes the effect that the changing angle of attack of the flow on the weir has on the streamlines over the crest, and relates p and L. The relevant fluid properties in determining the flow over the weir are the density, ρ, the dynamic viscosity, μ, and surface tension, σ. Since this is a case of open-channel flow, gravitational effects are critical and thus g is included as a relevant physical parameter. A functional description of the unit discharge over a fully suppressed $(b/B = 1)$ tilting weir can be written as:

$$q = f(p, h, \sin\theta, g, \rho, \mu, \sigma) \, . \tag{6.3}$$

Utilizing Buckingham π analysis and a yet to be determined function (ϕ), the following dimensionless equation can be written using the scaling terms $h \equiv \mathrm{L}$, $h/\sqrt{gh} \equiv \mathrm{T}$, and $\rho h^3 \equiv \mathrm{M}$:

$$C_d = \frac{3}{2\sqrt{2}}\, Fr = \phi(h/p, \sin\theta, Re, We) \, , \tag{6.4}$$

wherein:

$$Fr = \frac{q}{\sqrt{g} h^{3/2}} \, , \tag{6.5}$$

$$Re = \frac{\sqrt{g} h^{3/2}}{\nu} \quad (\text{where} \;\; \nu = \mu/\rho) \, , \tag{6.6}$$

$$We = \frac{\rho g h^2}{\sigma} \, . \tag{6.7}$$

The first term in Eq. (6.4) is the classical discharge coefficient as shown in Eq. (6.2), which can be considered as a dimensionless Froude number (Fr) for the flow over the weir crest $(q/\sqrt{g} h^{3/2})$, that has then been transformed by the coefficient $3/2\sqrt{2}$ to make the inertial term in the numerator reflect the depth-averaged velocity from Poleni's approach in Eq. (6.1).

Regimes of flow over a weir can be divided into four types: clinging, laminar, free, and inundated flow (Johnson, 1996; Sinclair et al., 2022). These regimes and their respective effect on the shape of the nappe were first described by Bazin (1898), and later summarized by Rao (1975). When the flow over the weir is clinging, its inertia is not sufficient to overcome scale effects due to surface tension. Here, the free surface clings to the weir plate and the nappe downstream of the crest is not fully formed. This causes the same discharge to pass over the weir at a lower head compared to when the nappe is fully formed, thus artificially increasing the discharge coefficient (Sarginson, 1972). An additional flow regime can occur at low heads, even when the nappe is no longer clinging to the downstream face. This flow regime has also been described as a depressed nappe (Rao, 1975). Here, viscous effects rather than surface tension effects are dominant. The flow inertia is not sufficient to overcome viscous effects in the same manner that is observed within the free flow regime; hence the velocity profile deviates from that expected for turbulent open-channel flow (Rouse, 1946a). This reduction in the upstream bulk velocity causes h over the weir to artificially increase in order to satisfy conservation of mass, thus decreasing C_d below what is expected for the free flow relationship (Schoder and Turner, 1929). Inundated flow occurs on the opposite end of the inertial spectrum, but the effect on C_d is nominally the same as for clinging flow. Here, the pressure head above the weir becomes too great for the air pocket beneath the nappe to be sustained, the nappe collapses, and the head over the weir decreases. Free flow then occurs in between the limits of clinging/laminar and inundated flow, when the weir is operating within the conditions assumed in Eq. (6.2). This means that dynamic similarity is present so that the flow dynamics are independent of viscous and surface tension scale effects, and that the nappe downstream of the crest is fully supported by a fresh supply of air at atmospheric pressure.

If viscous and surface tension effects are taken to be negligible within the normal operating parameters of the weir, then determining the head-discharge equation over a tilting weir converges upon an understanding of how C_d behaves as a function of the dynamic parameters h/p and $\sin\theta$. As Rouse (1932) speculated, the reduction in $\sin\theta$ is likely to have the same effect as increasing the h/p ratio, by which the streamlines become more horizontal over the crest and the contraction coefficient increases to allow more discharge over the weir, given the same upstream head condition. The goal of this study is to determine the behavior of the discharge capacity of a tilting weir as it relates to h/p and $\sin\theta$, as well as the range of

Reynolds number (Re) and Weber number (We) values that can be considered as a normal operating regime for free flow.

6.2 Review of Previous Work

6.2.1 Sharp-Crested Weirs

Much careful experimental work was completed on the flow measurement equation for sharp-crested weirs from the late-nineteenth until the mid-twentieth century to find an empirical equation to relate C_d (as in Eq. (6.4)) to h/p under normal operating conditions, *i.e.*, when Re and We effects can be neglected. Notable works on this topic are those of Smith (1886), Bazin (1898), Rafter (1900), Horton (1906), Schoder and Turner (1929), King et al. (1929), and Bureau of Reclamation (1948).

A seminal work on the topic that aimed to integrate the work of previous researchers, while offering a large amount of new experimental data, was that of Kindsvater and Carter (1959). These researchers at Georgia Tech University offered the novel contribution of taking into consideration viscous and surface tension effects that become relevant at low values of h. They also considered the effect on the flow dynamics for weirs where $b/B < 1$. Kindsvater and Carter (1959) convincingly showed that earlier formulas for C_d in Eq. (6.4) of a nonlinear form were overly complex, and that a simple linear equation could be used instead. They also suggested the use of empirically calibrated correction factors, k_h and k_b to account for Re and We scale effects under small values of h and b, introducing equivalent head (h_e) and equivalent crest length (b_e) terms to obtain an effective discharge coefficient (C_e) for sharp-crested weirs:

$$C_e = \frac{Q}{\frac{2}{3}\sqrt{2g} b_e h_e^{3/2}} \approx 0.602 + 0.075h/p \,, \tag{6.8}$$

with

$$h_e = h + k_h \,, \tag{6.9}$$

$$b_e = b + k_b \,. \tag{6.10}$$

The authors recommended the use of a k_h value of 0.003 ft, or approximately 1 mm. The use of k_h is important only when values of h are small. For water flow through air, Kindsvater and Carter (1959) estimated that prediction error due to viscous and surface tension effects would be within 2% as long as $h > 0.06$ m. It was also emphasized that k_h is an empirically calibrated correction factor that could differ significantly depending on which set of experimental data was used. The original authors attributed this to differences in experimental equipment. However, we hypothesize that this discrepancy may be due to the fact that at low values of h, either We or Re effects can be dominant depending on whether the nappe is fully formed or not. Evidence for this bifurcation in the flow behavior at low h is given in Zhang et al. (2010). By giving k_h as a positive parameter, Kindsvater and Carter (1959) implicitly assumed We effects to be dominant at low values of h, as explained earlier. Therefore, the specific choice of k_h may be a point in need of finer calibration on a case by case basis, but we report here the recommended value $k_h = 0.001$ m of the original authors. A less uncertain choice is the value of k_b. Kindsvater and Carter (1959) found little variability in the value of this parameter within the experimental data they examined, likely because it is a function of the static contraction ratio parameter, and not the dynamic variable h. They recommended a k_b value of -0.003 ft (-0.001 m) for the case where $b/B = 1$.

After the work of Kindsvater and Carter (1959), several other publications have further elucidated the nature of sharp-crested weir flow over a wide range of h/p values, including measurements of velocity and pressure distributions near the crest. (Rajaratnam and Muralidhar, 1971; Ramamurthy et al., 1987; Swamee, 1988; Sinclair et al., 2022).

6.2.2 Tilting Weirs

With the early explorations of the sharp-crested weir as a flow measurement device, examinations were also made to investigate the effect that tilting the upstream face of the weir had on the nappe profiles, and on the head over the crest at a constant discharge (Bazin, 1898; Bureau of Reclamation, 1948; Abou Seida and Quaraishi, 1976). Hager (1994) compiled the data from several of these types of studies to develop a flow-rating equation for tilting weirs of the form:

$$Q = \left[\frac{2}{3}C_e + 0.05\sin\left(\frac{3}{2}(90-\theta)\right)\right] b\sqrt{2g}h^{3/2}\,. \tag{6.11}$$

where C_e is Eq. (6.8) of Kindsvater and Carter (1959), the effective discharge coefficient for a sharp-crested weir, and θ is in degrees. The second term in the brackets on the right-hand side of Eq. (6.11) accounts for the effect of the changing θ on the overall discharge capacity of the structure. This study, published in German, represents an interesting first investigation into the flow-rating equation of a tilting weir. However, it was limited by the fact that the early experimental studies cited by Hager (1994) and used for calibration did not cover a wide range of flow conditions (i.e., h/p values).

The seminal work to date attempting to develop a flow-rating equation for tilting weirs is that of Wahlin and Replogle (1994). The authors of this technical report studied two models in a large flume ($B = 1.2$ m). As predicted earlier by Rouse (1932), they began with the assumption that the general form of the sharp-crested weir rating equation, as given by Kindsvater and Carter (1959) in Eq. (6.8), could be applied to the modified case of the tilting weir with the addition of a corrective factor to account for variation in θ. They chose to call this term C_a. By studying data previously collected by the US Bureau of Reclamation (USBR) in analysis of the nappe profiles for flow over variously inclined weirs (Bureau of Reclamation, 1948), the authors hypothesized that the relation between C_a and θ would take the form of a second order concave polynomial. C_a can also be thought of as a discharge amplification factor, Q_θ/Q_{90}, which represents the relative effect of θ on the amount of discharge that is able to pass over the structure at a given head, compared to the perpendicular 90° case. The results of the study proved to be fairly true to the original hypothesis, and a second order polynomial was defined as: $C_a = 1.0333 + 0.0038848\theta - 0.000045\theta^2$, with θ in degrees. Although by definition C_a should be unity when $\theta = 90°$, the authors did not verify this experimentally, and their empirical equation for C_a does not reflect this.

Furthermore, the number of observations in their study for $\theta > 45°$ were limited. For $\theta = 54.2°$, 14 data points were collected over an h/p range of 0.11-0.3 ($0.04 < h < 0.11$ m), and for $\theta = 63.4°$ only seven observations were made over an h/p range of 0.09-0.22 ($0.03 < h < 0.09$ m). With such small values of h, the observations may have been subject to We and Re scale effects (King et al., 1929; Kindsvater and Carter, 1959). Thus, it is a concern of the current authors as to whether applying the inclination-angle correction factor given by Wahlin and Replogle (1994) for $\theta > 45°$ is advisable. Wahlin and Replogle (1994) did report that when using their approach for $20° < \theta < 45°$, an average percent error of only 0.8% was found in their predictions of the laboratory data. At the very least, this means there was low prediction bias for their approach within this range of θ. From the experimental data published in the appendix of the study, the current authors computed the mean absolute value percent error (MAPE) to be 2.5% for this same case, which gives a more complete understanding of the magnitude of residual error from this approach. When applying the laboratory-derived equation to a field-scale structure, it was found that their equation under-predicted the discharge in the field by an average of 6.34% (Wahlin and Replogle, 1994). This raises the question of how directly applicable laboratory-calibrated discharge-rating equations are to field conditions (Hajimirzaie and González-Castro, 2020).

Since the first study of Wahlin and Replogle (1994) little convergence has been observed in the published experimental data on flow over the tilting weir. Prakash et al. (2011) conducted a laboratory experiment of flow over inclined rectangular notched weirs, with $\theta =$ 30°, 45°, 60°, 75°, and 90°. They found that the discharge capacity of the structure increases as θ decreases, and proposed an equation containing two fourth-order polynomials to account for this effect that was accurate to within 10%. However, the authors did not validate their findings with previous experimental data for flow over sharp-crested weirs, and their data have since found little agreement with results published by subsequent authors.

Work completed in South Korea has focused on studying the flow characteristics of free and submerged flow over tilting weirs, as well as how sedimentation patterns are affected by the inclination angle of the weir (Lee et al., 2014, 2016; Lee, 2018). These works have suggested incorporating the upstream total hydraulic head (H) into the tilting weir rating equation in order to model the effect of θ on the flow. However, this suggestion does not offer the most practical means of implementation in the field, where measuring the kinetic energy head in the approach channel is difficult. Unfortunately, these works have also yet to be published in English; thus their applicability to the wider engineering community remains obscure.

Nikou et al. (2016) investigated tilting weirs in a laboratory setting with different side contractions for $\theta = 20°$, $40°$, $60°$, $80°$, and $90°$. However, these authors made their observations over only a small number of discharge scenarios, which resulted in calibration of the empirical coefficients to only ± 15 % in prediction accuracy. Additionally, in a discussion piece, Khalili Shayan et al. (2018) convincingly showed that the assumption of the original authors that critical flow occurs over the weir crest was inaccurate.

Bijankhan and Ferro (2018) attempted to develop a rating equation for the tilting weir that was meant to be independent of the dynamic head over the structure as measured by h/p. This form is simpler in the sense that it depends on fewer parameters, but also less accurate because it neglects how C_d increases linearly with h/p (Kandaswamy and Rouse, 1957). Furthermore, Bijankhan and Ferro (2018) did not explain how a fresh air supply was provided underneath the nappe to ensure the condition of atmospheric pressure. From the experimental photos published by the authors, it appears the flow was not sufficiently aerated and thus subject to inundation effects, especially at low θ values where the relative difference between the crest elevation and tailwater depth is small. Furthermore, in a discussion piece on a follow-up study that Bijankhan and Ferro (2020) completed over submerged tilting weirs, Hajimirzaie and González-Castro (2020) revealed a flaw in the dimensional analysis of the authors, originally developed by Ferro (2012). This error introduces a spurious correlation between the independent and dependent dimensionless parameters. This leads to the perceived conclusion that C_d, as in Eq. (6.4), is independent of h/p. Several experimental investigations have shown that this conclusion is incorrect (Kandaswamy and Rouse, 1957; Wahlin and Replogle, 1994; Sinclair et al., 2022).

Other researchers have studied the flow characteristics of tilting weirs using numerical modeling. Mahdavi and Shahkarami (2020) utilized smoothed particle hydrodynamics to provide helpful visualizations of the flow field both upstream and downstream of the weir crest. The authors also validated their simulations with good agreement to available data from physical experiments, at least when $\theta = 90°$. However, the authors did not study a sufficiently large number of flow scenarios to accurately calibrate a head-discharge equation dependent on θ. Khatamipour et al. (2022) studied Reynolds-averaged Navier-Stokes (RANS) simulations of flow over tilting weirs in Open FOAM using a two-dimensional k-ε turbulence model over 12 flow cases. The authors observed similar behavior to Wahlin and Replogle (1994) in the relationship between Q_θ/Q_{90} and θ, but at smaller magnitudes of Q_θ/Q_{90} than the original study. It was also apparent from the published qualitative flow images that the flow was submerged for $\theta < 90°$, and thus not viable for calibrating a free-flow rating equation.

Most recently, Zerihun (2022) presented a flow-rating equation for tilting weirs derived from first principles using the Boussinesq-type energy equation for depth-averaged flow. This allowed for the creation of a numerical code that accounted for the presence of non-hydrostatic effects in the subcritical to supercritical transition region near the crest of the tilting weir. The results of the numerical simulations agreed well with the experimental nappe profiles of Bazin (1898) and Bureau of Reclamation (1948). However, the flow-rating equation presented by Zerihun (2022) lacks practical applicability in that it includes terms requiring a priori knowledge of the slope of the free surface and overflowing nappe.

To summarize, the consensus on how to properly treat the influence of θ on the flow characteristics of a tilting weir has so far been lacking in the literature. The initially proposed approach of Wahlin and Replogle (1994) has not been sufficiently validated for $\theta > 45°$, and the large majority of subsequent work has been lacking in experimental rigor. More recent work on determining the effect of the flow attack angle over other types of weirs has further highlighted that the influence of θ should not be neglected (Schmocker et al., 2011). Higher-order approaches, such as that presented by Zerihun (2022), offer promise for further exploration of this problem numerically but remain to be clearly linked to methods for practical implementation. In pursuit of that, we present here a thorough experimental effort at two unique geometric scales that entails a large number of careful observations across all relevant θ and h/p values for channel flow.

6.3 Experimental Setup and Measuring Devices

Experiments were first conducted in a recirculating flume manufactured by Armfield and located in the Environmental Fluid Mechanics Laboratory (EFML) at Colorado State University (CSU), USA. The flume was 5 m in length and 0.3 m wide, with a smooth neoprene channel bed and glass side walls. The flume slope was set to be horizontal. Beyond the inlet condition provided by the flume manufacturers, it was found necessary to install a honeycomb-like matrix of porous material at the flume inlet to straighten and normalize the incoming flow. Furthermore, a series of small roughness elements were installed just downstream of the honeycomb matrix in order to trip the turbulent boundary layer and reproduce as close as possible a fully developed open-channel velocity profile. The downstream channel boundary condition was a free overfall.

Nine tilting weir models were constructed at $\theta = 25.7°$, $29.1°$, $36.4°$, $45°$, $50°$, $53°$, $64°$, $71.2°$, and $90°$ by machining two sheets of smooth acrylic plastic of 12.7 mm (0.5 in.) thickness and adhering them together using a waterproof adhesive. The length of the weir plate (L), as shown in Figure 6.3, was consistent between all models at 150 mm. The crest of each model was precisely cut to be knife-edged, with the angle between the downstream-sloping crest and the parallel sides of the acrylic plates being 45°. Due to air entrainment caused by the plunging nappe, circular tubes of PVC plastic were also installed along the glass side walls of the flume to provide access to fresh air supply, as is shown in Figure 6.3. This ensured that the air pocket beneath the overflowing nappe was fully aerated to atmospheric pressure. The diameter of these tubes was sized to 19 mm (0.75 in.) according to specifications detailed in Bos (1976).

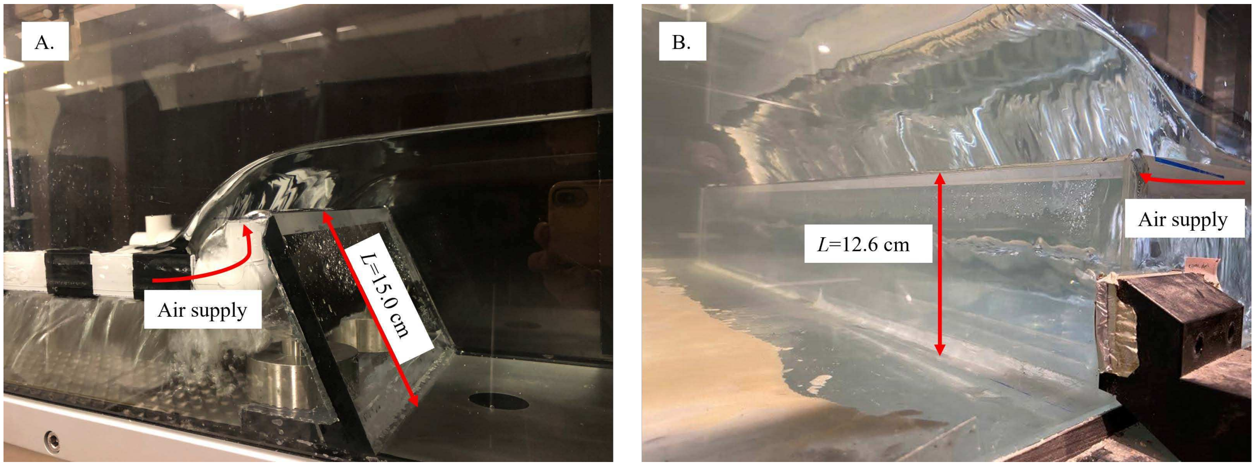

Figure 6.3: Experimental setups in the Environmental Fluid Mechanics Laboratory (A.) and Hydraulic and Hydromorphology Laboratory (B), showing placement of aeration tubes downstream of the crest and the location where fresh air was supplied to the underside of the overflowing nappe.

Measurements of h and steady Q were made over a full range of flow conditions for each model, ranging from clinging/laminar flow at the minimum, to fully inundated flow at the maximum. At least 20 observations were made within the free-flow regime, where dynamic similarity is achieved and the inertia of the flow is great enough to be free from scale effects caused by viscosity and surface tension, while also avoiding the under-pressurization of the nappe caused by inundated flow (see Table 6.1). These free-flow observations were used to calibrate C_e as a function of h/p for each model. Observations of h were made at a distance of 0.8 m upstream of the model crest using a vernier-type point gauge to an accuracy of ± 0.3 mm (0.001 ft). Measurement of steady Q through the flume was made using an electromagnetic flow meter located within the supply pipe to the channel with an accuracy of ± 0.3 L/s (0.01 cfs). Measurements of water temperature also were taken, at an accuracy of ± 0.1°C in order to precisely calculate temperature-dependent values for μ and σ.

Table 6.1: Description of experimental data collected. The number in parentheses after the number of observations per experiment (n) indicates the number of points used to calibrate the free-flow head-discharge equation. The range of h/p, Re_θ, and We_θ given for each experiment constitute the cases that were considered as free flow and used to calibrate the stage-discharge equation.

	Location	θ(°)	p (mm)	n	h/p		Re_θ		We_θ	
					min.	max.	min.	max.	min.	max.
A	EFML	25.7	65.0	27 (22)	0.50	0.94	2.0E+04	5.2E+04	1.6E+02	5.7E+02
B		29.1	73.0	26 (21)	0.57	0.91	2.9E+04	5.9E+04	2.7E+02	6.7E+02
C		36.4	89.0	36 (29)	0.36	0.98	2.0E+04	8.8E+04	1.6E+02	1.1E+03
D		45.0	106	43 (39)	0.38	0.97	2.7E+04	1.1E+05	2.4E+02	1.6E+03
E		45.0	106	23 (22)	0.43	1.05	3.3E+04	1.3E+05	3.1E+02	1.9E+03
F		50.0	115	20 (20)	0.35	0.96	2.8E+04	1.2E+05	2.5E+02	1.8E+03
G		50.0	115	27 (27)	0.34	1.02	2.6E+04	1.3E+05	2.2E+02	2.0E+03
H		53.0	120	50 (43)	0.43	0.99	3.9E+04	1.4E+05	3.9E+02	2.1E+03
I		64.0	135	27 (27)	0.32	0.99	2.9E+04	1.6E+05	2.7E+02	2.6E+03
J		71.2	142	27 (24)	0.39	0.95	4.1E+04	1.6E+05	4.2E+02	2.5E+03
K		90.0	150	27 (26)	0.24	0.93	2.2E+04	1.6E+05	1.8E+02	2.6E+03
L	HHLab	33.0	68.6	32 (27)	0.53	1.08	2.4E+04	7.0E+04	2.1E+02	8.5E+02
M		44.0	87.5	25 (20)	0.53	0.99	3.4E+04	8.7E+04	3.3E+02	1.1E+03
N		59.0	108	28 (24)	0.41	0.88	3.0E+04	9.6E+04	2.8E+02	1.3E+03
O		90.0	126	22 (21)	0.38	0.96	3.2E+04	1.3E+05	3.0E+02	2.0E+03

To ensure the initial results of the EFML experiments were both reproducible and scalable, follow-up experiments were conducted in a similar recirculating flume located in the Hydraulic and Hydromorphology Laboratory (HHLab) of the RiverLy research unit operating in the centre of the Institut National de Recherche pour l'Agriculture, l'Alimentation, et l'Environnement (INRAE) located in Lyon-Villeurbanne, France. This flume was larger than the EFML flume, at 1 m wide and 18 m in length, with a smooth glass channel bottom and side walls (see Figure 6.3). These experiments were conducted in the same manner as the earlier EFML experiments, with some minor variations. Here, four tilting weirs of the same design as the EFML models were examined at $\theta = 33°, 44°, 59°$, and 90°, and L was reduced to 126 mm. The crest location of each model structure was kept consistent at 11 m downstream of the flume inlet, which was a sufficiently long entrance length to ensure a fully developed velocity profile. Measurements of h were made 0.8 m upstream of the crest location using a trio of ultrasonic depth sensors measuring at 50 Hz and spaced evenly in the transverse direction across the 1 m wide channel. Measurements of steady Q were made using an electromagnetic flow meter recording at 50 Hz. The resultant time-series of h and Q were then averaged over 60 s to yield mean values, and the measurements of h were further averaged across the three sensors. The standard deviation in the measurements of h and Q were approximately 1 mm and 0.3 L/s, respectively.

6.4 Results

6.4.1 Verification with Previous Experimental Work

The present goal is to utilize the tilting weir as a special case of the sharp-crested weir ($\theta = 90°$). In the interest of best-practice we choose here to verify our experimental results for the vertical sharp-crested weir, labeled as experiments K and O in Table 6.1. In Figure 6.4, it can be seen that there is excellent agreement between the dimensionless rating equation of Kindsvater and Carter (1959), given by Eq. (6.8), and the experimental data for the sharp-crested weir observed within the current study. For the combined 47 observations shown in Figure 6.4, the MAPE between the observed C_e, and that predicted by Eq. (6.8) is only 0.55 %. Also plotted is the C_e equation given in King et al. (1929). It corresponds to: $C_e = 0.602 + 0.082(h/p)$. King et al. (1929) recommended the use of this equation with a k_h value of 1.25 mm as a very close alternative to his equation for the standard discharge coefficient (i.e., $C_d = 0.605 + 0.08h/p$). The King et al. (1929) equation has the same intercept as Eq. (6.8), but the slope does not match the current experimental data as well as that of Kindsvater and Carter (1959).

Because these experiments were completed in relatively narrow channels of width $b = 0.3$ and 1 m, we chose to use the recommended k_b value of 0.001 m from Kindsvater and Carter (1959) for a full-width ($b/B = 1$) weir in a narrow-width channel. However, we found it unnecessary to implement the introduction of k_h because for our experiments K and O, we

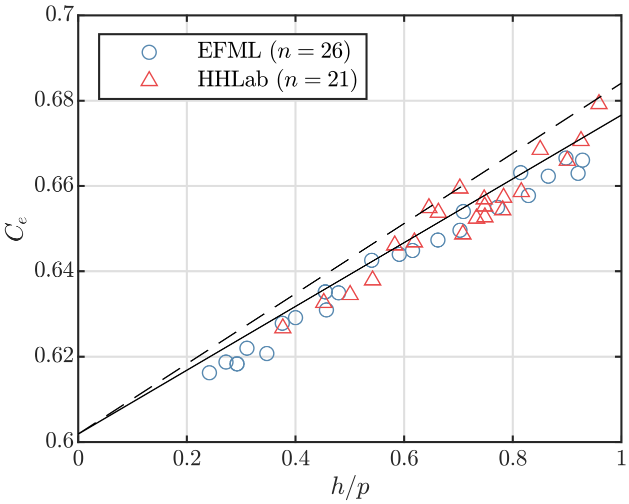

Figure 6.4: Dimensionless stage-discharge plot comparing the results of the present study for a sharp-crested weir ($\theta = 90°$) with the best-fit equations of previous experimentalists. Data points are calculated as $C_e = Q/\frac{2}{3}\sqrt{2g}b_e h_e^{3/2}$, with $k_b = -0.001$ m and $k_h = 0$ m. The solid line corresponds to $C_e = 0.602 + 0.075h/p$ from Kindsvater and Carter (1957). The dashed line corresponds to $C_e = 0.602 + 0.082h/p$ from Rehbock (1929).

did not observe the artificial increase in C_e attributable to the decrease in h that occurs when We effects are present under clinging flow conditions. Rather, Re effects appeared to be dominant for these experiments. Therefore, for all of the data presented in the current study, k_h is taken as 0 m. We aim to define a threshold h value below which viscous and surface tension effects are significant.

6.4.2 Determining the Effect of the Varying Inclination Angle

Figure 6.5 plots the data collected at the EFML for this study across all θ values and flow conditions examined, representing Q ranging from 4.1-30.5 L/s. An attempt also was made to study the flow characteristics over a model where $\theta = 20°$, but sufficient free flow conditions could not be achieved. Furthermore, as shown in Table 6.1, the maximum value of h/p for most experiments was approximately unity before the flow became inundated. This was due to the bed elevation remaining constant downstream of the weir. This $h/p = 1$ limit for free flow was earlier predicted by King et al. (1929) for channels where there is no drop in bed elevation downstream of the crest.

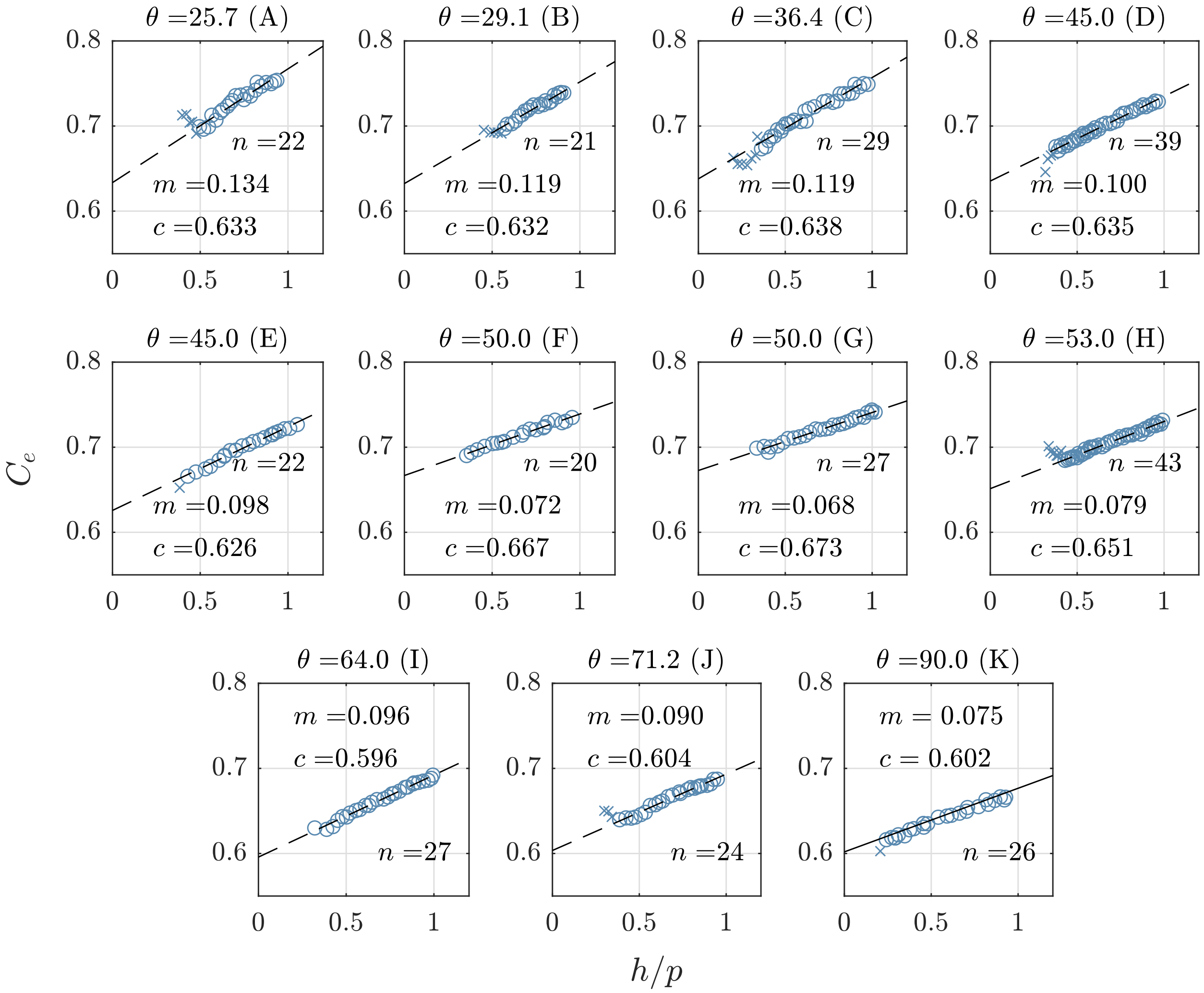

Figure 6.5: Dimensionless plot of C_e versus h/p for each weir inclination angle studied for the EFML experiments, with the linear best fit equation obtained from least-squares regression shown in the form: $C_e = c + m(h/p)$. Here, $C_e = Q/\frac{2}{3}\sqrt{2g}b_e h_e^{3/2}$, with $k_b = -0.001$ m and $k_h = 0$ m. Data points considered as free flow and used to calibrate the linear best fit equation are shown by circles and tallied by n. Data points excluded due to scale effects shown by 'x's.

HHLab data are shown in Figure 6.6, representing Q ranging from 10.7-84.1 L/s. In these plots, C_e is calculated exactly as in Eq. (6.8), with k_b = -0.001 m and k_h = 0 m. It can be seen that for the linear equation representing the dimensionless head-discharge rating equation, given by the form $C_e = c + m(h/p)$, both the intercept (c) and slope (m) of this line tend to increase as θ decreases. This can be understood by realizing that the tilting weir is an obstruction to the flow, and the amount of obstruction presented to the flow by the weir depends upon θ. Generally, the streamlines over the crest become more horizontal as θ

decreases and as h/p increases. Due to this reduction in the contraction of the overflowing jet, less upstream potential energy, represented by h, is needed for the flow to pass over the obstacle presented by the weir for a given discharge.

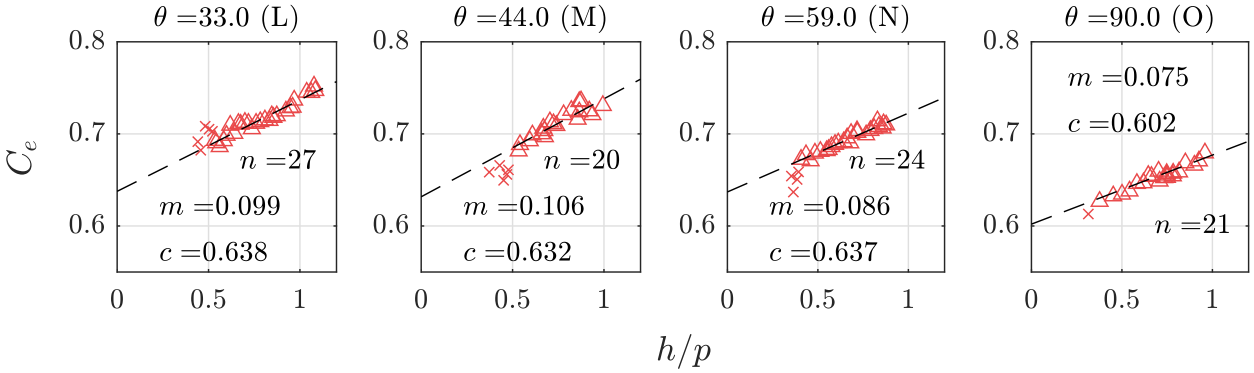

Figure 6.6: Experimental data for tilting weir flow observed at the HHLab. See Figure 6.5 for information on linear best fit lines. Here data points considered as free flow and used to calibrate the linear best fit equation are shown by triangles.

To account for this effect, we propose a transformation to the h term in a manner similar to that used by Kindsvater and Carter (1959) and originally examined by King et al. (1929). These authors suggested a linear transformation of the h term to account for the presence of viscous and surface tension effects at low values of h for flow over a sharp-crested weir. In a similar fashion, one can understand the effect of the changing θ for flow over a tilting weir as primarily affecting the h term. The magnitude of this h term, representing the amount of potential energy required to pass a certain flow over the weir crest, changes in response to shifting modes of approach kinetic energy dissipation and momentum transfer, as brought on by the changing θ.

Whereas Kindsvater and Carter (1959) used a simple linear transformation to account for viscous and surface tension effects for the static sharp-crested weir, an additional nonlinear transformation must be utilized for the case of the variably tilting weir due to the additional degree of freedom introduced by θ. Here, the flow dynamics are influenced both by the changing value of θ and the relative inertial condition, as defined by h/p. In keeping with the method of calculation of C_e used by Kindsvater and Carter (1959), we choose to retain the notation of h_e as it is defined by Eq. (6.9). However, it should be noted that for this study, h and h_e were equivalent since k_h was kept as 0 m. The purpose of our additional proposed correction factor is to transform the h_e observed over a tilting weir to the h_e that would be observed under the same discharge if the weir were completely perpendicular to the bed (i.e., $\theta = 90°$) using a term we call k_θ. An example transformation of the C_e values by k_θ is shown by Figure 6.7. When applied to the h_e term, the head-discharge rating equation for a tilting weir becomes:

$$Q = C_e \frac{2}{3} \sqrt{2g} b_e (k_\theta h_e)^{3/2} , \tag{6.12}$$

where $C_e = 0.602 + 0.075h/p$ from Eq. (6.8), and h_e and b_e are given by Eqn. (6.9) and Eq. (6.10), respectively. It should also be noted that the h/p term embedded in Eq. (6.12) within the C_e term has not been transformed by k_θ or k_h, but is in fact the directly measured ratio at any value of θ.

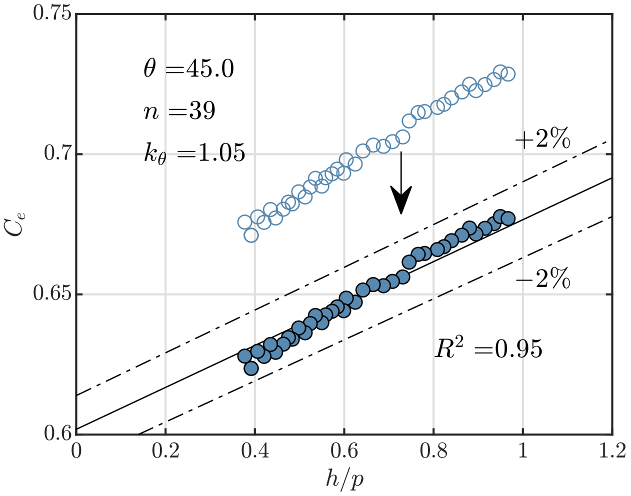

Figure 6.7: Example transformation of C_e values for constant h/p by way of k_θ head multiplication factor, from Experiment D. For the original values, shown by the hollow circles, $C_e = Q/\frac{2}{3}\sqrt{2g}b_e h_e^{3/2}$, with $k_b = -0.001$ m and $k_h = 0$ m, as in Figure 6.5. For the transformed values, shown by the filled circles, $C_e = Q/\frac{2}{3}\sqrt{2g}b_e(k_\theta h_e)^{3/2}$, with $k_\theta = 1.05$. Also shown is the R^2 value for the transformed values with respect to Eq. (6.8), given by the solid line, with ± 2% deviation shown by the dashed lines.

For determining k_θ, the most relevant length scale in this flow scenario is in the vertical because this indicates the degree to which the pressure at the crest will deviate from hydrostatic due to the vertical momentum of the flow as it navigates the weir (Castro-Orgaz and Hager, 2017). So, one can reasonably expect that k_θ could be understood most parsimoniously as being a function of $\sin\theta$, as was previously identified in our dimensional analysis. Using the independently measured discharge, unique values of k_θ can be found for each observation as:

$$k_\theta = \left[\frac{Q}{C_e \frac{2}{3}\sqrt{2g}\, b_e h_e^{3/2}}\right]^{2/3} . \tag{6.13}$$

For each experiment shown in Table 6.1, the average value of k_θ calculated by Eq. (6.13) was found and is given in Table 6.2. Then, a trial and error best-fit regression analysis was performed to fit an empirical function to the calibrated k_θ values. Gaussian, sum of sine, and power function fits were examined.

Table 6.2: Mean and standard deviation values for k_θ distributions for each experiment.

Experiment	θ (°)	$\overline{k_\theta}$	std. dev.
A	25.7	1.074	0.0081
B	29.1	1.064	0.0045
C	36.4	1.065	0.0083
D	45	1.050	0.0040
E	45	1.042	0.0040
F	50	1.064	0.0025
G	50	1.066	0.0036
H	53	1.053	0.0016
I	64	1.009	0.0047
J	71.2	1.012	0.0034
K	90	1.000	0.0022
L	33	1.055	0.0055
M	44	1.054	0.0070
N	59	1.043	0.0032
O	90	1.000	0.0038

The greatest agreement with the observed k_θ values in Table 6.2 was found using a two-term power function, given by:

$$k_\theta \simeq -\beta(\sin\theta)^\lambda + (1+\beta)\,, \tag{6.14}$$

where for the current experimental data $\beta = 0.07$ and $\lambda = 4.5$. Eq. (6.14) is valid for $\theta = 25° - 90°$, with RMSE = 0.0094 (see Figure 6.8).

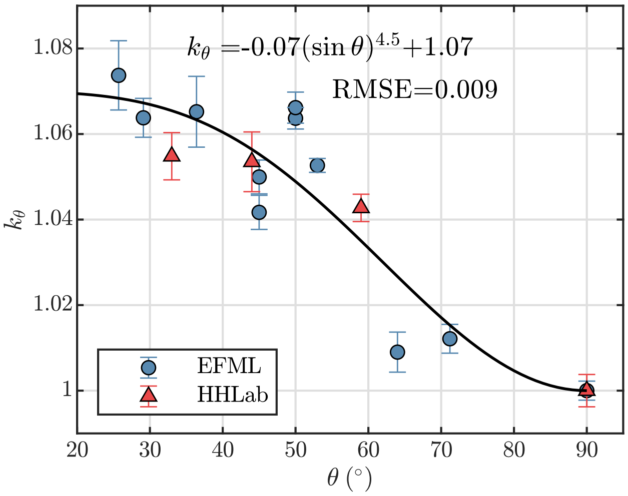

Figure 6.8: Empirical data and best-fit curve for the relationship between θ in degrees with the head correction factor k_θ. Mean values of k_θ are shown for each experiment, with error bars representing ± one std. dev., as in Table 6.2.

Eq. (6.14) is monotonic in the range of realistic θ values for tilting weirs. The implicit assumption in this approach is that the effect of the inclination on the contraction coefficient of the nappe is continuous, and that there is no intermediate value of θ between 0-90° which represents either a local maxima or minima in the discharge capacity for the tilting weir. This is an assumption supported by the hypothesis of (Rouse, 1932) that the effect of increasing θ on the contraction coefficient would be akin to a decrease in h/p. As can be seen from Eq. (6.8) and Figure 6.4, the influence of h/p on the discharge capacity of the weir also is monotonic.

The inclusion of the exponent λ on the $\sin\theta$ term indicates that the effect of θ on the contraction of the streamlines around the crest is nonlinear. This is likely due to the separation zone that is present at higher values of θ, but eventually disappears below some threshold value. From a cursory analysis of Figure 6.8, a first approximation of this threshold value can be given as $\theta \approx 60°$. Zerihun (2022) also identified a similar threshold value of θ for the influence of the separation zone on the flow dynamics. From the construction of Eq. (6.14), it is evident that when $\theta = 90°$, k_θ will be unity in Eq. (6.14), and Eq. (6.12) reduces to the classical sharp-crested weir rating equation given by Kindsvater and Carter (1959). At a minimum value of $\theta = 20°$, a maximum k_θ value of approximately 1.07 is applied to the head term. Physically, this means that the same discharge is passing over the structure inclined at $\theta = 20°$ with a 6.5% reduction in h compared to that discharge passing over a sharp-crested weir inclined at $\theta = 90°$.

6.4.3 Analyzing Uncertainty and Considering Operational Constraints

In addition to the 392 free-flow depth-discharge observations shown in Table 6.1, 48 additional observations across θ values were made, but were excluded from the calibration of Eq. (6.14) since these observations were made outside the normal operating regime of the tilting weir. This concerned flows at low values of h that were subject to scale effects due to viscosity and surface tension. Flows outside the normal operating regime were identified either visually by the presence of a clinging nappe, or by regression analysis. If the inclusion of a certain data point at a low value of h noticeably reduced the regression coefficient of the linear C_e vs. h/p equation shown in Figure 6.5 and Figure 6.6, it was excluded. These additional observations are included in Figure 6.9 and Figure 6.10 to show the influence of scale effects on the accuracy of the rating equation to predict discharge.

Figure 6.9 shows a plot of C_e versus h/p computed from Eq. (6.12) for the 440 observed sets of Q, h, h/p and θ, in comparison to Eq. (6.8). In Figure 6.10, $\%_{error}$ is defined as the

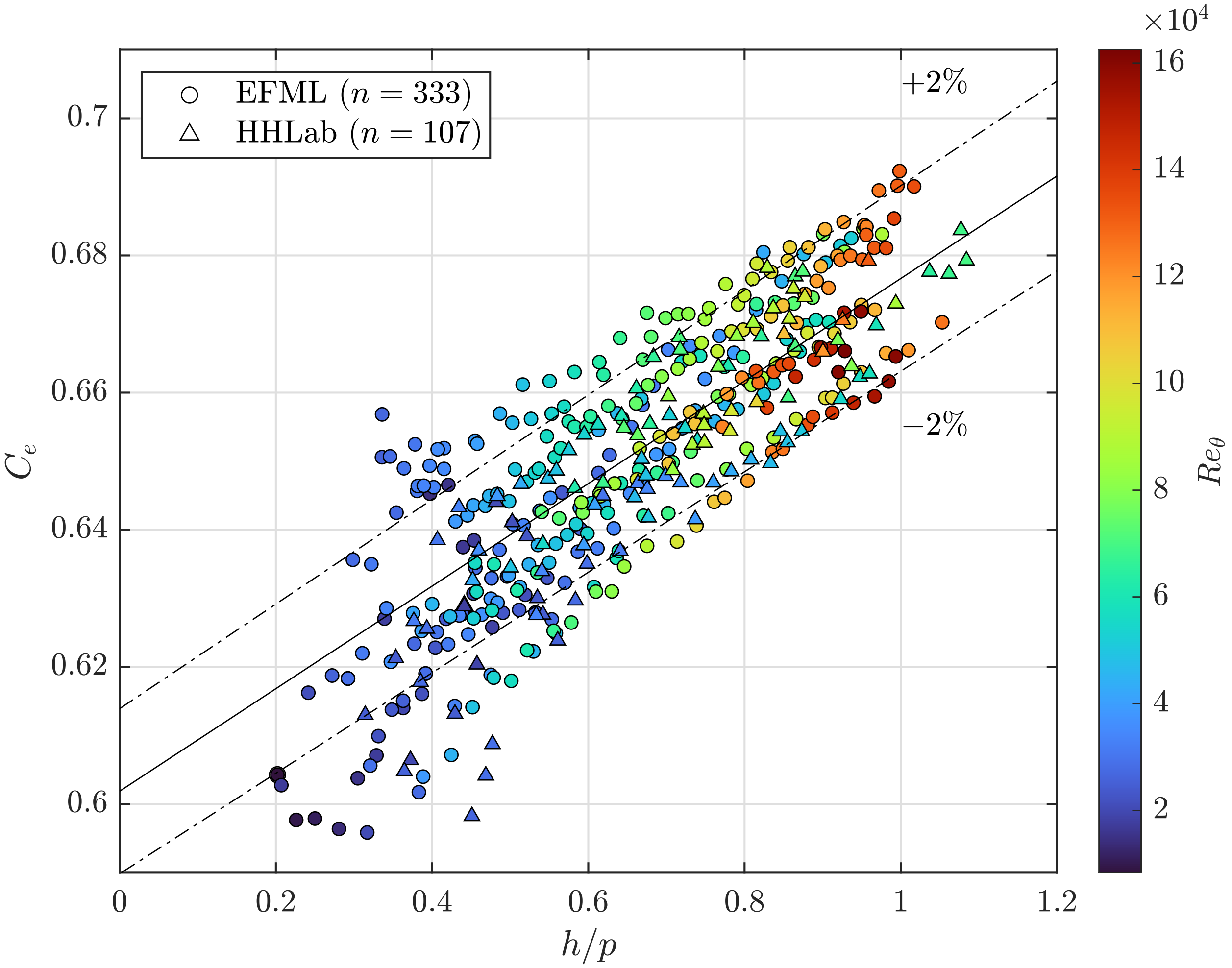

Figure 6.9: Scatter plot of C_e versus h/p for total of 440 observations after tilting weir h values have been corrected by the k_θ values given by Eq. (6.14). The solid line with ± 2 % deviation is Eq. (6.8) and represents the predicted flow by Eq. (6.12). The Re_θ (defined by Eq. (6.16)) color bar is shown to indicate how the deviation from the predicted C_e to the observed grows as Re_θ decreases.

relative percent difference between the observed discharge during experimentation (Q_{obs}) and the predicted discharge (Q_{pred}) given by:

$$\%_{error} = \frac{Q_{obs} - Q_{pred}}{Q_{obs}} \times 100 \,. \tag{6.15}$$

It can be seen from Figure 6.9 that there is a general relationship between h/p and $\%_{error}$, with $h/p = 0.6$ being an approximate divergence point below which $\%_{error}$ beings to grow. This value was previously identified by a separate study as an indicator of the lower threshold for the normal operating regime of a sharp-crested weir (Sinclair et al., 2022). For all observations of the current study, when $h/p \leq 0.6$, the mean of $|\%_{error}|$ is 1.75%. When $h/p > 0.6$, this value is reduced to 1.15%.

To explore thresholds related to Re and We scale effects, we also define updated Re and We numbers, where the length scale has been corrected by k_θ:

$$Re_\theta = \frac{\sqrt{g}(k_\theta h)^{3/2}}{\nu} , \tag{6.16}$$

$$We_\theta = \frac{\rho g (k_\theta h)^2}{\sigma} . \tag{6.17}$$

Figure 6.10 and Table 6.3 reveal the relationship between Re_θ, We_θ, and the relative percent error ($\%_{error}$) between the predicted and observed discharge for the 440 observations within the current study. Two flow regimes were identified. The threshold values of Re_θ and We_θ were identified by determining when the MAPE for the lower regime grew beyond 2%, and the prediction bias, represented by the mean value of $\%_{error}$, was as close to zero as possible for the upper regime. We choose ±2% as a somewhat arbitrary threshold, but this level of accuracy can generally be considered as excellent for flow measurements over hydraulic structures (Replogle, 2002).

Table 6.3: Relationship between head-discharge equation prediction accuracy and inertial regimes as defined by Re_θ and We_θ. For use as a best practice guide for the normal operating regimes of tilting weirs.

Regime	Re_θ	We_θ	$\approx h$ (cm)	n	prob. ±2%	$\overline{\%_{error}}$	$\overline{\|\%_{error}\|}$
I	$\leq 3 \times 10^4$	$\leq 3 \times 10^2$	$h \leq 5$	72	0.53	-1.45	2.08
II	$> 3 \times 10^4$	$> 3 \times 10^2$	$h > 5$	368	0.80	-0.08	1.25

Regime I occurs when $Re_\theta \leq 3{\times}10^4$ & $We_\theta \leq 3{\times}10^2$ and represent flows that occur below the absolute minimum required inertial state in the approach for the weir to be considered operating in free flow. Below this threshold, scale effects cannot be justifiably neglected.

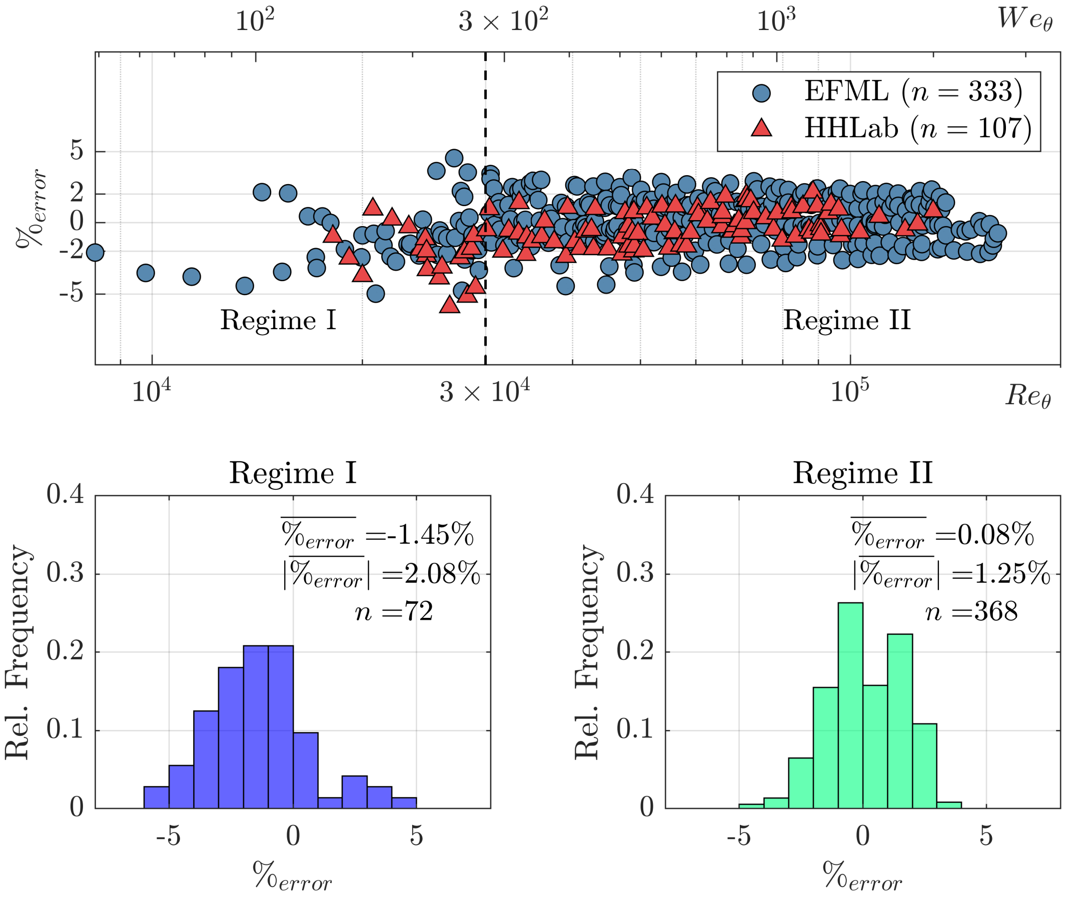

Figure 6.10: Top: scatter plot of 440 flow observations showing the relationship between prediction accuracy and Re_θ & We_θ. Bottom: frequency histograms of distribution of $\%_{error}$ for the two flow regimes identified.

Figure 6.10 and Table 6.3 show that for the majority of points, this results in the observed discharge being smaller than what is predicted for this regime, indicating that Re_θ effects were more significant here than those due to We_θ. This can be most readily explained by understanding that as viscous effects become more significant at low values of Re_θ, the piezometric head (h) must grow larger to account for the decrease in the velocity head. Regime II occurs when $Re_\theta > 3 \times 10^4$ & $We_\theta > 3 \times 10^2$. Here, scale effects are minimized and the accuracy of the head-discharge equation is optimized. This represents the ideal operating regime for a tilting weir. Table 6.3 shows that for this regime, the average $\%_{error}$

is only -0.08%, indicating the bias in the predicted discharge has been removed compared to Regime I.

These threshold values for Re_θ and We_θ can also be translated to more practical values of h, if we assume common values for physical constants and the fluid properties of room-temperature water (i.e., $g = 9.81\,m/s^2$; $\mu = 10^{-3}\,Ns/m^2$; $\rho = 1000\,kg/m^3$; $\sigma = 0.0728 N/m$). These approximated values are shown in Table 6.3. Unsurprisingly, we find a similar result as Kindsvater and Carter (1959) for the threshold value of $h \approx 0.05$ m as the point above which scale effects can be justifiably neglected. A similar finding was also reported in Hager (1994), but Ranga Raju and Asawa (1977) advocate for a higher threshold for avoiding scale effects of $h > 0.11$ m. The frequency histograms shown in Figure 6.10 also can be used to estimate the probability of a certain level of measurement accuracy within each regime (see Table 6.3).

6.5 Discussion

We now turn to some qualifications for the findings of the current study. First, it can be observed from the residuals in Figure 6.8 that the greatest uncertainty in the value of k_θ occurs between $\theta = 45°$ and $65°$. We hypothesize that this is partially due to experimental error and uncertainty in the aeration condition of the downstream nappe. Another possible explanation is the instability of the separation zone in this region. Additionally, in Figure 6.8, it can be seen that a large gap in the observed k_θ values exists between the four experiments with $\theta > 60°$ and the remainder of the experiments. One possible explanation for this behavior could be the disappearance of the separation zone below $\theta \approx 60°$, which merits further exploration.

An analysis of Figure 6.7 reveals that k_θ may be dependent on h/p as well as $\sin\theta$. This dependence is observable for experiment D in Figure 6.7; but a consistent dependence was not found between all experiments upon further investigation. Additional experimentation to investigate the link between k_θ with both h/p and $\sin\theta$ is warranted.

Finally, additional observations are needed for θ between 60° and 90°. The experimental data of the current study is sparse in this range, where the dynamics of the separation zone are likely to change most significantly. It also remains to be seen how applicable these laboratory findings can be when the flow problem is scaled up and implemented in the field. Additional complexities related to the amount of friction in the approach channel, the approach geometry, the impact of sedimentation over time, and changes to the surface roughness of the weir plate must be considered.

6.6 Conclusions

Observations of head and steady discharge were made for 440 flow cases in two unique experimental facilities, over hydraulic models of tilting weirs with inclination angles ranging from $\theta = 25^\circ$ to 90°. This allowed for the calibration of a head multiplication term as a function of the inclination angle, given by k_θ in Eq. (6.14). This empirical equation accounts for the fact that at a constant discharge, the head upstream of a tilting weir generally decreases with the inclination angle, due to the improved navigability of the streamlines over the crest and reduction in non-hydrostatic effects near the crest. The factor k_θ then acts to adjust the observed head over a tilting weir to that expected if the weir was perpendicular to the channel bed. Then, a modified form of the classical sharp-crested weir rating equation, given by Eq. (6.12), can be applied to predict steady discharge. If the inertial state of the approach flow is kept above a threshold value of at least $Re_\theta = 3 \times 10^4$ & $We_\theta = 3 \times 10^2$ ($h \approx 0.05$ m) and the nappe remains fully aerated, the tilting weir can be considered within an ideal operating regime where the mean absolute value of the error in the predicted discharge is only 1.3% for the current experimental data (see Table 6.3). We also identify a h/p value of 0.6 as a more immediately applicable threshold for the normal operating regime, but note that this value will likely not hold for especially small weirs (i.e., $L < 0.1$ m).

The results of this study work to synthesize and expand significantly upon the current level of knowledge within the literature. The most extensive experimental study to date on developing a head-discharge rating equation for tilting weirs is that of Wahlin and Replogle (1994). The current study expands on this work by developing an equation having greater continuity with previous work, in that it links back to the classical empirical data for the sharp-crested weir, being applicable for $25° \leq \theta \leq 90°$. We also offer a more parsimonious monotonic solution to correct for the effect of the dynamic weir inclination angle that relies less on arbitrarily maximizing goodness-of-fit metrics for the observed empirical data, and instead aims to give insight to the underlying flow dynamics. In terms of calibration accuracy, the current study contains a much larger number of observations of the flow at θ between 45° and 90° than in previous studies. As shown by Figure 6.11, this results in the data from the current study agreeing well with the findings of previous researchers for certain values of θ, while also being able to more fully reveal the nature of the relationship between Q_θ/Q_{90} and θ across a wide range of operational θ values. In summary, the findings of this study promote the tilting weir as a practical and versatile structure not only for stage regulation but also for flow measurement, giving operators of open-channel flows the opportunity for much greater control and efficiency within their system.

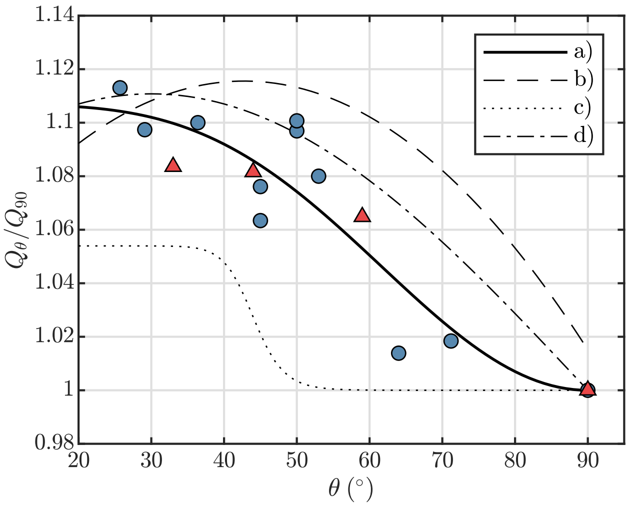

Figure 6.11: Comparison of current and previous study results on the relative effect of the changing θ on Q for a given value of h. a) Eq. (6.14) of the current study, taken to the 3/2 power. Blue circles are EFML data, and red triangles are HHLab data, b) Wahlin and Replogle (1994), c) Bijankhan and Ferro (2018), and d) Hager (1994).

6.7 Towards Practical Implementation

Step-by-step instructions taken from the approach laid out in this study for using the tilting weir as a water flow measurement structure are as follows:

1. Measure the inclination angle (θ) of the weir from the horizontal and the crest elevation (p) relative to the upstream channel bed.
2. Measure the depth of water flowing over the weir crest (h) at a distance of 3-4 times the anticipated h, upstream from the crest location. For most accuracy, ensure $h > 0.05$ m.
3. Calculate h/p. For channels without a downstream drop in bed elevation below the crest, h/p should remain below 1.
4. Using h/p, calculate C_e from Eq. (6.8).
5. Calculate h_e and b_e using the recommended values of k_h and k_b of Kindsvater and Carter (1959), as shown by Eqs. 6.9 and 6.10, respectively.
6. Calculate k_θ using Eq. (6.14). For most accuracy, ensure $25° \leq \theta \leq 90°$.
7. Using Eq. (6.12), estimate the discharge Q.

Chapter 7

Dynamics of Flow Over Tilting Weirs [3]

7.1 Introduction

As shown in Chapter 5, there is much information to be garnered concerning the discharge characteristics of weir flows by examining the underlying flow dynamics to elucidate the interplay between velocity and pressure, the importance of flow separation, and turbulent mixing. To build upon the seminal works on this topic completed a century ago (Bazin, 1898; Schoder and Turner, 1929), advances in state-of-the-art experimental and numerical investigative tools allow for a deeper understanding of the dynamics governing weir flows beyond the limited information that is given by a singular bulk parameter such as C_d or h/p. Ultimately, the goal of these types of analyses is to inform the improved design and operation of these structures in order to better fulfill their intended purpose. As will be seen in this chapter, the tilting weir offers the ability to dynamically control the structure inclination angle to alter the hydraulic characteristics of the flow field in the approach channel. This allows the tilting weir operator some measure of control over important aspects of a system, such as the water surface fluctuations for accurate head measurement, bed shear stress contributing to sediment transport, and flow depth to provide pressure head for lateral outflows. The mindful engineer will be aware of how to use the tilting weir in such a way that their desired practical aims are met within the operational constraints established by the implicit tradeoffs present in the flow field dynamics - which will be further explained in this chapter.

In Chapter 5 it was shown that C_d can be re-cast as a weir Froude number, Fr_h, and be further decomposed into its constituent parts which inform the physical mechanisms

---

[3] The research presented in this chapter is currently under preparation for submission to the *Journal of Hydraulic Engineering* under the title "Dynamics of Tilting Weir Flows".

influencing the discharge characteristics. It is the goal of the present chapter to leverage the same type of analysis to tilting weir flows to explain how and why the discharge characteristics of the tilting weir change with varying θ and h/p. To do so, we introduce here a few common quantitative flow field descriptors, as well as some original terms defined here for the special case of tilting weir flows.

7.1.1 The Tilting Weir Froude Number as a Discharge Coefficient

As described in Chapter 5, the dimensionless discharge for weir flows can be defined as a type of Froude number. We give a more general definition here for tilting weirs, which incorporates θ:

$$Fr_{h\theta} = \frac{q}{\sqrt{g}(hk_\theta)^{3/2}} \,. \tag{7.1}$$

The left-hand side of Eq. (7.1), as shown in Chapter 5, can be decomposed as the product of an integration constant, the angle correction factor (k_θ) introduced in Chapter 6, and a series of three coefficients:

$$Fr_{h\theta} = (2\sqrt{2}/3)(k_\theta^{-3/2})C_v K C_c \,, \tag{7.2}$$

where:

$$C_v = \left(\frac{q}{t}\right) \Bigg/ \left(\frac{1}{h}\frac{2}{3}\sqrt{2g}\left[\left(h + \frac{{U_0}^2}{2g}\right)^{3/2} - \left(\frac{{U_0}^2}{2g}\right)^{3/2}\right]\right) \,, \tag{7.3}$$

$$K = \frac{1}{h^{3/2}}\left[\left(h + \frac{{U_0}^2}{2g}\right)^{3/2} - \left(\frac{{U_0}^2}{2g}\right)^{3/2}\right] \,, \tag{7.4}$$

$$C_c = \frac{t}{h} = \frac{h - \delta - \epsilon}{h} = 1 - \frac{\delta}{h} - \frac{\epsilon}{h} \,. \tag{7.5}$$

Here, C_v, K, and C_c are respectively the velocity coefficient, head correction factor, and contraction coefficient. k_θ is the angle correction factor to account for the effect of θ on the tilting weir discharge characteristics. All other variables are the same as previously defined in Chapter 5.

7.1.2 Boundary Layer Displacement Thickness, Distribution of Kinetic Energy and Momentum

Important parameters for describing the velocity profiles of open-channel flows are the boundary layer displacement thickness (δ^*), and the respective kinetic energy (α) and momentum (β) correction factors. δ^* is defined as:

$$\delta^* = \int_0^D (1 - u(z)/U_e) dz \, , \tag{7.6}$$

where U_e is the maximum velocity in the vertical profile, typically taken to be the free-surface velocity in fully developed channel flows uninhibited by surface shear. For two-dimensional rectangular channel flows with negligible vertical velocity, α and β are defined as:

$$\alpha = \frac{b \int_0^D [u(z)]^3 dz}{bq^3/D^2} \, , \tag{7.7}$$

$$\beta = \frac{b \int_0^D [u(z)]^2 dz}{bq^2/D} \, . \tag{7.8}$$

7.1.3 Shear Velocity, Friction Slope, and Reynolds Stresses

Resistance to flow in open channels is commonly described using an estimation of the bed shear stress, τ_b (Mishra and Venayagamoorthy, 2024a). This is the tangential force per unit area that balances the down-slope component of the gravitational force caused by the weight of the fluid. Due to Newton's third law, it also represents the shearing action of the fluid on the channel boundary, and therefore is an important parameter in estimations of sediment transport. For a fully developed flow of a Newtonian fluid, the boundary shear stress is defined by the velocity gradient near the boundary (i.e., $\tau_b = \mu(du/dz|_{z=0})$). The shear (or friction) velocity is a representation of τ_b in dimensions of velocity [LT^{-1}], used as a scaling factor for wall bounded turbulent flows.

$$u_* = \sqrt{\frac{\tau_b}{\rho}} = \sqrt{\nu \left(\frac{du}{dz}\right)\bigg|_{z=0}} . \tag{7.9}$$

Due to the difficulty of making accurate and non-intrusive measurements of the near-wall velocity gradient ($du/dz|_{z=0}$), practical methods to estimate u_* are abundant. For steady, gradually-varied flow where the pressure gradient is hydrostatic, u_* can be estimated as:

$$u_* \equiv \sqrt{gRS_f} , \tag{7.10}$$

where S_f is the friction slope, defined by the gradient of decreasing total hydraulic head ($-dH/dx$) in the longitudinal direction (see Eq. (3.1)). A greater friction slope indicates increased energy losses along the channel reach due to distributed boundary friction. Mechanisms for energy dissipation are described by the turbulent kinetic energy cascade (see Section 2.4), whereby energy contained by the largest flow structures (i.e., eddies) of the mean flow field is transferred to smaller and smaller scales by turbulent fluctuations, until the energy is dissipated as internal heat by the action of viscous diffusion. The Reynolds stress terms in the RANS equations (see Section 2.3) can be used to conceptualize the stress the mean flow field experiences as a result of momentum transfer by fluctuating turbulent motions. For two-dimensional open-channel flow, the most important component of the Reynolds stress tensor is $-\rho\langle u'w' \rangle$, representing the vertical turbulent transport of streamwise momentum by near-wall motions such as bursts and sweeps (Kim et al., 1971).

7.1.4 Vertical Advection and Pressure Gradient

A common simplifying assumption in two-dimensional open-channel flow is that of horizontal streamlines resulting in a hydrostatic pressure gradient (i.e., $dP/dz = -\gamma$), and therefore it is important to understand where this condition does not hold true, such as for cases of rapidly-varied flow where a significant component of the flow inertia is in the vertical direction. For flows over tilting weirs, as shown in Chapter 5, the magnitude of the pressure gradient in the vertical helps inform the contraction dynamics of the nappe. The vertical pressure gradient for weir flows can be defined from examining the steady Navier-Stokes Eq. (2.9) equation in the vertical direction under the assumption of two-dimensional flow (i.e., $i = 3$, $j = 1, 3$):

$$u\frac{\partial w}{\partial x} + w\frac{\partial w}{\partial z} = -\frac{1}{\rho}\frac{\partial P}{\partial z} - g + \nu\left[\frac{\partial^2 w}{\partial x^2} + \frac{\partial^2 w}{\partial z^2}\right] . \tag{7.11}$$

If it is further assumed that the contribution of viscous effects is small (often a fair assumption for the convergent nature of flow observed for tilting weirs), Eq. (7.11) can be reduced to the inviscid Euler equation and re-arranged to define a dimensionless pressure gradient:

$$-\frac{1}{\gamma}\frac{\partial P}{\partial z} \approx \frac{1}{g}\left[u\frac{\partial w}{\partial x} + w\frac{\partial w}{\partial z}\right] + 1 . \tag{7.12}$$

where it can be readily observed that an absence of vertical inertia ($w \approx 0$) will result in a hydrostatic pressure gradient, and that when the vertical advection terms are in balance with gravity, the pressure gradient will be zero, as will eventually be the case for the free-falling jet that occurs within the undisturbed nappe downstream of the weir crest.

7.1.5 Head Loss via Turbulent Kinetic Energy Dissipation

The decomposition of $Fr_{h\theta}$ features the velocity coefficient, C_v to account for viscous energy losses. It is therefore prudent to consider the mechanisms by which energy is dissipated between the gauging section and critical section as the flow traverses the obstacle of the weir. This can be done be examining the turbulent kinetic energy (TKE) dissipation field. The TKE dissipation rate, ε, previously defined by Eq. (2.20), represents the rate by which turbulent kinetic energy from the mean field is transferred down through a cascade of smaller and smaller spatial and time scales until it is dissipated as internal heat by the action of viscosity. For comparing across different flow cases, we will non-dimensionalize ε

using scaling terms from the bulk flow:

$$\varepsilon^* = \frac{2\nu\langle s'_{ij}s'_{ij}\rangle}{U_0^3/h} \,. \tag{7.13}$$

where $U_0 = q/D$ is the bulk velocity at the upstream gauging section, and h is the head over the weir.

The following analysis examines how the above parameters of the flow field dynamics for the tilting weir change with θ and h/p, as described by the tilting weir Froude number, $Fr_{h\theta}$.

7.2 Methodology

7.2.1 Experimental Measurements

As in Chapter 6, experimental data for tilting weir flow dynamics was gathered in two separate experimental facilities: the Environmental Fluid Mechanics Laboratory at Colorado State University (EFML), and the Hydraulics and Hydromorphology Laboratory at INRAE-Villeurbanne, France (HHLab). Particle Image Velocimetry was utilized to capture the instantaneous flow field in the vicinity of the weir and then averaged over a minimum of 1550 fields to produce a mean-field representing the steady flow over the weir. From this mean field, the turbulent fluctuating velocity field was also determined via Reynolds decomposition. Here we examine eight different flow cases where the steady volumetric discharge, Q, was kept nominally constant as $\sim$ 30 L/s/m, with θ ranging from 25.7-90°. In these experiments, Q was measured independently using an electromagnetic flow meter installed in the inlet pipe to the flume, and the flow depth at the gauging section upstream of the tilting weir was measured using a point gauge location 1 m upstream of the weir crest.

These data are supplemented by instantaneous velocity measurements made using an ADV at the HHLab for flow conditions where Q = 15, 30, 45, 60 , and 75 L/s/m, over four different tilting weir models with θ = 33, 44, 59, and 90°. Here the weir crest was located at 11 m downstream of the flume inlet, with ADV velocity profiles being measured at 100

Hz over four minutes at 1 m upstream of the weir crest and at 10 different points in the vertical column. Three control experiments were also run at discharges of $Q = 41$, 71, and 107 L/s/m, where the weir models were removed, and the velocity profiles measured for the unobstructed flow cases. Water surface elevations were also measured at 1 m increments along the flume development length, from 2 m to 10 m downstream of the inlet, to estimate S_f. These measurements were made using ultrasonic water depths sensors measuring at 50 Hz. Independent measurements of discharge were made at 1 Hz using an electromagnetic flow meter installed in the inlet pipe to the flume.

7.2.2 Numerical Simulations

Finally, computational fluid dynamics (CFD) simulations, similar to those described in Chapter 5, were completed using FLOW-3D. All simulations utilized the k–ω RANS turbulence model. The width of the numerical domain was 0.15 m, with a no-slip channel boundary wall as one boundary condition in the transverse direction, and a symmetry boundary condition in the other. The symmetry boundary condition allowed for the aspect ratio of the numerical channel to be doubled because the side-wall boundary layer effect was present only on one of the boundaries. The length of the numerical domain in the approach to the crest was 1.5 m, with the upstream boundary condition in the longitudinal direction being set to ensure a constant volumetric influx of 10 L/s. This flow condition was examined over tilting weir models with θ ranging from 3-90°, as well as for the case of the free overfall ($\theta = 0°$). The length of the weir blade, L, was constant in all models at 10 cm.

Details for all experimental and numerical flow cases examined are provided in Table 7.1. Nappe characteristics (i.e., C_v, C_c) for the HHLab-ADV data were unavailable due to experimental limitations.

Table 7.1: Details for experimental and computational flow cases of tilting weirs analyzed in the current study.

Dataset	θ (°)	h (mm)	p (mm)	q (L/s/m)	h/p	Fr_h	C_v	K	C_c	ϵ/h	δ/h
EFML-PIV	25.7	60.9	65	31.95	0.94	0.68	0.98	1.07	0.69	0.03	0.28
	29.1	62.3	73	33.72	0.85	0.69	0.98	1.07	0.70	0.06	0.23
	36.4	64.0	89	33.71	0.72	0.67	0.98	1.05	0.68	0.05	0.26
	45	64.1	106	33.81	0.60	0.67	0.98	1.04	0.69	0.06	0.25
	53	64.4	125	33.30	0.52	0.65	1.00	1.03	0.67	0.08	0.25
	64	61.2	140	28.50	0.44	0.60	0.95	1.02	0.65	0.16	0.19
	71.2	61.5	147	30.92	0.42	0.65	0.97	1.03	0.69	0.08	0.23
	90	66.7	155	28.79	0.43	0.53	0.97	1.02	0.57	0.15	0.28
EFML-CFD	3	75.6	5	64.43	14.44	0.99	0.99	1.43	0.74	0.04	0.22
	6	76.6	10	63.36	7.33	0.95	0.98	1.36	0.76	0.05	0.20
	9	79.3	16	65.59	5.07	0.94	0.96	1.32	0.78	0.03	0.19
	15	82.9	26	65.55	3.20	0.88	0.97	1.25	0.77	0.03	0.20
	30	88.5	50	64.25	1.77	0.78	0.97	1.15	0.75	0.05	0.21
	45	91.6	71	62.69	1.29	0.72	0.96	1.10	0.72	0.06	0.22
	60	94.3	87	61.98	1.09	0.68	0.96	1.08	0.70	0.08	0.22
	65	95.1	91	61.83	1.05	0.67	0.96	1.08	0.69	0.08	0.23
	72	95.9	95	61.54	1.01	0.66	0.95	1.07	0.69	0.09	0.22
	90	97.9	100	61.58	0.98	0.64	0.95	1.07	0.67	0.10	0.22
HHLab-ADV	33	37.3	69	14.64	0.54	0.65		1.04			
	33	57.6	69	29.63	0.84	0.68		1.06			
	33	74.7	69	44.58	1.09	0.70		1.08			
	33	90.1	69	59.55	1.31	0.70		1.10			
	33	104.9	69	74.72	1.53	0.70		1.11			
	44	39.6	88	15.06	0.45	0.61		1.02			
	44	59.1	88	29.68	0.68	0.66		1.05			
	44	75.7	88	44.52	0.87	0.68		1.06			
	44	91.9	88	59.91	1.05	0.69		1.08			
	44	106.7	88	74.92	1.22	0.69		1.09			
	59	39.3	108	14.80	0.36	0.61		1.02			
	59	60.4	108	29.92	0.56	0.64		1.04			
	59	77.6	108	44.80	0.72	0.66		1.05			
	59	92.2	108	59.77	0.85	0.68		1.06			
	59	107.0	108	74.63	0.99	0.68		1.07			
	90	40.7	126	14.66	0.32	0.57		1.01			
	90	63.3	126	29.54	0.50	0.59		1.03			
	90	81.5	126	44.70	0.65	0.61		1.04			
	90	98.4	126	59.63	0.78	0.62		1.05			
	90	113.6	126	75.33	0.90	0.63		1.06			

7.3 Results

7.3.1 Primary and Secondary Influences on Discharge Characteristics

Figure 7.1 plots the progression of $Fr_{h\theta}$ with h/p, along with the constituent terms of $Fr_{h\theta}$. The first point to notice here is the practical functionality of the tilting weir discharge equation laid out in Chapter 6, whereby the combined effects of θ and h/p on the flow inertia are contained within $Fr_{h\theta}$, with h being corrected for θ using Eq. (6.14). Here we see that the numerical data for the EFML-CFD data set show good agreement with the experimental data and proposed approach of Chapter 6, lending credibility to its robustness. Furthermore, we see that the tilting weir discharge equation is accurate for a θ value as low as 15° ($h/p \approx 3$). Beyond this, the tilting weir flow appears to transition to a sill-type flow regime, where the weir flow equation is no longer accurate and practical complications for accurate flow measurement become present due to a considerable slope in the water surface of the approach channel. This delineation between the weir and sill regime is marked by a break in the monotonic increase in the contraction coefficient, C_c, similar to what was observed in Chapter 5 for the vertical sharp-crested weir. Evidence is also present for the influence of viscous and surface tension scale effects at low values of h/p, as can be observed from examining the data point from the EFML-PIV experiments where $\theta = 90°$.

Interestingly, the trends in K and C_c appear to match well with the earlier observed data for the sharp-crested weir, regardless of the value of θ. This gives the indication that simply scaling the tilting weir inertia using the h/p term seems to function fairly well across a large range of θ. Where this scaling breaks down, necessitating the introduction of k_θ, appears to be in the behavior of C_v. Figure 7.1 shows that these values tend to be slightly higher compared to the vertical case at the same h/p value. Although these are preliminary data and more investigation is warranted, this trend seems to suggest that the most prominent

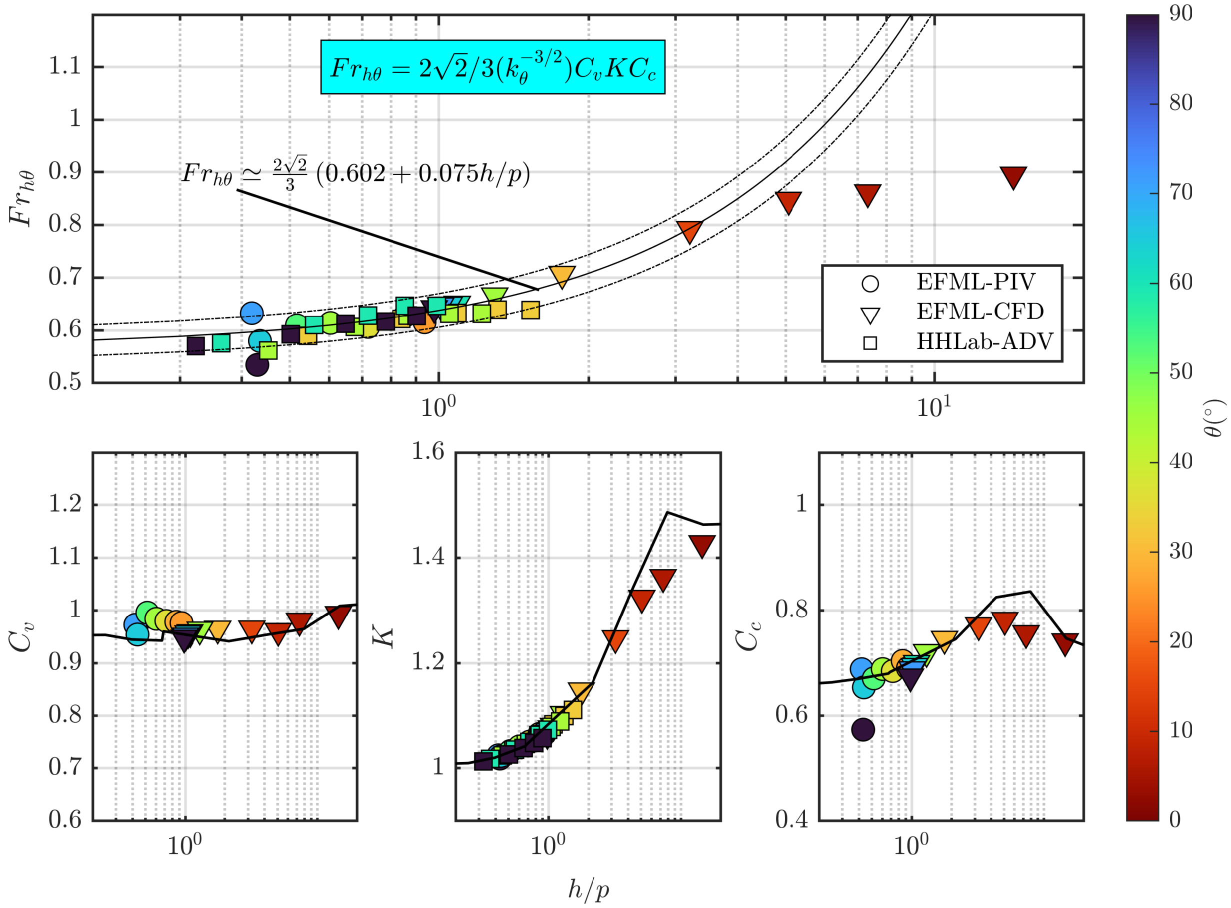

Figure 7.1: $Fr_{h\theta}$ vs. h/p for tilting weir flows spanning the weir-sill range, summarized in Table 7.1. The classical empirical equation relating h/p and $Fr_{h\theta}$, after Chapter 6, is shown in the solid line, with ±5% deviation represented by the dash-dot line. Data points are color-coded based upon their value of θ. Shown below are the constituent terms for $Fr_{h\theta}$, with respect to h/p. The solid black line in the three bottom plots indicates the trend line for the vertical sharp-crested weir data presented in Chapter 5.

reason for an increase in discharge capacity when lowering θ is due to improved navigability of the streamlines around the obstacle, resulting in less localized energy losses.

However, we see that the major contributor to the magnitude of Fr_{h_θ} is K which accounts for the contribution of kinetic energy effects on the discharge characteristics. The linear trend with both C_c and K with h/p for the flows within the weir regime is what allows for such a simple empirical equation as Eq. (6.8) to be used. For the cases of very low θ ($< 15^\circ$) shown by the EFML-CFD simulations, a break in the expected trend for weir flows in K and C_c with h/p is observed. This is indicative that the tilting weir under these flow conditions is no longer functioning as a weir, but more as a sill, and should not be utilized for flow measurement.

7.3.2 Boundary Layer Development and Distribution of Reynolds' Stresses

Turning to an examination of the velocity distribution for different tilting weir flow cases given by the HHLab-ADV data, we see in Figure 7.2 that as h/p increases and θ decreases, resulting in an increase in Fr, the velocity profile more closely follows the classical logarithmic distribution. This more fully developed and uniform distribution of momentum and kinetic energy is achieved through increasing Reynolds stresses, as shown in Figure 7.3. Figure 7.4 plots the depth averaged quantities for δ^*, S_f, α, and β, respectively. The observed monotonic increase in kinetic energy greatly influences how $Fr_{h\theta}$ increases monotonically with h/p, as observed by the behavior of K in Figure 7.1. At low values of Fr, the velocity profile follows a more parabolic profile typical of laminar flow, and the absence of Reynolds stresses indicates there is no mechanism present to mix momentum. This causes the dimensionless boundary layer displacement thickness (δ^*/D) to increase, along with α and β. The overall trends in α and δ^*/D are interesting to note, due to the fact that in classical treatments of the "infinitely high weir" (i.e., Wall Overflow case, $Fr \ll 1$) the size of the viscous boundary layer compared to the overall flow field was assumed to be negligible, and α was assumed to be 1. However, these data appear to show the opposite trend: as flow inertia increases with Fr, the thickness of the boundary layer diminishes due to more efficient mixing of momentum - which in turn means that α and β more closely approximate 1.

However, it should be noted that a decrease in the relative thickness of the viscous boundary layer compared to the overall flow depth does not necessarily result in smaller distributed energy losses for the flow moving along the channel reach. The reason why the velocity distribution is more uniform as Fr increases is also why the friction slope S_f increases with Fr: more efficient turbulent mixing of momentum and energy due to Reynolds stresses

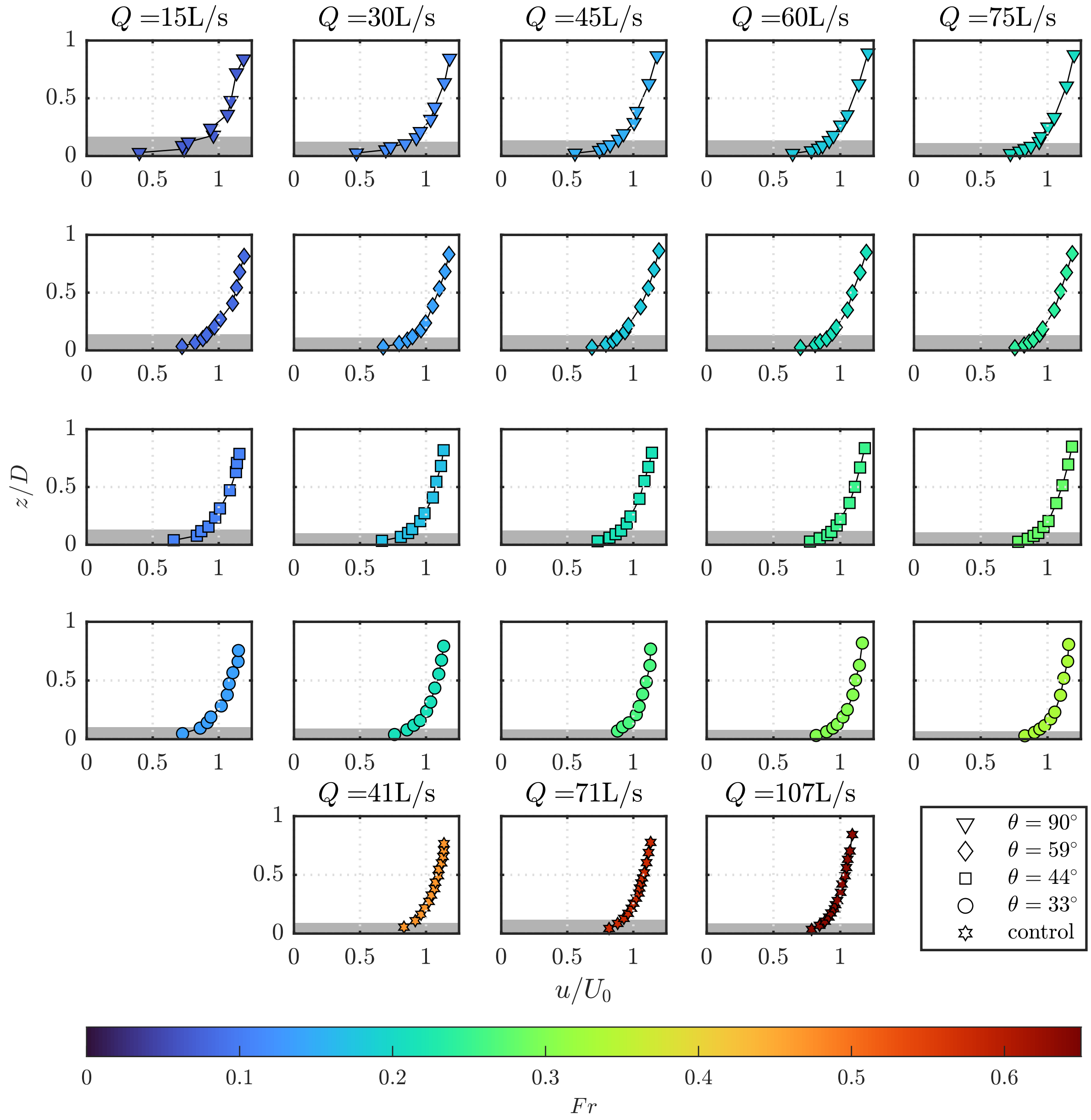

Figure 7.2: Dimensionless profiles of streamwise velocity for the HHLab ADV experiments. U_0 is the depth-averaged velocity (Q/A). Data points are color-coded based upon their value of Fr. The gray strip represents the dimensionless boundary layer displacement thickness, δ^*/D.

causes high-momentum fluid from the undisturbed outer flow region to be transported near the bed, where the action of viscous effects are locally important and energy is dissipated as heat. As discussed in Chapter 5, the increase in the slope of the water surface in the approach channel increases the practical difficulty of obtaining an accurate measurement of h at the gauging section.

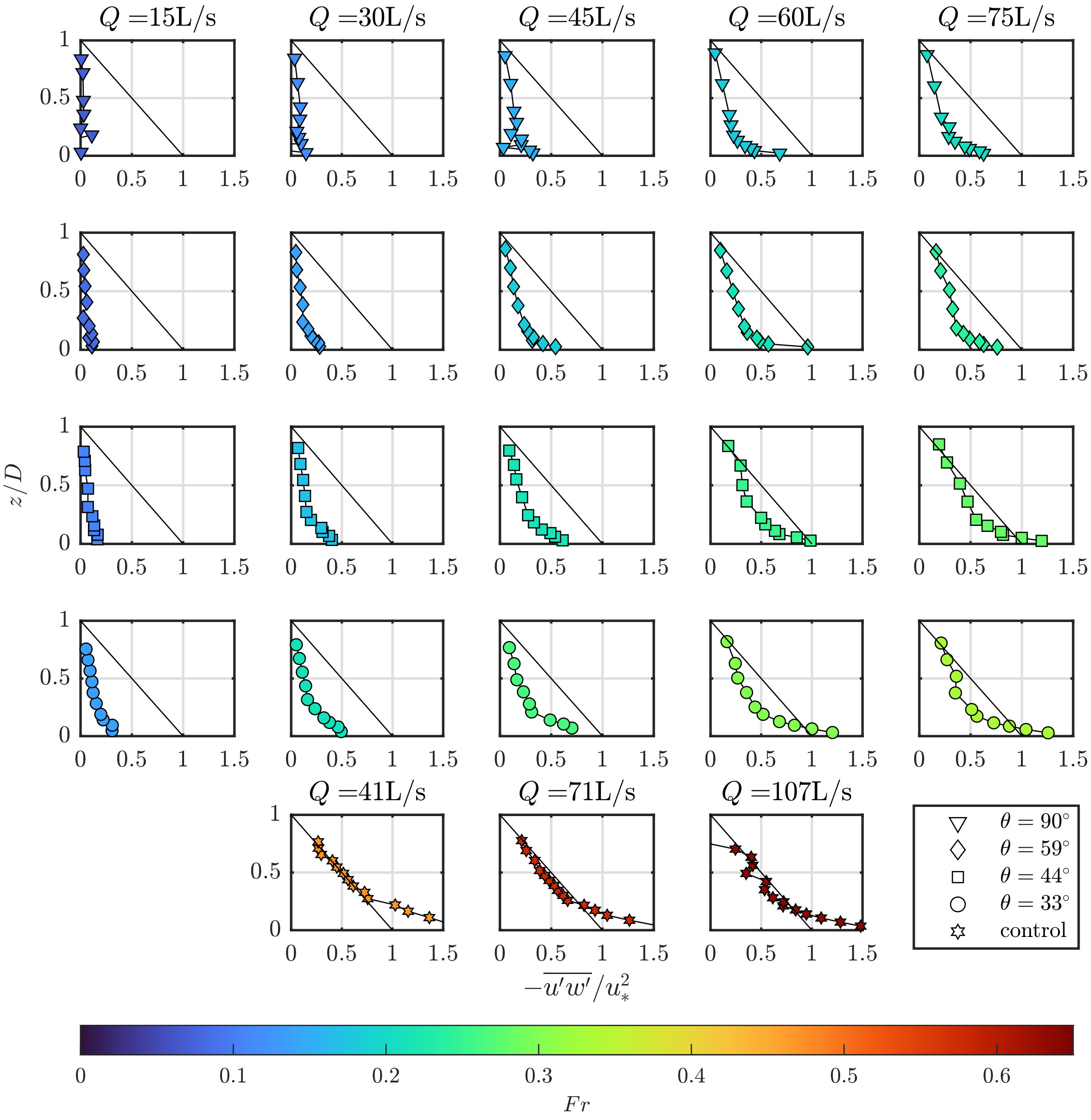

Figure 7.3: Dimensionless profiles of Reynolds stress for the HHLab ADV experiments. Data points are color-coded based upon their value of Fr. The solid black line represents the assumed distribution of fluid shear stress for fully developed two-dimensional open-channel flow.

7.3.3 Flow Separation and the Vertical Pressure Gradient

In Figure 7.1, it was observed that a break in the monotonic increase of C_c with h/p occurs for tilting weir flows. Analysis of vertical sharp-crested weirs in Chapter 5 revealed that this was due to increased draw-down in the free-surface caused by a collapse of supporting

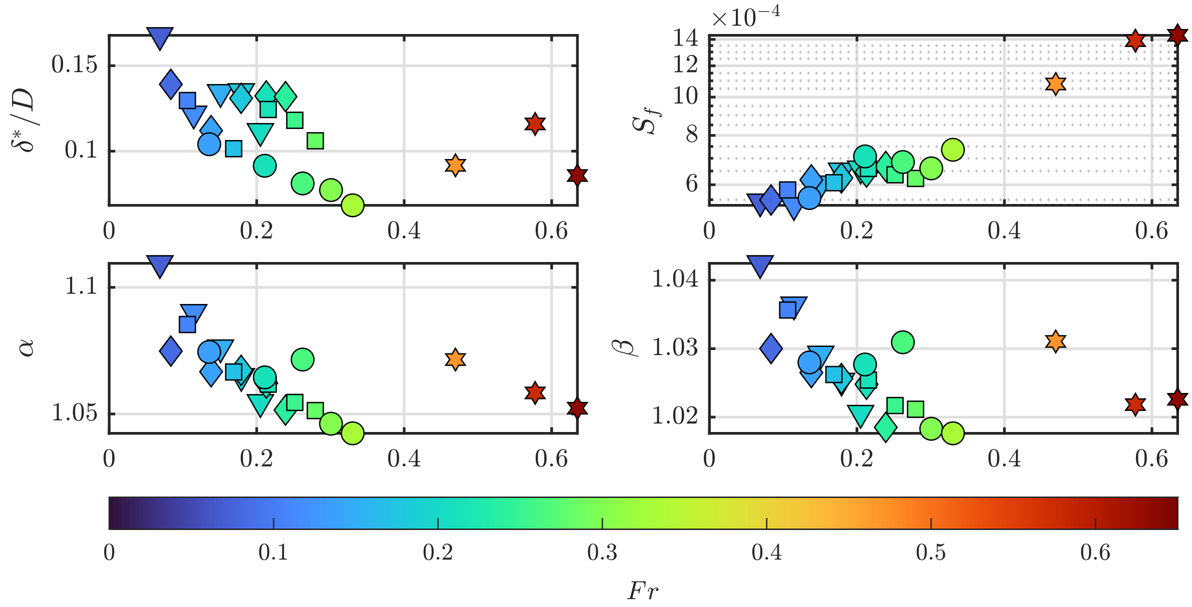

Figure 7.4: Depth-averaged flow profile quantities from the HHLab-ADV experiments. The figure legend is the same as in Figure 7.2 and Figure 7.3.

hydrostatic pressure underneath the nappe. For the tilting weir, we can examine how areas of flow separation and the orientation of streamlines contribute to a similar phenomenon.

Figure 7.5 shows the velocity quiver plots for the eight PIV experiments of the EFML-PIV data set. Overlaid on top of these vectors is the approximate area of the recirculation zone of separated flow. These areas are calculated by finding the x position along the bottom boundary where flow separation occurs, marked by a change in sign of $\partial u/\partial z|_{z=0}$ from positive to negative. This sign change occurs due to the adverse pressure gradient caused by the stagnation pressure at the bottom base of the weir. From this separation point, a separation streamline is traced using the two-dimensional velocity field and MATLAB *streamline* function, so that position coordinates in x and z are generated for the separation streamline. The area of separation flow is then calculated as:

$$A_s = \int_{x_s}^{x_b} \left[z(x)_s - z(x)_b \right] dx \; . \tag{7.14}$$

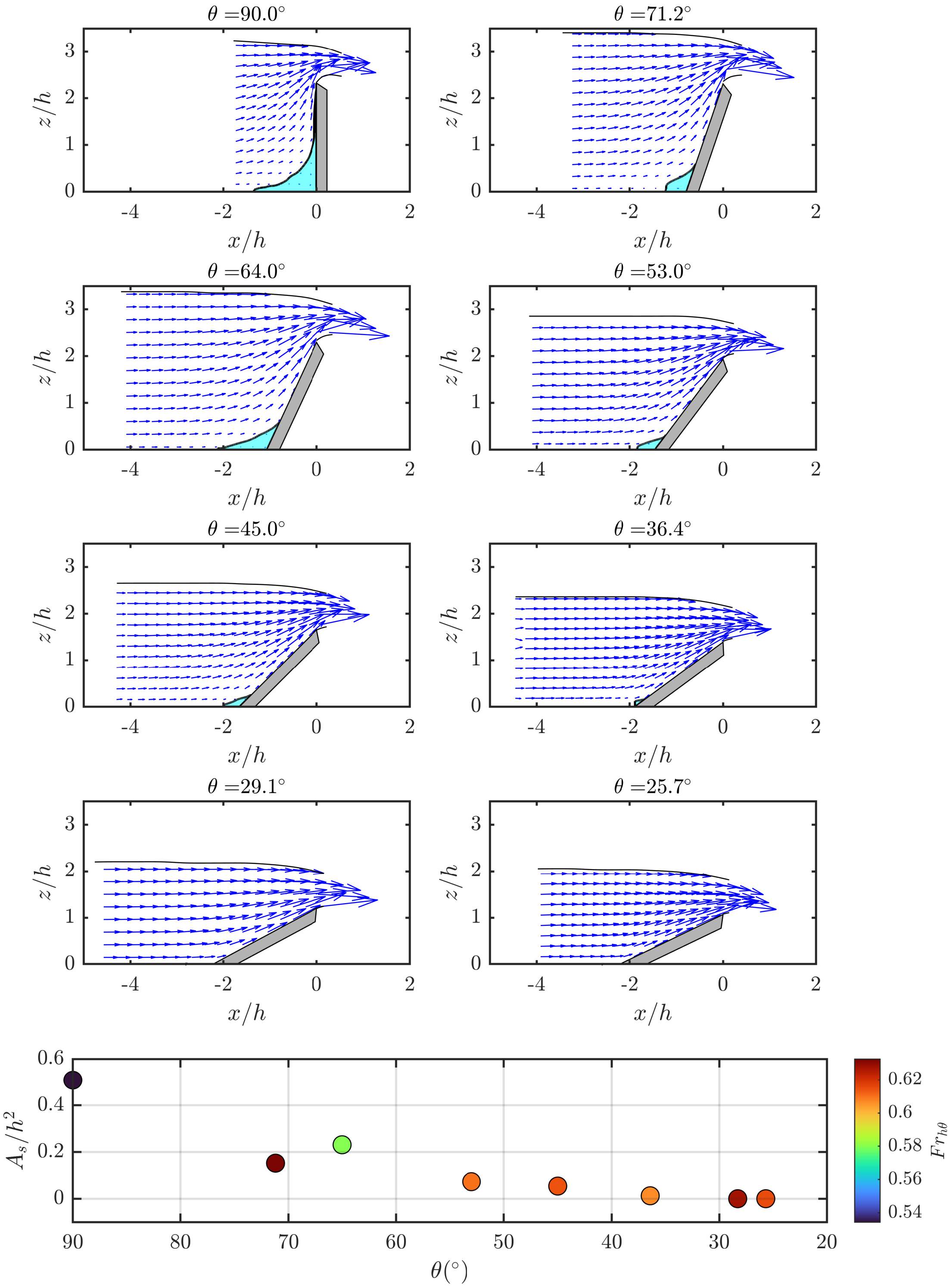

Figure 7.5: Velocity quiver plots with areas of flow separation overlaid on top for the EFML-PIV experiments. The bottom plot shows the estimated dimensionless separation area are with respect to θ, with points color-coded by their value of $Fr_{h\theta}$.

where x_s is the longitudinal position of the separation point, x_b is the longitudinal position of the weir geometry at the end of the separation streamline, and $z(x)_s$ and $z(x)_b$ are the vertical coordinates of the separation streamline and boundary geometry, respectively.

Observing Figure 7.5 and Table 7.1 it can be seen that as θ decreases the fluid velocity is distributed more towards the streamwise direction, resulting in less deflection of the lower nappe surface above the crest (ϵ/h). The area of the separation zone, made dimensionless by using h^2 as a scaling factor, appears to decrease monotonically with θ, and completely vanish for $\theta < 45°$. The decrease appears to be non-linear, in accordance with the nonlinear behavior of the k_θ term in Chapter 6. The observed trend of a decreasing separation zone with increasing flow inertia is opposite to what was reported by Rajaratnam and Muralidhar (1971) for sharp-crested weirs, but altogether represents a coherent trend with other aspects of the flow field dynamics observed in this chapter. As the flow inertia increases, the relative size of the boundary layer decreases, allowing for delayed or even a complete avoidance of separation. This trend is consistent with classical observations of wall-bounded flows, such as flow over a cylinder. As flow inertia decreases and the size of the separation zone grows, some amount of fluid is displaced by that occupied within the separated recirculation zone, thereby increasing h for the same q and decreasing $Fr_{h\theta}$.

At low values of $Fr_{h\theta}$, gravitational effects are dominant over inertial effects, and therefore significant deflection of the upper nappe surface is observed, making δ/h initially large. Increasing flow inertia allows the streamlines along the upper nappe surface to maintain a stream-wise orientation, causing δ/h to decrease - at least as long as there is an appreciable zone of separated flow at the base of the weir.

Because the fluid within the separated zone is slow-moving and nearly static, it acts like a foundation of hydrostatic pressure for the overflowing nappe. When the separation zone diminishes, increased drawdown in the free surface is observed, as in Figure 7.6. The amount of drawdown (δ/h) with respect to the free surface elevation at the gauging section can be observed in Table 7.1, and qualitatively by the size of the region in Figure 7.6 where

$0 < -(dP/dz)/\gamma < 1$, indicated by reduction in the hydrostatic pressure distribution due to streamline curvature. When $-(dP/dz)/\gamma \geq 1$, a hydrostatic pressure distribution exists that supports the overflowing nappe.

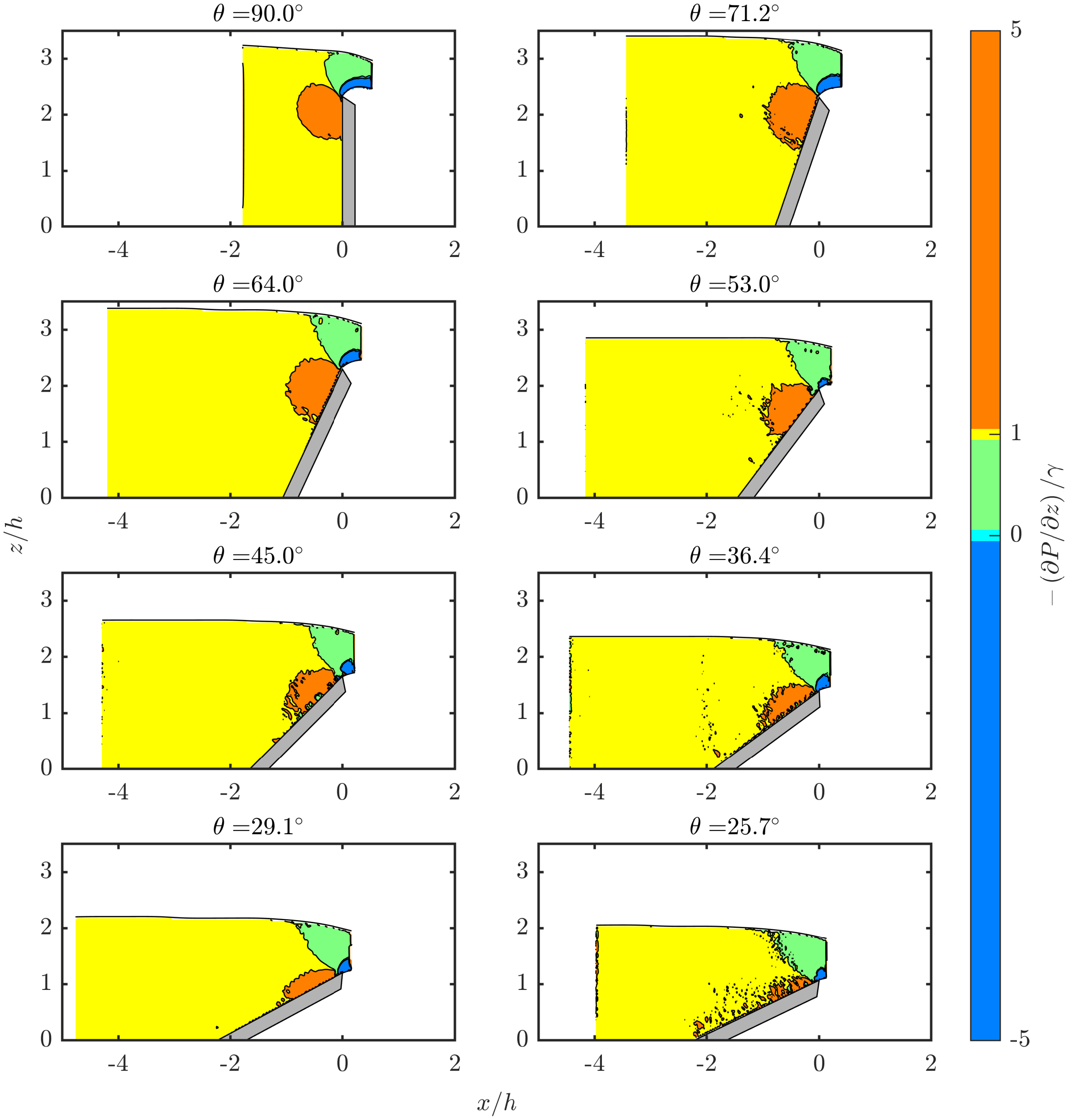

Figure 7.6: Dimensionless contour plots of the vertical pressure gradient for the EFML-PIV experiments. A variance of 0.05 is given for the color scale around 0 and 1.

7.3.4 Zones of Local Energy Loss

One long-standing question of interest for those studying weir flows is the applicability of inviscid flow-type analyses for solving the discharge characteristics and nappe profiles. One can already have a general idea of the applicability of potential flow assumptions by examining the magnitude of the velocity coefficient term, C_v, as seen in Table 7.1 and Figure 7.1. The magnitude of C_v generally falls within the range of 0.95–1. As previously mentioned, this coefficient represents a reduction in the observed jet velocity due to viscous energy losses, compared to what is theoretically predicted from assumptions of potential flow. This gives the indication that some amount of local energy loss is present and should be taken into account when predicting the discharge coefficient. Extensive studies on the behavior of C_v in application to jet nozzles has shown that this coefficient trends toward unity with increasing Reynolds number (Street et al., 1996). A similar increasing trend in C_v with h/p can be seen in Figure 5.4, giving the indication that local viscous losses became less appreciable with increasing flow inertia. It has also been shown that altering the exit condition of jet orifices to become more well-rounded also works to increase C_v.

Figure 7.7 plots an estimation of the dimensionless TKE dissipation rate, ε^*, as defined by Eq. (7.13), for the eight different EFML-PIV experiments. These plots reveal that the observed values of C_v from the bulk flow behavior can be substantiated by observed zones of local kinetic energy losses near the sharp-crest interface. These losses occur due to the irreversible transfer of energy from the mean flow field to the turbulent field by the combined action of Reynolds stresses and mean flow velocity gradients. This energy is eventually dissipated through the action of local deformation in the turbulent field captured by the turbulent strain rate tensor s'_{ij}. Examining the magnitude and extent of the dissipative zones shown in Figure 7.7, they appear to decrease as the inclination angle lowers, which is likely due to the smoother angle of the approaching streamlines as the flow navigates the sharp crest.

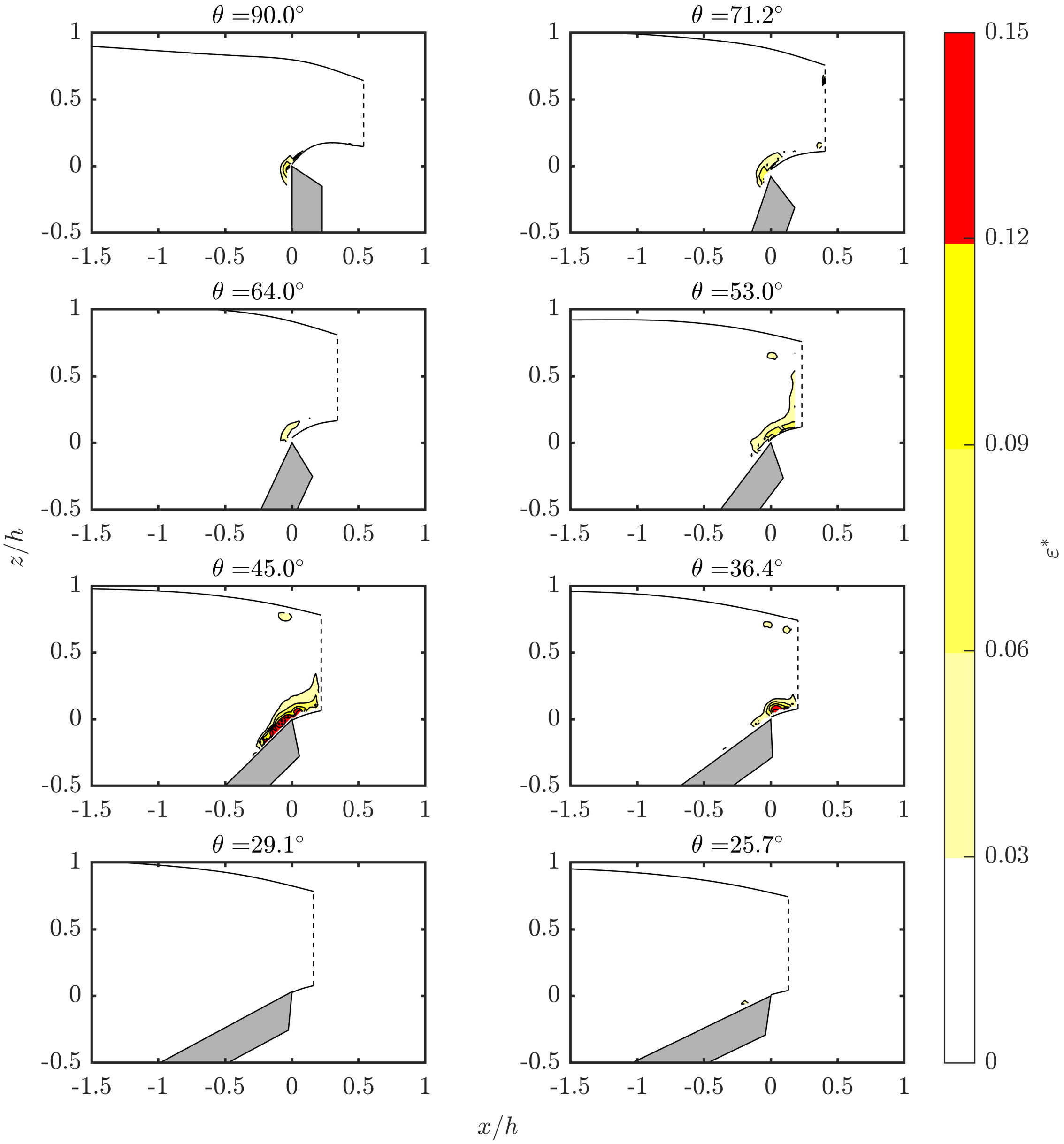

Figure 7.7: Dimensionless contour plots of turbulent kinetic energy dissipation rate for the EFML-PIV experiments. Free-surface boundaries shown by the curved solid black line, with the limit of the PIV measurement window shown by the dashed black line.

The trends observed in Figure 7.7 are certainly preliminary in nature and deserve further investigation. One limitation of note is that here we are estimating ε^* under the two-dimensional flow assumption. This assumption may be valid for approximations of the mean flow field, but it is, strictly speaking, incorrect for estimating quantities of the turbulent flow field. This is due to the inherently three-dimensional phenomenon of vortex stretching, which is the engine driving the turbulent energy cascade (Pope, 2000). However, even with these limitations, three important insights can be drawn from this investigation of zones of local energy loss:

1. Energy loss in the weir flow problem is primarily due to small localized regions of high shear near the sharp-crested, rather than distributed losses along the boundary.
2. Zones of local kinetic energy loss appear to generally decrease in size as θ decreases, although some anomalies in this trend are present. Regardless, this helps to validate the incorporation of C_v as part of a conceptualization of the overall discharge coefficient.
3. Opportunities for improved tilting weir design are available by designing the near-crest region to feature a more stream-lined approach to reduce regions of high shear in the mean flow field.

Further investigation into the careful quantification of TKE dissipation for weir flows using three-dimensional numerical simulations or stereoscopic PIV is warranted.

7.3.5 The Transition from the Weir to Sill Regime for Tilting Weirs

One issue of concern for tilting weir flows is the point where the monotonic trend in the contraction coefficient stops - indicative of a transition from a weir flow regime to a sill flow regime. The discharge equation laid out in Chapter 6 is not suitable for sill-type flows, and thus it is important to understand which combination of θ and h/p leads to a departure from the expected weir flow behavior that is significant enough to be classified as a sill-type of flow. In Chapter 5, a value of $h/p \approx 8$ ($Fr = 0.95$) was determined to be the threshold value. The EFML-CFD simulation results presented in Figure 7.1 indicate that for the flow case were $\theta = 9^\circ$ and $h/p = 5$, the flow had transitioned to a sill regime. Based upon these threshold points, a preliminary demarcation between the weir and sill regimes for tilting weir flows is shown in Figure 7.8. A simple decaying logistic function is shown to estimate the

h/p threshold value. However, additional simulations and experiments are likely necessary to gain more confidence in this threshold definition.

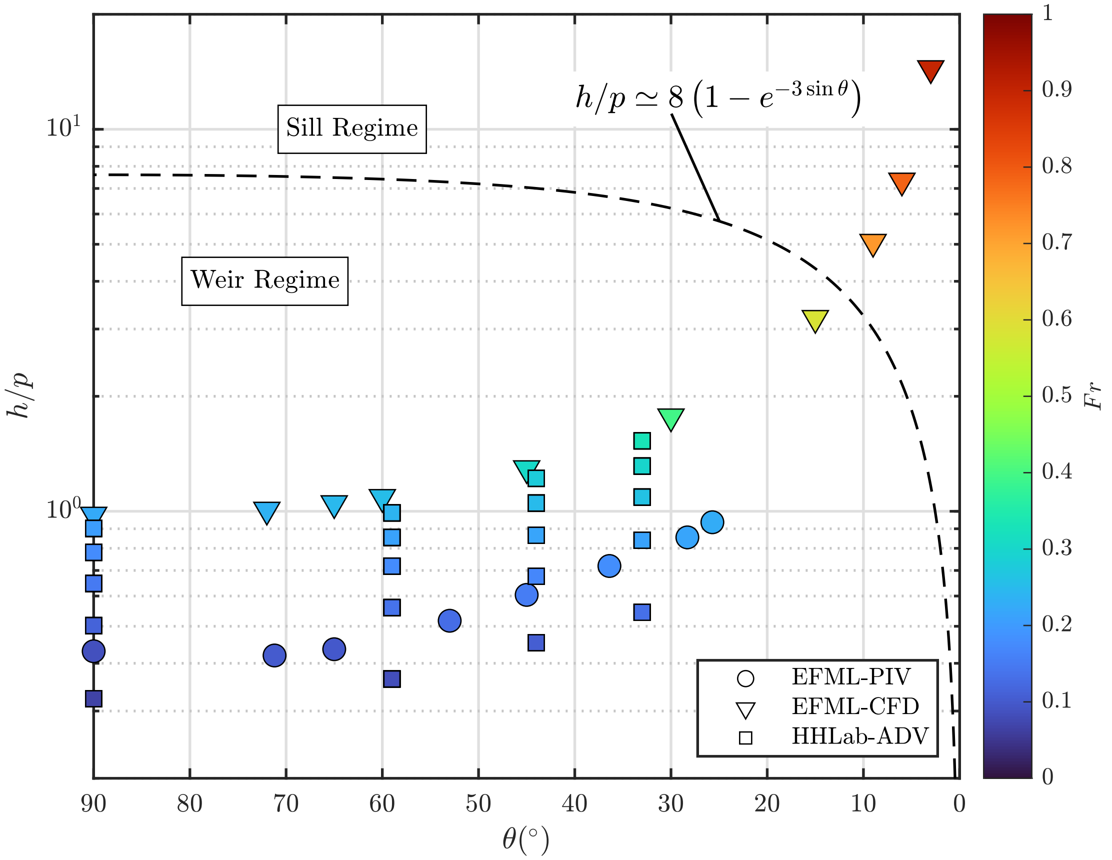

Figure 7.8: Values of h/p shown vs. θ and color-coded by Fr to illustrate the transition from a weir flow regime to a sill flow regime for the tilting weir. An equation to approximate the threshold h/p value for the transition from weir to sill flow based upon the value of θ is shown by the dashed line.

7.4 Conclusions

This chapter has examined different aspects of the flow field dynamics influencing the discharge characteristics of flow over tilting weirs. Supporting evidence was found for the approach taken in Chapter 6, where the tilting weir is treated as type of sharp-crested weir. Increasing the flow field inertia with respect to gravitational effects by decreasing θ was found to have similar effects on the flow field dynamics compared to increasing h/p for the sharp-crested weir. The primary influences on the discharge characteristics for tilting weirs were found to be the influence of kinetic energy, represented by K, with the behavior of C_c being indicative of a transition between weir and sill regimes of flow.

Chapter 8

Application of Tilting Weirs to Prototype-Scale [4]

8.1 Introduction

8.1.1 Tilting Weir Flow Rating Fundamentals

Tilting weirs (also known as overshot gates, crest gates, LayFlat gates, and pivot weirs) are commonly used to regulate water levels in natural and artificial channels, as well as gates on dam spillways. They have also been investigated in the past several decades as a viable flow measurement device using laboratory model studies (Wahlin and Replogle, 1994; Bijankhan and Ferro, 2018; Pugh et al., 2024). Although reliable flow measurement structures for channel flow are available in long-throated flumes and weirs (Bos et al., 1984; Wahl et al., 2005), the motivation for investigating tilting weirs for flow measurement is found in their dual functionality. Several commercially available tilting weir-type structures are available on the market for field application (e.g. Obermeyer Hydro Inc. pneumatically actuated gate, Rubicon Water FlumeGate, Mueller Water Products overshot gate, Waterman Valve LLC Tilting Weir, etc.). However, thus far there has not been an investigation in the literature to examine if laboratory-derived stage-discharge relationships for tilting weirs are appropriate for these structures. this study provides the first comprehensive synthesis of field calibration data of flow over tilting weirs, developing a generalized framework that can be applied across diverse field sites.

---

[4] The research presented in this chapter has been submitted in revised form upon anonymous peer review to the *Journal of Irrigation and Drainage Engineering* under the title "Field Calibration of Flow Over Tilting Weirs in Canals" by J.E. Pugh, T.K. Gates, and S.K. Venayagamoorthy. This chapter is written to reflect and acknowledge the contribution of the co-authors.

Flow over a tilting weir is driven by gravity. At the gauging section in the approach to the weir, the flow is one-dimensional and hydrostatic. The flow then accelerates and converges at the crest, inducing a non-hydrostatic pressure distribution. Downstream of the crest, a free-falling jet (or nappe) forms (see Fig. 8.1), which then plunges into the downstream pool, entraining air in the process. The hydraulic control point occurs when the flow passes through a critical section just downstream of the crest, where the lower nappe elevation is maximum and specific energy is minimized (Castro-Orgaz and Hager, 2017). The discharge, Q, is estimated by measuring the water surface elevation upstream at the gauging section, where the flow depth is D. The head, h, is defined relative to the crest height, p, with the datum taken as the bottom sill on which the structure is mounted. The inclination angle θ is defined by $\sin^{-1}(p/L)$, where L is the weir plate length. Unit discharge, $q = Q/b$, and velocity head contribute to the total hydraulic head, $H = h + \alpha U_0^2/2g$; where $U_0 = q/D$.

An important dimensionless parameter for this study is the channel Froude number in the prismatic control section:

$$Fr = q/\left[\sqrt{g}(h+p)^{3/2}\right] \ . \tag{8.1}$$

The classical weir-discharge rating equation is the Poleni equation:

$$Q = C_d \frac{2}{3} b \sqrt{2g} h^{3/2} \ , \tag{8.2}$$

where g is the gravitational acceleration constant, and C_d is well-approximated for $h/p \leq 5$ using the equation of Kindsvater and Carter (1959):

$$C_d \simeq 0.602 + 0.075 h/p \equiv \xi(h/p) \ , \tag{8.3}$$

which is valid for vertical ($\theta = 90°$) sharp-crested weirs. For ease of notation, this semi-empirical equation is given the symbol $\xi(h/p)$.

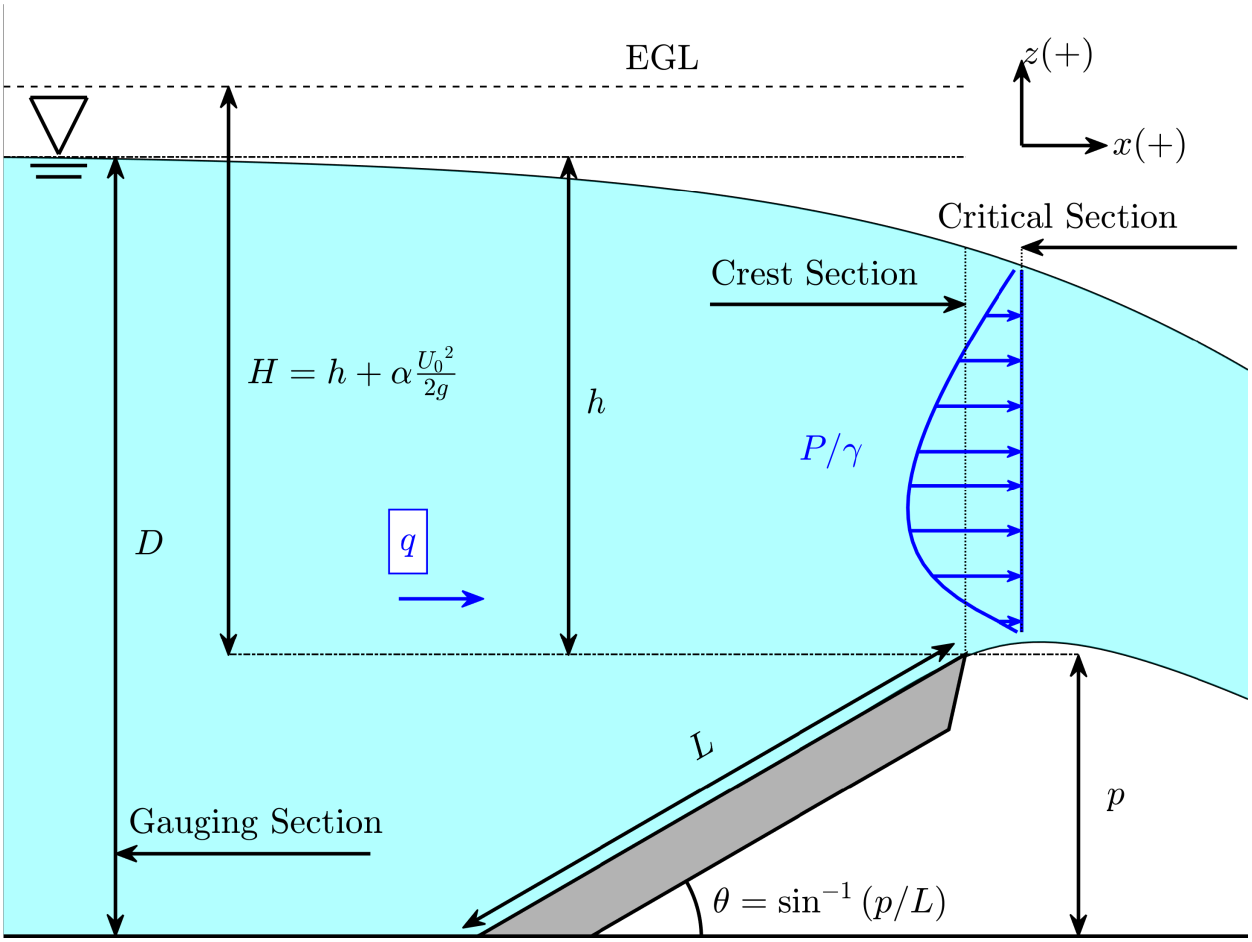

Figure 8.1: Schematic of flow over a tilting weir, where $h/p = 1.77$ and $\theta = 30°$. EGL is the energy grade line, shown by the dashed line. All dimensions shown are to scale.

Laboratory studies on tilting weir flows were reviewed recently in Pugh et al. (2024). This study built upon previous works of Bazin (1898), Bureau of Reclamation (1948), and Wahlin and Replogle (1994) by examining physical models of tilting weir flows in two separate rectangular flumes. They proposed an adaption of Eqs. 8.2 and 8.3 to the more general case of tilting weir flows by applying an angle-correction factor, k_θ, to the head term h. The dimensional discharge (Q) and dimensionless discharge coefficient ($C_{d\theta}$) are then calculated as:

$$Q = \xi(h/p)\frac{2}{3}b\sqrt{2g}(hk_\theta)^{3/2} \rightarrow C_{d\theta} = \frac{Q}{\left[\frac{2}{3}b\sqrt{2g}(hk_\theta)^{3/2}\right]}\ , \tag{8.4}$$

where $C_{d\theta}$ still remains well-approximated by $\xi(h/p)$. k_θ can be approximated by:

$$k_\theta \simeq -0.07(\sin\theta)^{4.5} + 1.07 \equiv \Omega(\sin\theta) \,, \tag{8.5}$$

and for ease of notation, Eq. 8.5 is given the symbol $\Omega(\sin\theta)$. Wahlin and Replogle (1994) and Pugh et al. (2024) found that for $\theta < 20°$, it became practically difficult to maintain free flow of the nappe (especially without a significant drop in the downstream channel bed elevation). Therefore, Eq. 8.4 is only valid for $\theta \geq 20°$. Pugh et al. (2024) also discussed the importance of considering scale effects at low values of h and ensuring sufficient ventilation of the nappe. They suggested that, in accordance with Kindsvater and Carter (1959), C_d remains a function of only h/p as long as $(hk_\theta) > 5$ cm (for water under standard conditions). For h values lower than this threshold, viscous effects alter the discharge characteristics, and surface tension effects can cause the overflowing nappe to cling to the weir surface. A lack of sufficient atmospheric pressure underneath the nappe will result in an artificial decrease in the upstream water level at the gauging station. When the air pocket below the nappe is under-pressurized or fully collapsed, this is a condition of clinging flow (Johnson, 2000; Sinclair et al., 2022). This contrasts with submerged flow, where the downstream tailwater elevation rises sufficiently above the structure crest elevation, to drown out the critical flow condition in the control section (Bureau of Reclamation, 2001). When the weir is operating normally between these two extremes, the flow can be described as “free” or “springing” (Johnson, 2000).

8.1.2 Applying Laboratory-Derived Approaches in the Field

The application of laboratory-derived stage-discharge relationships to structures in the field has been previously investigated for sharp-crested weirs (Soulis and Dercas, 2012), broad-crested weirs (Clemmens et al., 1990), and briefly by Wahlin and Replogle (1994) for tilting weirs. The approach for such a task can be well-formulated by examining the

WinFlume software (Wahl et al., 2000). General considerations when calibrating a flow measurement structure in the field are:

1. The construction material (and associated roughness height) of the approach channel, the prismatic control section channel, and the flume or weir plate.
2. Areas of flow separation creating local energy losses between the gauging section and the control section.
3. Significant changes in the approach channel velocity distribution compared to laboratory experiments due to: curvature, surface shear (i.e., wind or waves), or channel boundary shear (i.e., channel boundary material or vegetation).
4. Sediment deposition upstream of the control section altering the dynamics of boundary layer separation upstream of the structure crest.
5. Tailwater conditions and/or ventilation conditions below the nappe affecting the free-flow capacity of the weir.

For field calibration of tilting weirs, items 3–5 are likely to be most important. Energy losses due to surface friction must be considered for the free overfall, long-throated flume, or broad-crested weir (Rajaratnam et al., 1976). However, these losses can be neglected for weir flows due to the small size of the boundary layer in relation to the overall flow field (Bos et al., 1984). However, local energy losses due to flow separation between the gauging section and critical section (and especially near the weir crest) can still be significant (Bureau of Reclamation, 2001; Pugh et al., 2025). Additionally, Schoder and Turner (1929) showed that major changes in the velocity distribution of the approach channel led to variances in the predicted discharge of as much as 26%. Finally, in sediment-transporting channels, the ability to pass sediments through a structure is of critical importance, and can have a major effect on the approach flow conditions and resulting head-discharge relationship (Bos and Wijbenga, 1997). Although tilting weirs are dynamic structures that can be operated in such a way to allow for sediment passage, this does depend on operational priorities and thus accumulation of sediments over time could be a major consideration for field calibration.

What has been absent from the literature until now is a concerted effort to compile the existing data on flow observations of prototype-scale tilting weirs under various field conditions to examine how well a laboratory-derived relationship for the stage-discharge curve applies. To meet this need, this study aims to:

1. Compile and describe collected data on tilting weir flows in the field.
2. Examine the viability of a laboratory-derived stage-discharge relationship for field application.
3. Consider first and second-order effects explaining variances in discharge characteristics between the laboratory and field.
4. Recommend operational guidelines and further research for prototype-scale tilting weirs.

8.2 Methodology

8.2.1 Characterization of Field Datasets

This study features the compilation of four separate field study campaigns of discharge measurements of tilting weirs of various sizes, the dimensions of which are given in Table 8.1. The following sections detail the background of each field measurement campaign, the type of tilting weir studied, and the uncertainty associated with measurements.

8.2.2 Kutlu 2019 (K2019) and Current Study (PGV2025)

Data collected in the field by the authors included those during the 2024 irrigation season (PGV2025), and during the 2017 and 2018 irrigation seasons (K2019). The K2019 data were published previously in a Colorado State University M.S. thesis by Caner Kutlu (Kutlu, 2019). Both data sets were obtained from observations on the three same Obermeyer-type

Table 8.1: Description of structures examined and range of flow characteristics.

Weir Name	Study Name	b (m)	L (m)	n	θ (°)	h (mm)	Q (L/s)	Fr
Montgomery (A)	K2019A	6.71	1.52	46	23.6–34.6	195–832	491–9201	0.02–0.25
Magnuson (B)	K2019B	6.10	1.92	35	35.3–40.4	216–844	660–8676	0.02–0.17
Mulberry (C)	K2019C	4.57	1.85	4	22.8	613–686	4133–4852	0.19–0.20
Montgomery (A)	PGV2025A	6.71	1.52	6	25.5–33.1	539–854	4905–11263	0.15–0.28
Magnuson (B)	PGV2025B	6.10	1.92	4	30.2–39.4	439–679	4425–7510	0.11–0.19
Mulberry (C)	PGV2025C	4.57	1.85	5	31.2–32.3	505–667	3076–4983	0.12–0.17
Oasis	WR1994	1.63	1.70	40	20.2–49.0	212–393	352–863	0.04–0.17
Golden Gate Weir No. 1	HG-C2020	24.38	1.83	7	22.9–69.5	149–469	2461–15424	0.01–0.16
				Σ147				

tilting weirs located within the Larimer and Weld irrigation canal, owned and operated by the Larimer and Weld Irrigation Company in Weld County, Colorado, USA (see Fig. 8.2).

The studied weirs have been labeled A (Montgomery Weir), B (Magnuson Weir) and C (Mulberry Weir) for ease of notation. These weirs were chosen because they represented critical points along the system where a flow estimation served to improve operational efficiency. The general site characteristics of each of the weirs can be viewed in the photographs in Fig. 8.3 and in Appendix B. The approach channels at each of the three weirs were long, straight, and of fairly uniform roughness. The earthen canal in which the weirs were installed was composed primarily of clay, covered by deposits of sand and grassy vegetation along the banks. Offtake structures (see Fig. B.2) for irrigation water diversion were installed at intervals upstream from each of the weirs. Downstream from the structures, there were concrete slabs to support the weir hinge and air bladder, followed by concrete blocks and rip-rap placed on the canal bed to dissipate energy. The characteristics of the weir plates were far from smooth and of homogeneous roughness, being originally steel plates now covered with a rust layer. The weir plates themselves were slightly curved and had stiffness plates that were mounted parallel to the flow direction (see Fig. B.1).

Each weir had an existing stilling well positioned on the upstream side to facilitate flow depth measurements. The distance between the stilling wells and the crest was measured to range from 1.22 m to 2.13 m, depending on the setting of θ. This distance proved insufficient

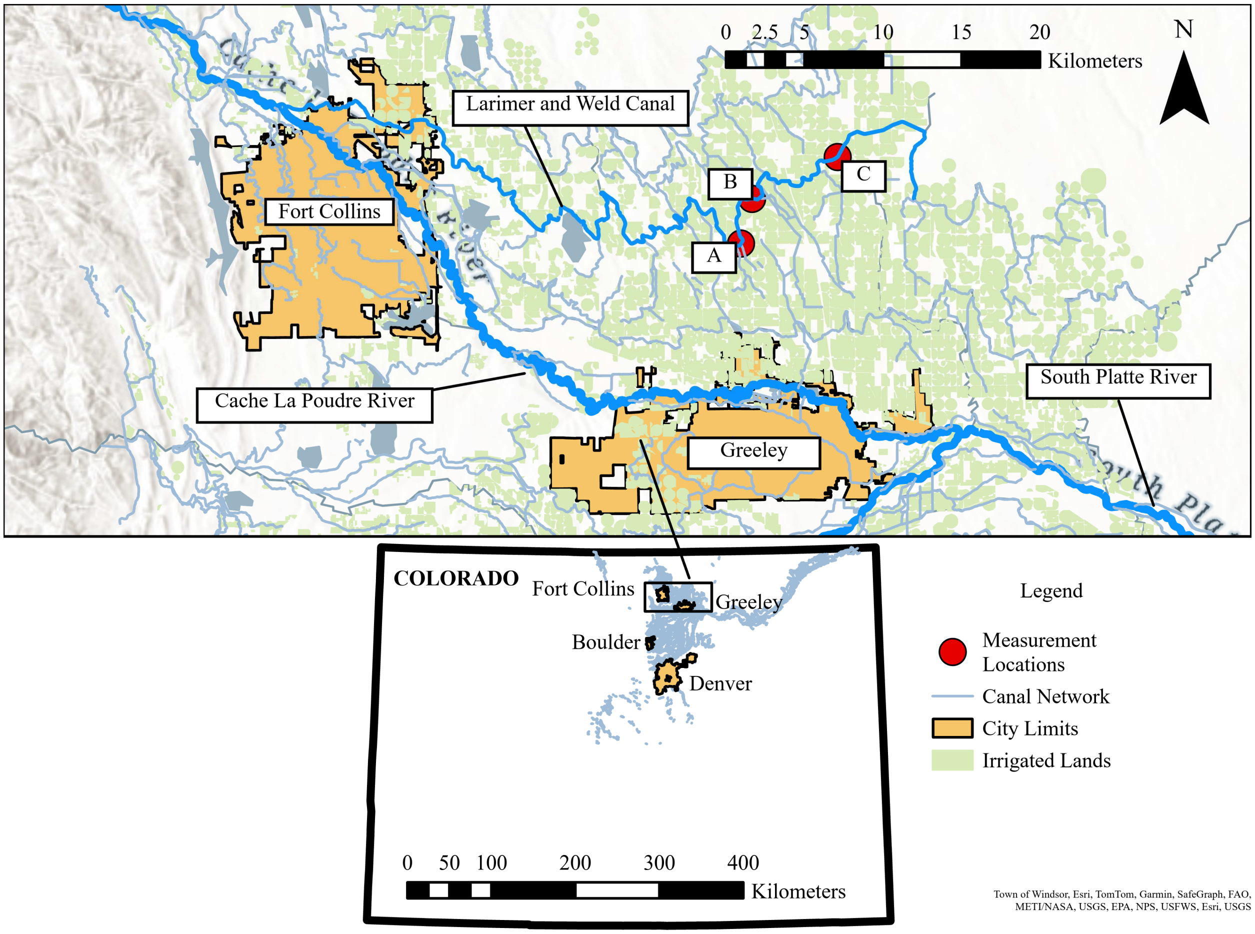

Town of Windsor, Esri, TomTom, Garmin, SafeGraph, FAO, METI/NASA, USGS, EPA, NPS, USFWS, Esri, USGS

Figure 8.2: Map of field study area for studies K2019 and PGV2025 within Colorado, USA.

to keep the gauging section upstream from the accelerating draw-down flow-field of the weir; thus, temporary stilling wells were installed within the channel upstream of the crest and just downstream of the flow measurement section (see Fig. 8.4). Air ventilation of the nappe was primarily supplied by diverging sidewalls downstream of the crest. Flow toward the weirs was guided by concrete retaining walls built diagonally to the flow direction in the upstream approach to the weir, and parallel to the flow direction near the weir crest. The retaining walls downstream of the weir expanded to allow for ventilation of the nappe (see Fig. B.3). It was found that the divergence angle of the retaining walls at Weir B was insufficient for proper ventilation. Free flow capacity at Weir A was increased by a drop in the bed elevation downstream of the crest.

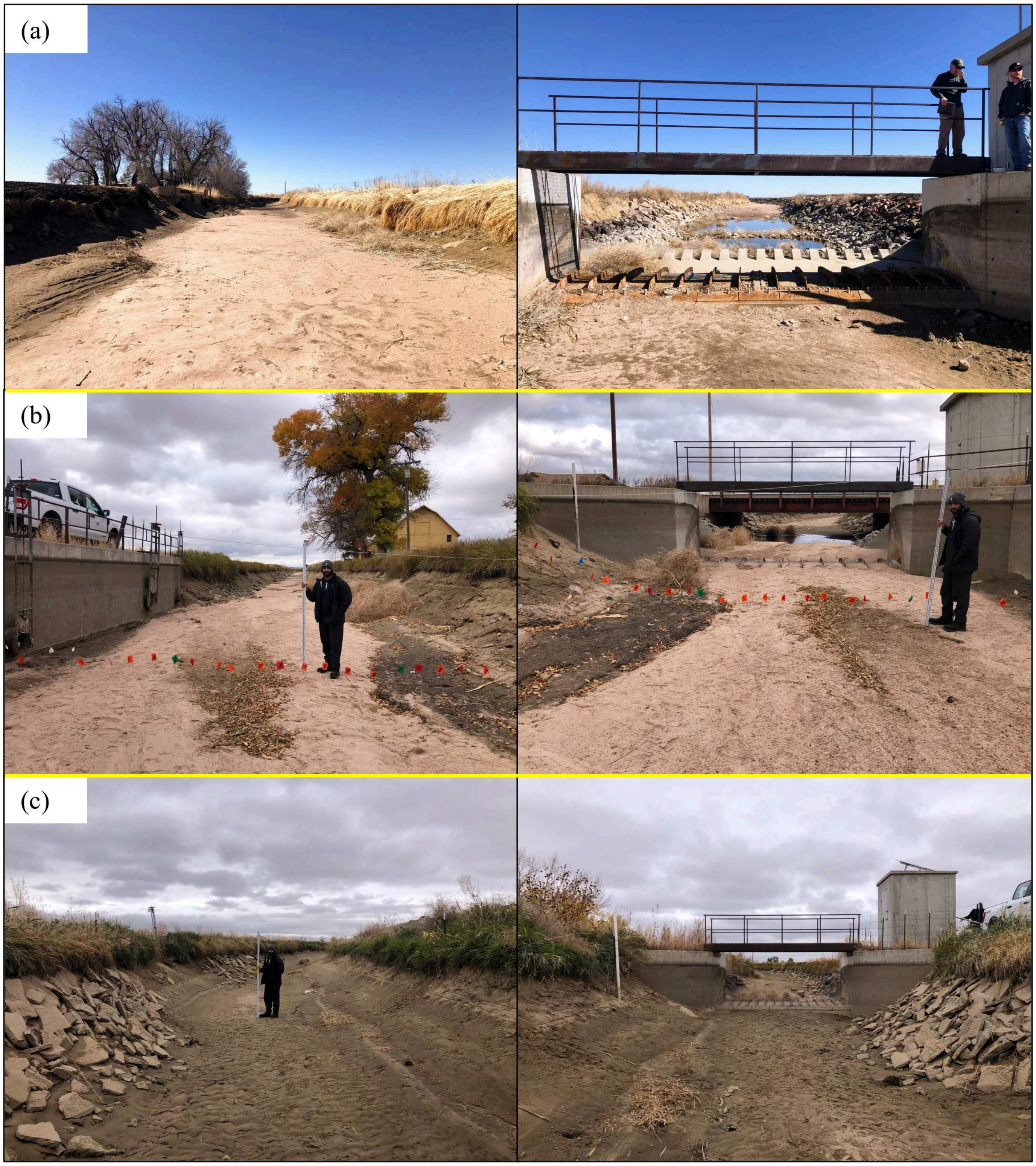

Figure 8.3: Photographs of dewatered measurement locations (a) Weir A; (b) Weir B; and (c) Weir C. Details are given in Table 8.1. Weirs are not inclined and are laying flat. View in left panel is upstream, view in right panel is downstream.

Flow Discharge Measurements

A 2,000 kHz Teledyne Marine StreamPro acoustic Doppler current profiler (ADCP) was used in this study to estimate Q during periods of nominally steady flow. Data collection

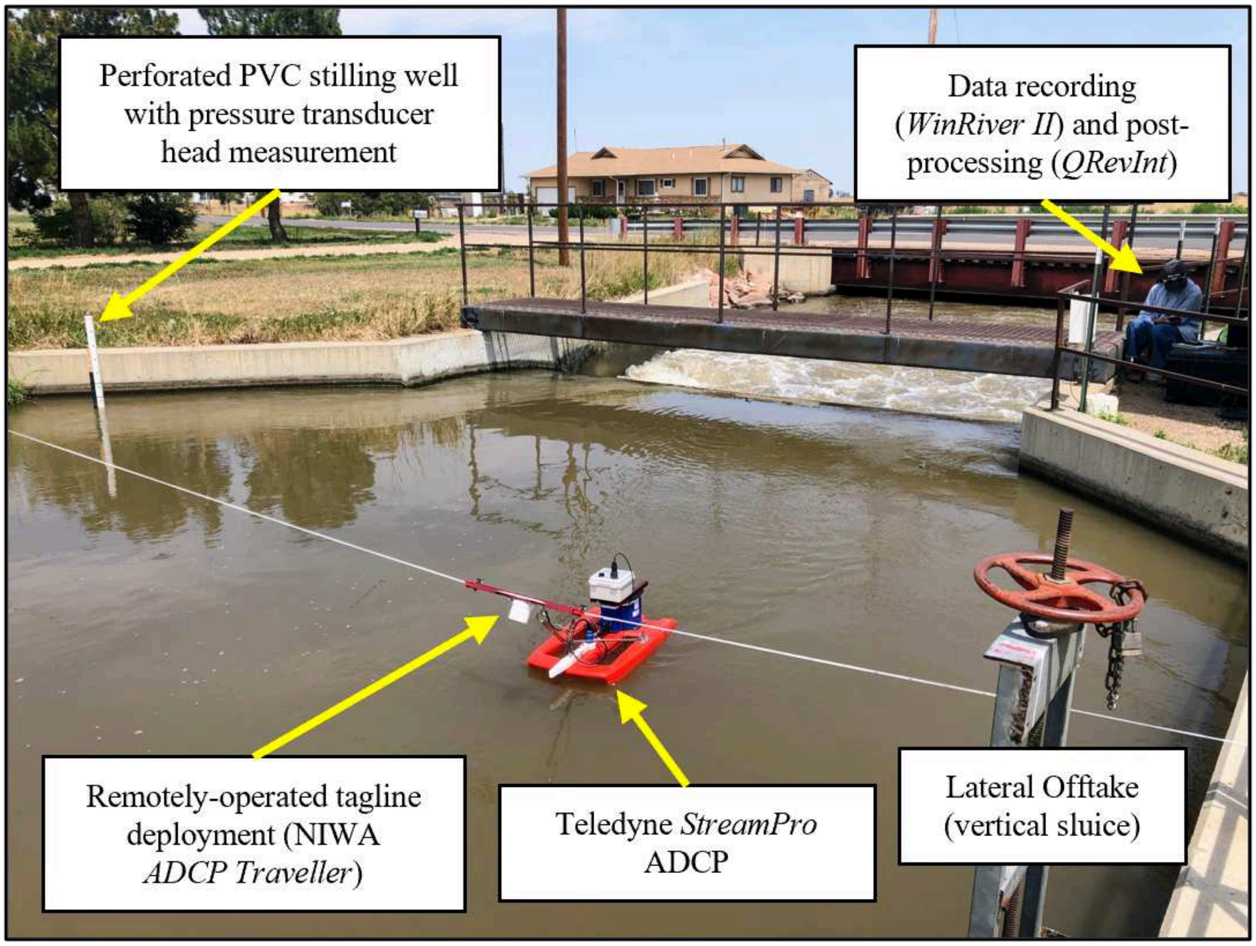

Figure 8.4: Example of PGV2025 ADCP moving boat flow measurement procedure at Weir B. $Q = 7510$ L/s; $h = 679$ mm; $\theta = 30.2°$. View is downstream.

was achieved using the *WinRiver II* software (v. 2.24). Flow measurements were performed at transects slightly upstream of the weirs (see Fig. 8.4). The ADCP was operated in bottom-tracking mode to determine the flow velocity relative to the channel bed. Moving bed tests were performed before each of the flow measurements to account for a mobile bed. A moving-bed condition was observed at all weirs during the higher flow events, which contributed to increased measurement uncertainty.

For the K2019 study, an even number of transects of the boat-mounted ADCP, ranging from four to ten, were performed along the cross-section at each measurement location using a manual rope-and-pulley method. A minimum of four transects were collected, with additional transects recorded as necessary to ensure that the total exposure time exceeded the general guideline of 720 s recommended by Mueller et al. (2013). To quantify a band of uncertainty in discharge measurements, the relative standardized uncertainty (RSU) in percent, was calculated following the guidance of Huang (2012). This allowed for the approximation of standard deviation that was not biased by the magnitude of the mean discharge or the number of transects, after which a 95% confidence interval for each discharge measurement was calculated using a z-score of 1.96.

For the current study, improved guidelines on reducing and estimating the uncertainty in ADCP discharge measurements were made in the intervening six years since the K2019 study. A remotely operated tagline deployment (NIWA *ADCP Traveller*) was used to achieve better uniformity in the ADCP boat travel speed, and a minimum of four transects were collected where the time per transect was at least 240 s, after the recommendations of Pugh et al. (2021). Although these general guidelines are available for exposure time, they represent a rule-of-thumb. Recent worked has focused on more accurately defining the recommended exposure time based upon direct *in-situ* measurements of the timescale of the largest eddies in the flow (González-Castro and Lee, 2020; Díaz Lozada et al., 2021).

The ADCP velocity and bathymetry data collected in *WinRiver II* were post-processed using the *QRevInt* software (v. 1.31 - Genesis HydroTech LLC, Mueller (2016)), which allowed for an estimation of discharge measurement uncertainty as a 95% confidence interval, calculated using the OURSIN method (Naudet et al., 2019; Despax et al., 2023).

Flow Depth Measurements

For the K2019 study, values of h for each Q measurement were determined by reading a staff gauge located on the control channel side-wall using a calibrated auto-level. For the PGV2025 study, temporary stilling wells were installed just downstream of the flow measurement section using perforated PVC pipes. The slots of the stilling wells were aligned perpendicular to the stream-wise direction to prevent sediment accumulation within the wells. Inside each well was an Onset HOBO water level logger to measure the hydrostatic pressure on the canal bed. A logger was also placed above the water level surface at Weir A to measure the atmospheric pressure. Continuous measurements of flow depth were logged for the entirety of the measurement campaign at a five minute interval, which allowed for the eventual calculation of an average flow depth during the measurement time window, along with a standard deviation for the measurement to characterize uncertainty. At the end of the irrigation season, the channel cross-sections were surveyed.

Calculations of h were done by finding the relative elevations of: the channel bed at the location of the stilling well, the bottom sill on which the tilting weir was mounted, and the crest at the time of measurement. A 95% confidence interval in the value of h was determined for each measurement from the standard deviation in water level measurement during the ADCP flow measurement time window. These uncertainties bands were found to be small - on the order of $\pm 1\%$ of h.

Weir Inclination Measurements

For both the K2019 and PGV2025 studies, θ was determined during flow conditions by measuring the vertical distance between the weir crest and the top of the concrete retaining wall with a surveying rod. Then, knowing the total distance between the bottom sill elevation and the top of the retaining wall, the crest height, p, could be computed. θ was determined, as shown in Fig. 8.1, as $\theta = \sin^{-1}(p/L)$.

8.2.3 Wahlin and Replogle 1994 (WR1994)

Stage-discharge data on a prototype-scale tilting weir situated within the Oasis Canal of the Imperial Irrigation District of Southern California were collected in November 1993 and originally published in Wahlin and Replogle (1994). The channel was trapezoidal and concrete-lined, with a 0.61 m bottom width and 1.25:1 side slopes. Discharge measurements were made using a broad-crested weir downstream of the tilting weir, which was reported by Wahlin and Replogle (1994) to have an error of ±2%. It is not clear how this determination of measurement error was made, but its value is consistent with other characterizations of measurement error for broad-crest weir and long-throated flumes (Bureau of Reclamation, 2001). Head measurements were made using a movable stilling well and point gauge system, accurate to ±1%. These accuracy ratings were also taken to characterize measurement uncertainty.

8.2.4 Hajimirzaie and González-Castro 2020 (HG-C2020)

Discharge data of flow over a tilting weir along the Golden Gate Canal located within the Big Cypress Basin of the South Florida Water Management District (SFWMD) were collected in 2014 and previously published in the discussion article by Hajimirzaie and González-Castro (2020). The Golden Gate Canal is unlined and has a trapezoidal cross-section geometry, with side slopes of 1:2 and bottom widths of 21.3 m and 27.4 m on the respective upstream and downstream sides of the structure. The bed and bank material primarily consists of sands. The head and inclination angle measurements for these field measurements were provided by the second author of this discussion (González-Castro, personal communication, August 2023). These data were collected in 2014 on a triple-bay tilting weir named Golden Gate Weir No. 1, which functions primarily as a barrier to prevent saltwater intrusion, while also providing flood control. The crest of the weir is varied using a hydraulic hinge-support system powered using an electric motor. Discharge measurements were made using a 1200 kHz Teledyne Marine RiverPro ADCP, with uncertainties calculated using the *RiverFlowUA* Mathematica package (González-Castro et al., 2016). This package computes the total calibration uncertainty by propagating the calibration uncertainties of the quantities measured by the ADCP system based on the First Order Taylor Series and the precision uncertainty of the ADCP and measurement environment estimated statistically from multiple transects (González-Castro and Muste, 2007).

8.2.5 Method of Propagating Uncertainty

For calculating uncertainty bands of dimensionless parameters which contained multiple sources of uncertainty (e.g. Eq. 8.4), the worst-case propagation of uncertainty *Matlab* code was used (Ridder, 2025), which attempts to determine the possible maximum and minimum values of a function via nonlinear optimization and the uncertainty band of each input.

8.2.6 Characterization of Prediction Accuracy

Error associated with the ability of a method to estimate discharge is characterized in this study using either the mean percent error (MPE) to estimate bias, or the mean absolute percent error (MAPE) to estimate overall prediction accuracy.:

$$\mathrm{MPE}\ (\%) = \frac{1}{n}\sum_{i=1}^{n}\left[\frac{Q_p - Q_m}{Q_m} \times 100\right]_i , \tag{8.6}$$

$$\mathrm{MAPE}\ (\%) = \frac{1}{n}\sum_{i=1}^{n}\left[\frac{|Q_p - Q_m|}{Q_m} \times 100\right]_i , \tag{8.7}$$

where Q_p is the predicted discharge and Q_m is the measured discharge for observation i within total observations n.

8.3 Results

8.3.1 General Head-Discharge Trends

Fig. 8.5 plots 143 head-discharge observations (see Table 8.1) from five different tilting weirs and four independent studies. The four observations of the PGV2025 study at Weir B were not included in the analysis due to observed clinging flow conditions at the time of measurement (see Fig. 8.6). Fig. 8.5 indicates the range of scale in the four datasets presented. The observed h, plotted on the horizontal axis, has been multiplied by the angle-correction k_θ term using Eq. 8.5 to incorporate the effect of θ on the discharge characteristics. A simple best-fit head-discharge rating curve is plotted here for which $C_{d\theta} = 0.56$. This value of $C_{d\theta}$ gives the indication that the discharge capacity for the field-scale tilting weirs was 10–15% less for the same value of hk_θ compared to laboratory measurements under similar h/p conditions, where $C_{d\theta}$ is expected to range from 0.62–0.67. (see Eq. 8.3).

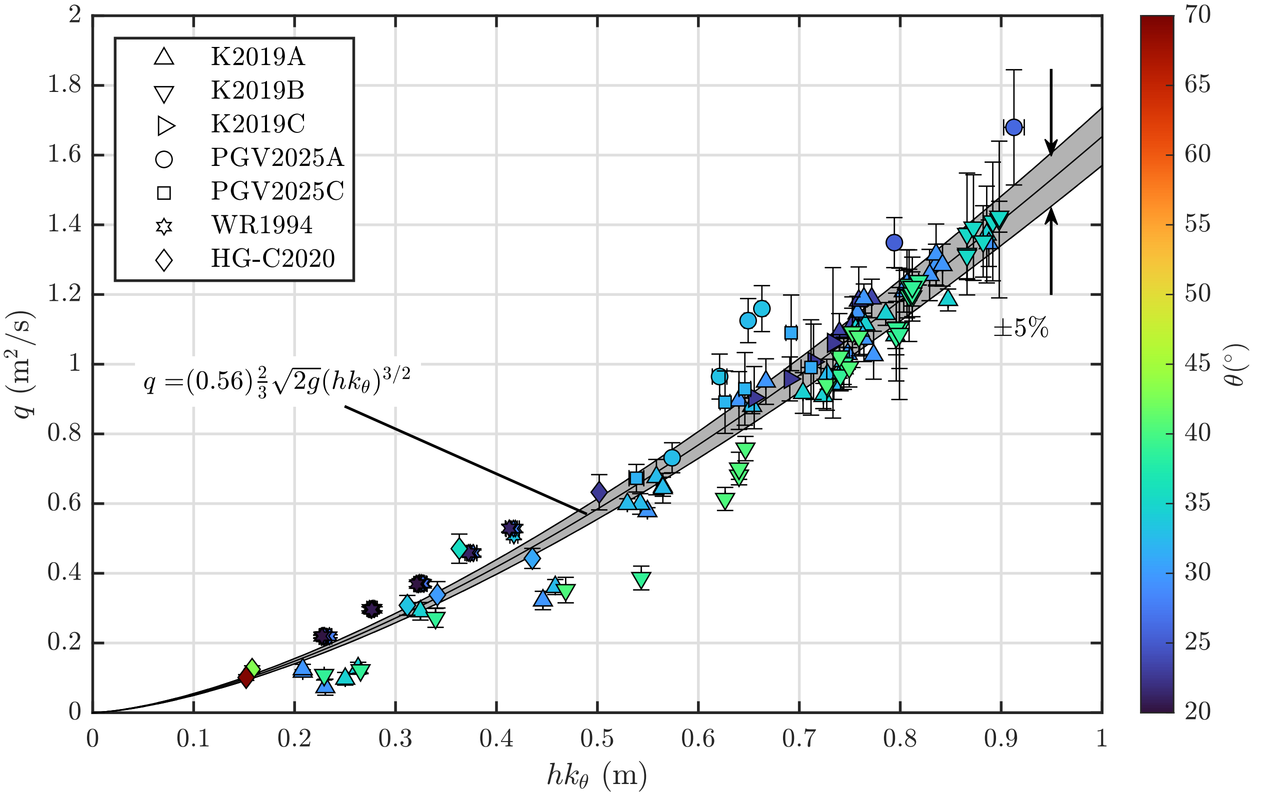

Figure 8.5: Unit discharge vs. angle-corrected head (hk_θ). A best-fit power equation with ± 5% deviation is shown to illustrate the general trend between head and discharge, as well as the variability in the relationship due to changing θ and different site conditions.

Note that here $C_{d\theta}$ is not made a function of h/p, in contrast to $\xi(h/p)$. Even with this simpler approach, it can be seen that the data generally follow the expected trend, where $q \sim h^{3/2}$. In fact, the MAPE for the 95 observations with $Fr \geq 0.1$ is a reasonable 8.4%. This highlights the robustness of stage-discharge relationships for weirs, indicating that in many cases, if h/p is not varying significantly and field conditions remain relatively stable, a constant value for $C_{d\theta}$ may suffice for a fairly good approximation of Q. However, there are also several observations where the MAPE is much larger, on the order of 20–30%. Clearly, there are some differences in the head-discharge dynamics occurring between the different weirs and factors that remain to be accounted for.

Figure 8.6: (a) Free flow at Weir A ($Q = 4905$ L/s; $h = 539$ mm; $\theta = 32.7°$) vs. (b) clinging flow at Weir B ($Q = 4425$ L/s; $h = 439$ mm; $\theta = 39.4°$) for the PGV2025 study.

8.3.2 An Inertial Threshold

Fig. 8.7a plots the dimensionless discharge coefficients and h/p ratios for the same data shown in Fig. 8.5. The function $\xi(h/p)$ is shown with a ±5% deviation band, representing the predicted discharge using Eq. 8.4. Here it can be seen that agreement between the observed field data and the expected behavior of $C_{d\theta}$ given by $\xi(h/p)$ begins to decrease with h/p. It can also be seen that data from the same study are grouped together, and often run parallel to $\xi(h/p)$ with a slight shift up or down (see in particular data for WR1994 and K2019). This gives the notion that the fundamental physics governing the discharge over a weir are the same in the field as in the laboratory, but that some additional considerations are at play in each field study that introduce variability into the discharge prediction accuracy.

Examining the increase in error at low h/p, Fig. 8.7b is helpful in revealing that there is a well-defined logistic trend between Fr (given by Eq. 8.1) and h/p, for both the tilting weir field data of the current study, and for laboratory measurements of sharp-crested weirs (Pugh et al., 2025). We can set a threshold value of Fr that is indicative of when clinging effects are likely to occur due to a lack of inertia, or when local energy losses caused by flow separation near blunt edges along the flow path of the weir become significant. This threshold value is set for the current data as $Fr = 0.1$, where data with $Fr < 0.1$ are

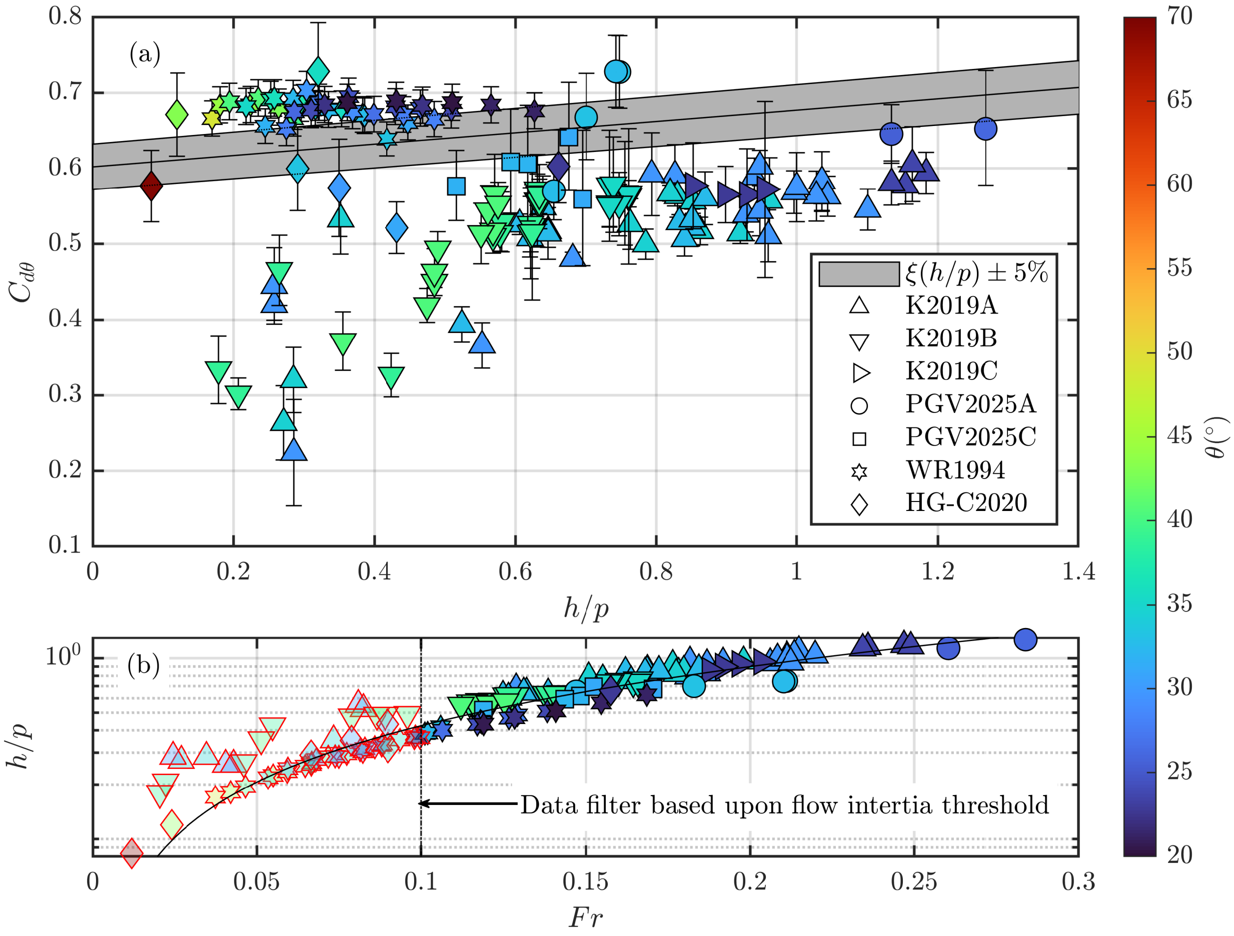

Figure 8.7: (a) Dimensionless head-discharge plot. Vertical error bars represent the 95% confidence interval. (b) Fr vs. h/p, showing logistic increase in Fr with h/p. The black curve represents a fit from experimental data for vertical sharp-crested weirs, taken from Pugh et al. (2025). Data below the chosen inertial threshold of $Fr \geq 0.1$ are made semi-transparent and outlined in red.

filtered out of our analysis of the head-discharge equation. Fig. 8.7b shows that $Fr = 0.1$ is equivalent to $h/p \approx 0.5$, which is a similar threshold to that between clinging and springing flow set by other authors (Sinclair et al., 2022; Johnson, 2000).

8.3.3 Accounting for Field Site Variability

Field conditions such as sediment accumulation, approach velocity distribution, local energy losses due to flow separation, and ventilation can all influence the discharge dynamics of prototype-scale structures. Visual comparisons of these site-specific factors are provided in Appendix B. Evidence of flow separation creating head loss along the upstream side-wall was observed at Weir B, as shown in Fig. B.2.

Turning now to a treatment of this variability between different field locations, we introduce an additional field calibration factor (k_F) to the head term so that discharge over tilting weirs in the field can be predicted as:

$$Q = \xi(h/p)\frac{2}{3}b\sqrt{2g}\left[h\Omega(\sin\theta)k_F\right]^{3/2} \rightarrow C_{d\theta F} = \frac{Q}{\left[\frac{2}{3}b\sqrt{2g}\left[h\Omega(\sin\theta)k_F\right]^{3/2}\right]}\ , \tag{8.8}$$

where k_F is calculated for each observation with $Fr \geq 0.1$ by running an optimization procedure to limit the squared error between the observed field discharge coefficient ($C_{d\theta F}$) value and that predicted by $\xi(h/p)$. k_F acts as a simple multiplicative factor to h, and therefore makes the assumption of a linear variation in the weir head between laboratory conditions and field-specific conditions.

A k_F value of unity means that the tilting weir is behaving in the field in the same way as in the laboratory. If $k_F > 1$, h in the field is less than that in the laboratory, giving the indication that clinging flow effects may be present in the field or that the nappe is not fully ventilated. If $k_F < 1$, h is slightly higher in the field to pass the same amount of q through the weir cross-section at a given value of θ as in the lab. Fig. 8.8 appears to show that as Fr increases, k_F trends towards unity. From this, we can hypothesize that effects due to field conditions are mainly due to clinging flow conditions, and/or viscous effects due to increased boundary drag, which become less prominent as Fr increases. We can also see that for each respective study, the values of k_F are closely grouped together, meaning that a representative value, $\overline{k_F}$, that minimizes the sum of squared errors between $C_{d\theta F}$ and $\xi(h/p)$ for all observations at a particular field site can be used to account for conditions unique to that measurement location. These calculated $\overline{k_F}$ values are given in Table 8.2 for each study.

It should be noted that for the WR1994, HG-C2020, and WR1994 studies, values of $\overline{k_F}$ differed by only about 5% from unity, indicating that the underlying physics governing the

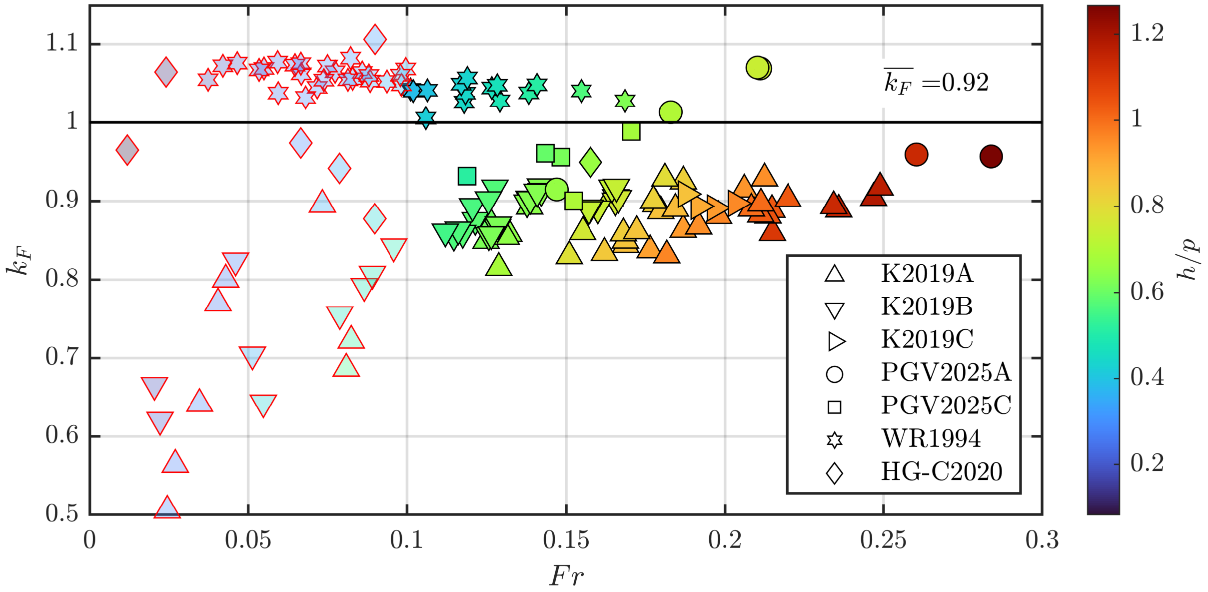

Figure 8.8: Progression of k_F term with increasing Fr. Free flow ($Fr \geq 0.1$) data shown with black outline, and excluded data shown semi-transparently with red outline. The weighted average of all free flow k_F values shown is 0.92.

tilting weir flow dynamics remain the same in the field as in the laboratory, but that small corrections are necessary to account for field-specific sites. Remarkably, the PGV2025A data did not require any correction for field conditions.

Table 8.2 shows that the $\overline{k_F}$ values for K2019 appear systematically lower than the observations from the other three studies. Overall, it appears the h values measured by Kutlu (2019) are slightly higher for the same θ and q values compared to the other three studies. This is likely due to differences in the methods used to measure h, especially since the data for K2019A/C and PGV2025A/C were taken at the same weirs. K2019 only used manual readings from a staff gauge, which are less accurate than pressure transducer water level measurements (Bureau of Reclamation, 2001). These discrepancies highlight the reality that field measurements inherently have greater uncertainty due to the dynamic nature of the observation environment. This further justifies the need for high-fidelity field instruments with a robust characterization of the various sources of uncertainty present, and for repetitive observations over multiple time periods.

Table 8.2: Description of k_F calibration values.

Weir Name	n	k_F	$\overline{k_F}$	% total
K2019A	38	0.82–0.93	0.88	40%
K2019B	26	0.86–0.92	0.89	27%
K2019C	4	0.89–0.91	0.90	4%
PGV2025A	6	0.91–1.07	1.00	6%
PGV2025C	5	0.90–0.99	0.95	5%
WR1994	15	1.01–1.06	1.04	16%
HG-C2020	1	NA	0.95	1%
	Σ **95**		$\overline{\mathbf{0.92}}$	

When applying this additional field-correction factor, k_F, as in Eq. 8.8, Fig. 8.9 shows that reliable flow measurement can be achieved for tilting weirs operating under field conditions. Here, $C_{d\theta F}$ is calculated for each study using the values of $\overline{k_F}$ found in Table 8.2. For the 95 flow observations with $Fr \geq 0.1$ ($h/p \gtrsim 0.5$), the MPE is only 0.42%, and the MAPE is 3.5% - only about 2 percentage points greater absolute error than was found for the laboratory study of tilting weirs flows (Pugh et al., 2024). With further refinement and study, it is possible that the MAPE value for field-scale tilting weirs could become as low as that for dedicated flow measurement devices such as long-throated flumes (1–2%) (Wahl et al., 2005), or high-quality ADCP measurements ($< 3\%$) (Mueller, 2016).

As a final aspect of analysis, Fig. 8.10a-c shows the distribution of stream-wise velocity in the ADCP measured cross-section for flow cases with similar Fr. The channel aspect ratios shown in the plot titles, calculated as the ratio between the channel top-width (T_w) and the hydraulic depth (A/T_w), decrease moving downstream through the system from Weir A to Weir C. This plot was created using the *QRevInt* MAP feature, which creates a spatial contour map of flow properties using a combination of the measured ADCP velocities and extrapolation algorithms. Comparing Fig. 8.10a and 8.10c, it is apparent that at Weir A, the influence of boundary friction on the flow field appears to be less than at Weir C, simply

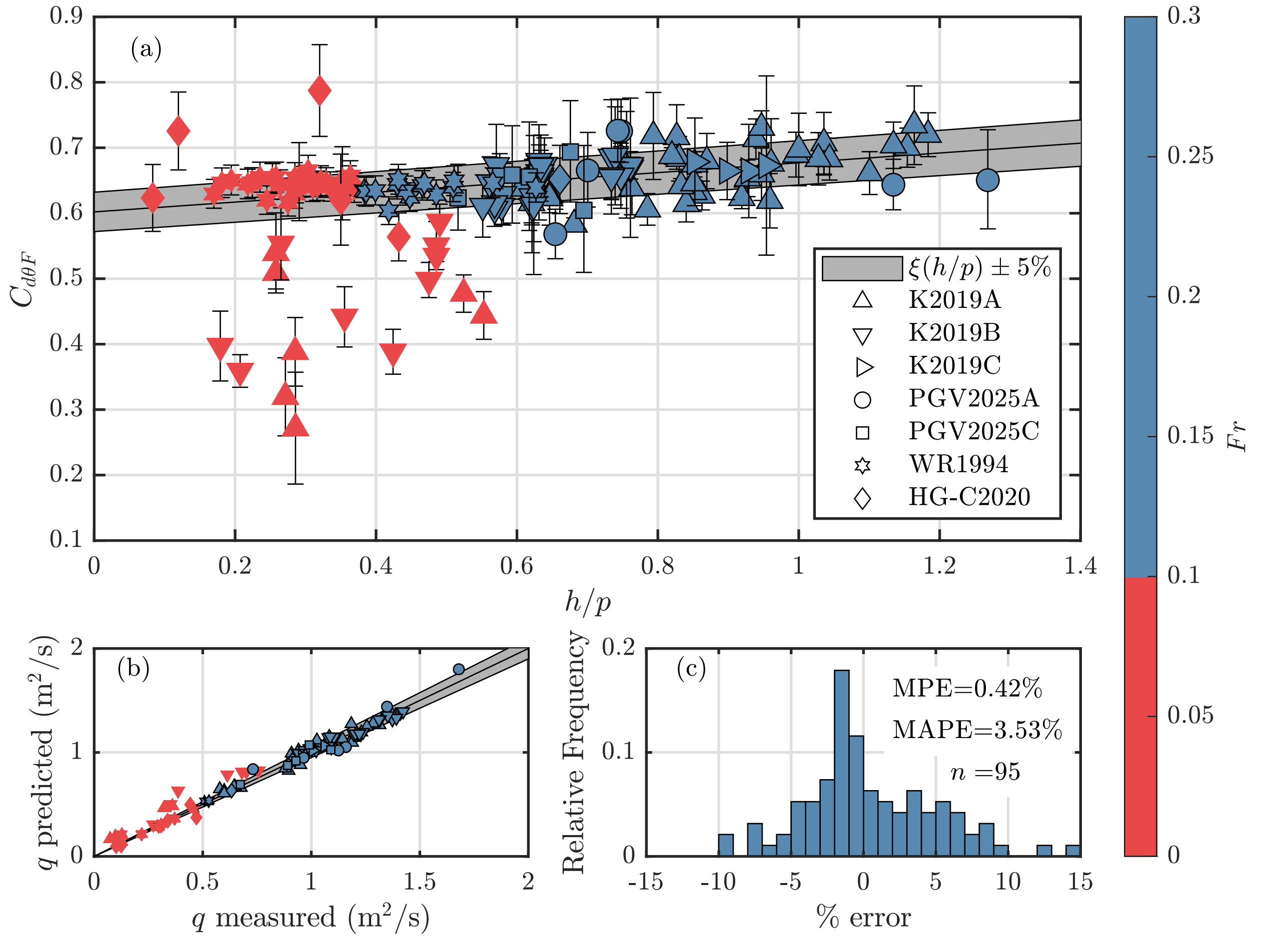

Figure 8.9: (a) Dimensionless discharge coefficient, $C_{d\theta F}$, corrected for θ and field conditions as given by Eq. 8.8, plotted against h/p. Free flow data are shown with black outline and blue fill, and excluded data are shown with red fill. (b) Values of q predicted by Eq. 8.8 against measured values. The gray patch represents ±5% deviation from the 1:1 line. (c) Relative frequency histogram of percent error for the 95 free flow observations shown in panel (b).

by virtue of the qualitative differences in the velocity contour map. This can also be seen in Fig. 8.10d when comparing the stream-wise velocity in a vertical at the mid-section of the channel. The velocity defect regarding the theoretical turbulent smooth channel logarithmic profile is greater at Weir C than it is at Weir A. Thus, the velocity profile at Weir C appears to be more inhibited by friction than at Weir A, which helps explain the lower $\overline{k_F}$ value at Weir C. As the aspect ratio grows smaller, we should expect the influence of boundary friction to grow larger, reducing the flow velocity, increasing the flow depth, and decreasing Fr.

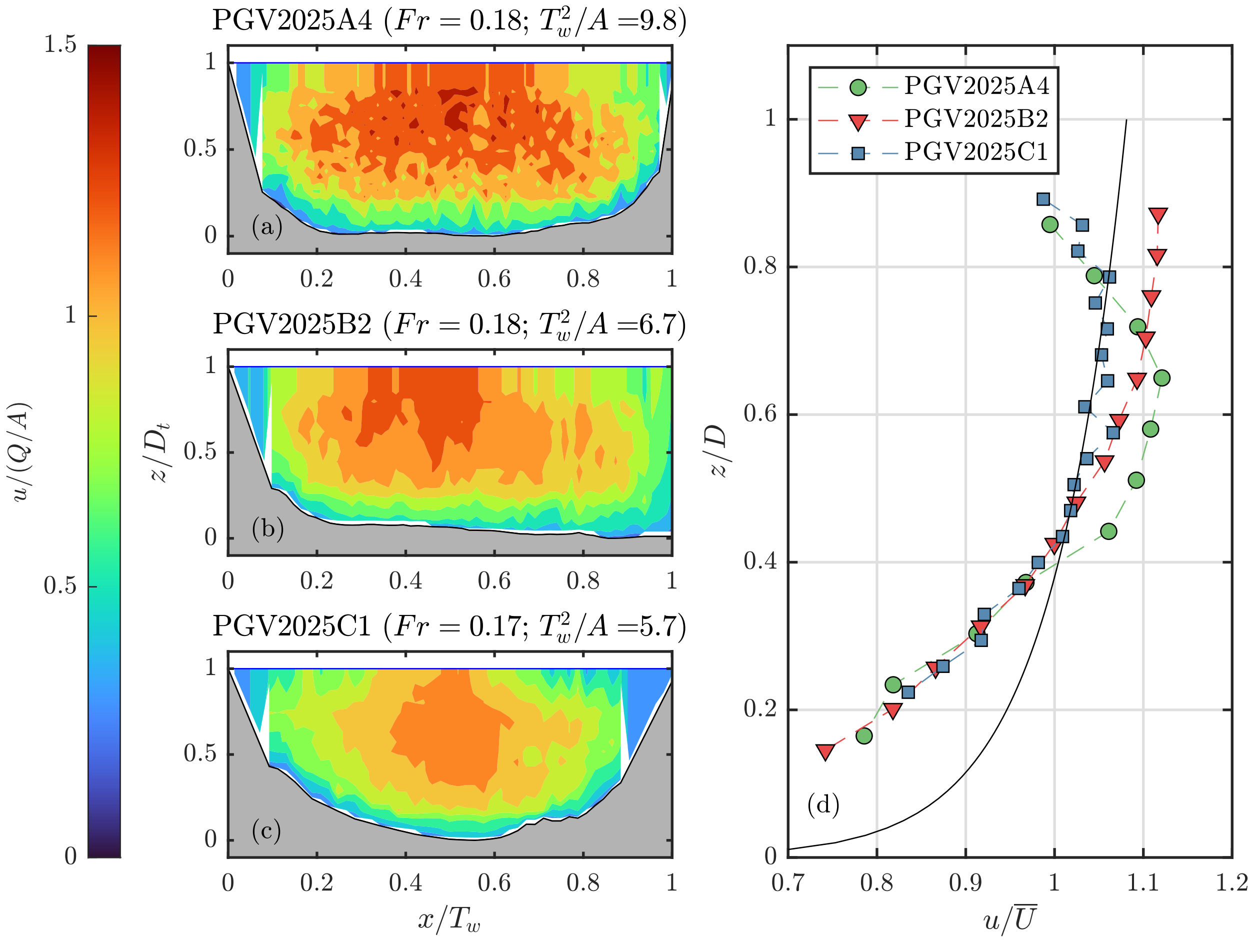

Figure 8.10: (a–c) Contour maps of dimensionless streamwise velocity and bathymetry from ADCP data at three field sites with similar Fr. Case A4: $Q = 6468$ L/s; $h = 583$ mm; $\theta = 33.1°$. Case B2: $Q = 7471$ L/s; $h = 638$ mm; $\theta = 32.1°$. Case C1: $Q = 4983$ L/s; $h = 649$ mm; $\theta = 31.2°$. D_t, T_w, and A denote the thalweg depth, top-width, and cross-section area respectively. The channel aspect ratio is given by T_w^2/A. (d) Vertical velocity profiles at mid-channel, overlaid with a theoretical smooth-channel log-law profile: $u/u_* = (1/\kappa)\ln(zu_*/\nu) + B$, with values for κ, u_*, and B taken to be 0.4, 0.05 m/s, and 5.2, respectively.

Although k_F values were not available for Weir B, it can be seen that the flow field at this site represents an intermediate case between Weirs A and C in terms of the relative amount of boundary shear influencing the velocity distribution. It should also be noted that the observed velocity profiles in the earthen canals of the current study deviate markedly from the theoretical log-law profile for a turbulent flow in a smooth channel, due to the size of the boundary layer and the wake region near the free surface (Guo and Julien, 2006). This has been recently highlighted by Fenton (2025) with implications for discharge estimation in naturally rough channels. As can be seen when comparing the approach flow conditions for each weir in Appendix B, there is some qualitative evidence for greater surface shear due to wind and Weir A, whereas the flow conditions at Weir B were found to be quiescent. Together, these findings show that field conditions for tilting weir flow measurements can at times differ significantly enough from the rectangular smooth channel laboratory conditions in which stage-discharge relationships are derived, highlighting the need for the additional correction term, k_F. As Weirs A and C in the PGV2025 study both exhibited similar instances of local energy losses caused by flow separation along the side-walls in the approach, but different mean values of k_F, we can make the tentative inference that calibration of k_F is likely influenced most significantly by channel boundary conditions affecting the velocity distribution of the approach flow. This points to the need to accurately survey channel cross-sections and characterize boundary roughness when taking field measurements. Future investigations could be made into the relationship between k_F and the kinetic energy correction factor, α. Previous studies have attempted to make similar adjustments based upon the velocity distribution (Schoder and Turner, 1929; Kolupaila et al., 1958). Other factors such as the head measurement technique, clinging flow conditions, insufficient nappe ventilation, and submergence can influence k_F as well.

In summary, the key findings from this study are:

1. Variations from idealized laboratory conditions are present in the field. For this reason, an additional calibration factor, k_F, must be included into the tilting weir discharge equation.

2. k_F is likely influenced most significantly by channel boundary roughness material and its influence on the velocity distribution of the approach flow.

3. Other non-ideal field conditions, such as surface shear, clinging flow, insufficient nappe ventilation, or localized head loss due to flow separation, also influence k_F.

4. Proper construction of the downstream structure side walls, operating with $\theta \geq 20°$, and ensuring the flow condition for measurement exceeds the inertial threshold of $Fr = 0.1$ ($h/p \approx 0.5$) all help to mitigate the non-ideal conditions affecting the nappe formation listed above.

5. k_F trends towards unity with increasing flow inertia.

6. If the head correction term $k_\theta \simeq \Omega(\sin\theta)$ is applied to h, and the range of operational h/p values is small at an individual field site, a constant value of $C_{d\theta F}$ can be calibrated to allow for a fairly good estimation of Q within $\pm \sim 8.5\%$.

7. If k_F is calibrated for a specific field site, Eq. 8.8 can be used to predict Q within $\pm 3.5\%$.

8.4 Assessment of Limitations

Although this study provides a framework by which discharge may be calculated for field-scale tilting weirs using laboratory-derived equations, we recognize additional insight is needed about the physical meaning of k_F. We use k_F to correct field-observed data to what would be expected in the laboratory; but, given the current limitations of the study it is not yet possible to separate the individual contributions of boundary roughness, flow separation, nappe ventilation, and measurement of head and weir geometry into to the nature of k_F. A more thorough analysis is needed in the future to quantify these effects separately. For example, a laboratory flume study could be completed to determine the effect of relative roughness on the reduction in discharge capacity for tilting weirs, similar to the work of Rajaratnam et al. (1976) and Davis et al. (1998) for the rectangular free overfall. Furthermore, we make the assumption that the energy losses represented by k_F are independent of flow condition. Future work could investigate the variability of k_F with Fr. Even with these unknowns, we believe there is sufficient evidence to suggest that the first-order contributing factors to k_F are boundary roughness and approach flow conditions, with second-order effects being flow separation, clinging flow, and insufficient nappe ventilation.

Additional detailed field measurements made by other researchers, with reliable estimations of the multiple sources of uncertainty in the parameters required for the flow rating procedure of tilting weirs (i.e., h, b, L, p, and Q), are encouraged by the authors to validate the field site correction procedure laid out here.

Although the presented methodology and framework has the potential to be broadly applicable, it should be noted that these data were all collected within engineered channels. It remains to be seen how this approach fares when applied to tilting weirs located within natural unlined channels where the approach features a less uniform cross-section geometry. Finally, we recognize that the operational constraints laid out (i.e., $\theta \geq 20°$ and $h/p \geq 0.5$) may be infeasible to achieve for some legacy structures (e.g. HG-C2020), which were primarily designed for management of water levels instead of flow measurement, and as such the values of h over the structures are often quite small compared to p.

8.5 Conclusions

this study has examined the viability of prototype-scale tilting weirs for flow measurement in engineering channels using a stage-discharge relationship developed from a physical modeling laboratory study. In order to account for site condition variability, we have introduced an additional field calibration factor, k_F, to the head term in the tilting weir flow equation. The average value k_F was found to vary between 0.88-1.04 for the five field measurements sites examined. This corresponds to a change in discharge capacity between -17% and $+6\%$. Considering field measurement uncertainties, reduction is more likely on the order of 5-10% for rough channels in the field compared to laboratory measurements in smooth channels. The recommended operational constraints for flow measurement using tilting weirs are: $\theta \geq 20°$ and $h/p \geq 0.5$. The primary factors causing a reduction in discharge capacity are hypothesized to be the drag induced by roughness in the approach channel. This finding is in agreement with the earlier hypothesis of Rouse (1961) in his summary of Schoder and Turner (1929):

> "Even then, Schoder has shown, variation in the velocity distribution in the channel (caused, for example, by variation in relative roughness) may easily affect the rate of discharge for a given head by as much as 5%. This is probably the reason why formulas developed from flow over weirs in short, smooth, laboratory flumes often fail to yield satisfactory results in the field."

This study has provided some preliminary evidence for this hypothesis and established a framework for using prototype-scale tilting weirs as flow measurement devices. However, more investigation is needed to understand more precisely why k_F varies, and to potentially offer prescriptive guidance on its calibration based upon specific field site characteristics, such as Manning's n. This work lays the foundation for future advancements in tilting weir design and operation, enabling system operators to enhance water management efficiency, reduce infrastructure costs, and better adapt to evolving irrigation demands.

8.6 Practical Application

Accurate flow rating of a tilting weir under field conditions can be achieved by the following process:

1. **Retrieve the dimensions of the weir plate**: L (plate length) and b (crest length). Measure L with respect to the bottom sill elevation.
2. Obtain a **measurement of the sill-referenced crest height**, p.
3. **Calculate the inclination angle** (θ) using measurements of L and p (i.e., $\theta = \sin^{-1}(p/L)$). For best accuracy, ensure $\theta \geq 20°$. **OR:**
4. Alternatively, **determine the inclination angle directly** using an inclinometer or similar device, and then determine the crest height ($p = L \sin\theta$).
5. **Estimate the value of k_θ** using Table A.1.

6. **Measure a sill-referenced flow depth**, D, in the approach channel, ideally using a stilling well and pressure transducer. Give care not to choose a gauging section that is within the zone of draw-down over the weir. Typically, an upstream distance of at least four times the maximum expected head over the structure is sufficient for the gauging section location.

7. **Determine the head over the weir**, $h = D - p$ from measurements 4 and 5, and calculate the ratio h/p. For greatest accuracy ensure $h/p \geq 0.5$.

8. **Estimate the value of** $C_{d\theta F}$ using Table A.1.

9. **Choose a first-guess value of** k_F between 0.9 and 1 based upon given site conditions. A lower k_F allows for greater energy loss compared to a smooth channel. A k_F of 1 is indicative of a straight, smooth channel.

10. **Estimate** Q using the equation:

$$Q = C_{d\theta F} \frac{2}{3} b \sqrt{2g} \left[h k_\theta k_F \right]^{3/2} \tag{8.9}$$

11. **Obtain an independent estimate of** Q, using an ADCP or nearby flow measurement structure.

12. **Adjust** k_F iteratively using an independent flow measurement until the predicted Q (Eq. 8.9 aligns closely with the observed discharge.

Chapter 9

Summary and Conclusions

9.1 Investigative Summary

This dissertation encompasses an investigation of the flow characteristics of tilting weirs using a comprehensive approach that integrates laboratory experimentation, computational simulations, and field-scale observations. The research was motivated by the limitations of existing empirical formulations for tilted weir structures and the need to develop a physically grounded, generalizable framework for their use in both research and operational settings.

A foundation in the governing equations of fluid motion was laid to frame the numerical modeling and later development of semi-empirical equations for discharge estimation. A detailed literature review explored prior work on curvilinear, rapidly-varied open channel flows, emphasizing the unique transitional nature of tilting weirs between vertical sharp-crested weirs and horizontal free overfalls. Laboratory-scale flume experiments were carried out at two separate facilities using high-resolution instrumentation, including Particle-Image Velocimetry (PIV), and Acoustic-Doppler Velocimetry (ADV). These laboratory experiments examined both bulk parameters related to calibrating a stage-discharge relationship for tilting weirs, and aspects of the two-dimensional flow field related to the dynamics of the overflowing nappe and boundary layer separation upstream of the weir. These were supplemented by Reynolds-Averaged Navier-Stokes (RANS) simulations to explore flow cases that were not available to investigation in the laboratory due to physical modeling constraints.

A new discharge equation was developed for tilting weirs that incorporates the inclination angle through a correction term k_θ, validated with over 400 experimental observations at two separate facilities. Field-scale validation of the lab-derived rating equation was conducted across multiple prototype weirs within an irrigation canal system in Northern Colorado, introducing a secondary correction term k_F to address variability in approach flow, nappe aeration, and channel geometry present. The research concludes with a practical framework that allows tilting weirs to be implemented as dual-purpose structures to regulate stage and measuring flow with accuracy and physical fidelity.

9.2 Key Findings

1. **Discharge Coefficient Decomposition:** The classical discharge coefficient for sharp-crested weirs was decomposed into its constituent physical parameters, clarifying the roles of flow contraction, kinetic energy head, and viscous energy losses in discharge prediction.

2. **Generalized Rating Equation:** A new rating equation was derived that incorporates the tilting weir inclination angle via a correction factor k_θ. The proposed formulation converges with classical theory in the limiting case of the vertical weir.

3. **Laboratory Validation:** The new equation was validated against over 400 high-resolution laboratory observations across a range of inclination angles, flow conditions, and channel geometry configuration - demonstrating consistent predictive accuracy.

4. **Flow Dynamics Characterization:** Detailed flow field measurements and RANS simulations revealed the importance of boundary layer separation, Reynolds stresses contributing to mixing of momentum, vertical pressure gradients, and energy dissipation zones in understanding the behavior of the discharge characteristics under variable θ and h/p, particularly in identifying the transition between weir and sill regimes.

5. **Definition of Operating Regimes:** Based on experimental and numerical data, the study defined thresholds for flow regimes (weir vs. sill), as well as more practically minded regimes for measurement accuracy, helping guide the deployment of tilting weirs to ensure optimal measurement accuracy.

6. **Field-Scale Application:** The proposed lab-based equation was applied to field data from multiple prototype tilting weirs, showing strong agreement when corrected using a field term k_F that accounts for real-world variability.

Overall, this dissertation work has aimed to be a significant step forward in taking a fresh look at a long-studied and ubiquitous hydraulic structure: the weir. Leveraging state-of-the-art investigative techniques towards this problem has allowed new insights to be garnered that will help usher in a new perspective on hydraulic structure design that can meet the dynamic and multi-faceted water resource needs of the 21st century, particularly regarding more accurate flow measurement and more efficient stage regulation.

9.3 Avenues for Future Work

While this dissertation offers a comprehensive framework for characterizing tilting weirs, several avenues remain open for further exploration:

- **Adaption of Discharge Equation for Submerged Conditions:** Free flow conditions will not always be guaranteed to occur in realistic field scenarios, despite the best intentions of the design engineer and system manager. Investigation into the behavior of the tilting weir discharge equation under submerged conditions is necessary to a comprehensive understanding of this topic.

- **Continued Validation and Further Exploration of Flow Field Dynamics:** Chapter 7 presented several analyses of the flow field dynamics for tilting weirs that are preliminary in nature. Further experimental and computational work is warranted to further explore the trends and initial insights presented therein, especially related to the mechanism for increased discharge capacity observed for tilting weirs, and quantifying regions of TKE dissipation.

- **Influence of Weir Blade Characteristics:** Examining variable aspects of the weir blade, such as curvature or blade roughness, on the associated components of the discharge capacity related to nappe contraction and local viscous energy losses could result in a new frontier of tilting weir design that optimizes structure functionality.

- **Comprehensive Study of k_F:** We have introduced k_F in this work as a practical correction factor to adapt laboratory-derived discharge equations to realistic field conditions. However, a physically based understanding of this term is still lacking. Further laboratory and numerical investigations are warranted to understand the hierarchy of effects influencing the behavior of k_F.

- **Management of Sediment Transport:** Investigating the nature of the tilting weir as a hydraulic control to predict near-bed dynamics influencing sediment transport, such as u_* or $-\rho\langle u'w'\rangle$. This could allow for simple measurements of h and θ to be related to an estimate of sediment transport capacity, further increasing the functionality of tilting weirs.

- **Fish Passage Around Tilting Weirs:** Similarly to an estimation of sediment transport capacity, the ability of the tilting weir to predict flow parameters related to fish passage, such as the presence of recirculation zones or the magnitude of the bulk channel velocity, could be further studied to determine the operating parameters under which fish passage is likely to occur.

- **Downstream Conditions:** Examination of the effect of h/p and θ on the channel conditions downstream of the weir, such as bed shear stress, air entrainment rate, and size of downstream recirculation zone could help inform engineering design for tilting weirs.

- **Real-Time Flow Control Integration:** The incorporation of tilting weirs into smart water infrastructure with real-time sensors and actuators presents exciting possibilities for adaptive water management.

- **Broader Geographical Application:** The discharge framework and field-related correction factor should be further tested across diverse channel geometries (natural and artificial) and geographical contexts, including arid, tropical, and mountainous environments, to assess robustness under varying hydraulic regimes.

Bibliography

M. Abou Seida and A. Quaraishi. A flow equation for submerged rectangular weirs. *Proceedings of the Institution of Civil Engineers*, 61(4):685–696, Dec. 1976. doi: 10.1680/iicep.1976.3338. URL https://www.icevirtuallibrary.com/doi/abs/10.1680/iicep.1976.3338. Publisher: ICE Publishing.

P. Ackers, W. R. White, J. A. Perkins, and A. J. M. Harrison. *Weirs and Flumes for Flow Measurement*. John Wiley & Sons, 1978. ISBN 0-471-99637-8.

R. Alboresha and U. Hatem. Effect of Height and Surface Roughness of a Broad Crested Weir on the Discharge Coefficient: Experimental Study. *IOP Conference Series: Materials Science and Engineering*, 1090(1):012087, Mar. 2021. ISSN 1757-899X. doi: 10.1088/1757-899X/1090/1/012087. URL https://dx.doi.org/10.1088/1757-899X/1090/1/012087. Publisher: IOP Publishing.

K. H. M. Ali and A. Sykes. Free-Vortex Theory Applied to Free Overfalls. *Journal of the Hydraulics Division*, 98(5):973–979, May 1972. doi: 10.1061/JYCEAJ.0003328. URL https://ascelibrary.org/doi/10.1061/JYCEAJ.0003328. Publisher: American Society of Civil Engineers.

J. D. Anderson, Jr. Ludwig Prandtl's Boundary Layer. *Physics Today*, 58(12):42–48, Dec. 2005. ISSN 0031-9228. doi: 10.1063/1.2169443. URL https://doi.org/10.1063/1.2169443.

B. F. Armaly, F. Durst, J. C. F. Pereira, and B. Schönung. Experimental and theoretical investigation of backward-facing step flow. *Journal of Fluid Mechanics*, 127:473–496, Feb. 1983. ISSN 1469-7645, 0022-1120. doi: 10.1017/S0022112083002839. URL https://www.cambridge.org/core/journals/journal-of-fluid-mechanics/article/abs/experimental-and-theoretical-investigation-of-backwardfacing-step-flow/6F4D0F1F684A7BAF899EA1CB88B09DEC. Publisher: Cambridge University Press.

H. E. Bazin. *Expériences nouvelles sur l'écoulement en déversoir [New Experiments on Weir Flow]*. Annales des ponts et chaussées [Annals of bridges and roads], Paris, France, 1898.

M. Bijankhan and V. Ferro. Dimensional analysis and stage-discharge relationship for weirs: A review. *Journal of Agricultural Engineering*, 48(1):1–11, 2017. ISSN 22396268. doi: 10.4081/jae.2017.575. URL https://doi.org/10.4081/jae.2017.575. Publisher: Page Press Publications.

M. Bijankhan and V. Ferro. Experimental Study and Numerical Simulation of Inclined Rectangular Weirs. *Journal of Irrigation and Drainage Engineering*, 144(7):04018012, July 2018. ISSN 0733-9437. doi: 10.1061/(asce)ir.1943-4774.0001325. URL https://doi.org/10.1061/(ASCE)IR.1943-4774.0001325. Publisher: American Society of Civil Engineers (ASCE).

M. Bijankhan and V. Ferro. Experimental Modeling of Submerged Pivot Weir. *Journal of Irrigation and Drainage Engineering*, 146(3):04020001, Jan. 2020. doi: 10.1061/(ASCE)IR.1943-4774.0001455. URL https://ascelibrary.org/doi/abs/10.1061/%28ASCE%29IR.1943-4774.0001455. Publisher: American Society of Civil Engineers.

M. Bos and J. Wijbenga. Passage of sediment through flumes and over weirs. *Irrigation and Drainage Systems*, 11(1):29–39, Feb. 1997. ISSN 15730654. doi: 10.1023/A:1005752711183. URL https://www.proquest.com/docview/746112801/abstract/8EF6D98422AA4C05PQ/1. Num Pages: 29-39 Place: Dordrecht, Netherlands Publisher: Springer Nature B.V.

M. G. Bos. *Discharge Measurement Structures*. International Institute for Land Reclamation and Improvement, Wageningen, The Netherlands, 1976. ISBN 9789070754150. URL https://edepot.wur.nl/64285.

M. G. Bos, J. A. Replogle, and A. J. Clemmens. *Flow measuring flumes for open channel systems*. John Wiley and Sons Inc., New York, NY, 1984.

Bureau of Reclamation. Boulder Canyon project : final reports. Bulletin 3: “Studies of Crests for Overfall Dams”. Technical Report 6: Hydraulic Investigations, United States Bureau of Reclamation, Department of the Interior, Denver, Colo, 1948. URL https://catalog.hathitrust.org/Record/001959384.

Bureau of Reclamation. *Water Measurement Manual*. U.S. Department of the Interior - Bureau of Reclamation, Denver, CO, 3rd edition, 2001. URL https://www.usbr.gov/tsc/techreferences/mands/wmm/index.htm.

J.-N. Butté and J. Pichon. Étude de la turbulence dans un écoulement à surface libre au-dessus d’une singularité en forme de marche [Study of the Turbulence in a Free-Surface Flow Over a Step-Shaped Singularity]. *La Houille Blanche*, 56(4):331–336, June 1970. ISSN 0018-6368, 1958-5551. doi: 10.1051/lhb/1970024. URL https://www.shf-lhb.org/articles/lhb/abs/1970/04/lhb1970024/lhb1970024.html. Number: 4 Publisher: EDP Sciences.

L. Castex. Quelques nouveautés sur les déversoirs pour la mesure des débits (Some novelties concerning weirs for flow measurement). *La Houille Blanche*, 1969(5):541–548, Aug. 1969. ISSN 0018-6368, 1958-5551. doi: 10.1051/lhb/1969043. URL https://www.shf-lhb.org/articles/lhb/abs/1969/05/lhb1969043/lhb1969043.html. Number: 5 Publisher: EDP Sciences.

O. Castro-Orgaz and W. H. Hager. *Non-hydrostatic free surface flows*, volume 1 of *Advances in geophysical and environmental mechanics and mathematics*. Springer, Cham, Switzerland, 2017. ISBN 978-3-319-47971-2. URL https://link.springer.com/book/10.1007/978-3-319-47971-2.

N. S. Clarke. On two-dimensional inviscid flow in a waterfall. *Journal of Fluid Mechanics*, 22(2):359–369, June 1965. ISSN 1469-7645, 0022-1120. doi: 10.1017/S0022112065000800. URL https://www.cambridge.org/core/journals/

journal-of-fluid-mechanics/article/abs/on-twodimensional-inviscid-flow-in-a-waterfall/43AFFA8B7B4B632C3071DA318AF79598. Publisher: Cambridge University Press.

A. Clemmens, T. Wahl, M. Bos, and J. Replogle. *Water measurement with flumes and weirs*. International Institute for Land Reclamation and Improvement, Wageningen, The Netherlands, 2001. ISBN 90-70754-55-X. URL https://edepot.wur.nl/82325.

A. J. Clemmens, J. A. Replogle, and Y. Reinink. Field Predictability of Flume and Weir Operating Conditions. *Journal of Hydraulic Engineering*, 116(1):102–118, Jan. 1990. ISSN 0733-9429. doi: 10.1061/(ASCE)0733-9429(1990)116:1(102). URL https://ascelibrary.org/doi/10.1061/%28ASCE%290733-9429%281990%29116%3A1%28102%29. Publisher: American Society of Civil Engineers.

A. C. Davis, B. G. S. Ellett, and R. P. Jacob. Flow Measurement in Sloping Channels with Rectangular Free Overfall. *Journal of Hydraulic Engineering*, 124(7):760–763, July 1998. ISSN 0733-9429. doi: 10.1061/(ASCE)0733-9429(1998)124:7(760). URL https://ascelibrary.org/doi/10.1061/%28ASCE%290733-9429%281998%29124%3A7%28760%29. Publisher: American Society of Civil Engineers.

A. Delafosse, M.-L. Collignon, M. Crine, and D. Toye. Estimation of the turbulent kinetic energy dissipation rate from 2D-PIV measurements in a vessel stirred by an axial Mixel TTP impeller. *Chemical Engineering Science*, 66(8):1728–1737, Apr. 2011. ISSN 0009-2509. doi: 10.1016/j.ces.2011.01.011. URL https://www.sciencedirect.com/science/article/pii/S0009250911000212.

A. Despax, J. Le Coz, D. S. Mueller, A. Hauet, B. Calmel, G. Pierrefeu, G. Naudet, B. Blanquart, and K. Pobanz. Validation of an Uncertainty Propagation Method for Moving-Boat Acoustic Doppler Current Profiler Discharge Measurements. *Water Resources Research*, 59(1), 2023. ISSN 1944-7973. doi: 10.1029/2021WR031878. URL https://onlinelibrary.wiley.com/doi/abs/10.1029/2021WR031878.

F. Dias and E. O. Tuck. Weir flows and waterfalls. *Journal of Fluid Mechanics*, 230:525–539, Sept. 1991. ISSN 1469-7645, 0022-1120. doi: 10.1017/S0022112091000885. URL https://www.cambridge.org/core/journals/journal-of-fluid-mechanics/article/abs/weir-flows-and-waterfalls/9BC0E5FC334443D1FA648F2F077A792E. Publisher: Cambridge University Press.

J. M. Díaz Lozada, C. M. García, G. Scacchi, and K. A. Oberg. Dynamic Selection of Exposure Time for Turbulent Flow Measurements. *Journal of Hydraulic Engineering*, 147(10):04021035, July 2021. ISSN 0733-9429. doi: 10.1061/(asce)hy.1943-7900.0001922. URL https://ascelibrary.org/doi/abs/10.1061/%28ASCE%29HY.1943-7900.0001922. Publisher: American Society of Civil Engineers.

J. M. Díaz Lozada, C. M. Garcia, K. Oberg, T. M. Over, and F. F. Nieto. Improvements to estimate ADCP uncertainty sources for discharge measurements. *Flow Measurement and Instrumentation*, page 102311, Jan. 2023. ISSN 0955-5986. doi: 10.1016/j.flowmeasinst.2023.102311. URL https://www.sciencedirect.com/science/article/pii/S0955598623000079.

M. Eckert. The efflux problem: how hydraulics became divorced from hydrodynamics. *Archive for History of Exact Sciences*, 78(2):127–152, Mar. 2024. ISSN 1432-0657. doi: 10.1007/s00407-023-00320-2. URL https://doi.org/10.1007/s00407-023-00320-2.

F. Engel and W. Stainsby. Velocity-of-approach factors in unified weir equations. *Proceedings of the Institution of Civil Engineers*, 9(2):165–179, Feb. 1958. doi: 10.1680/iicep.1958.2284. URL https://www.icevirtuallibrary.com/doi/abs/10.1680/iicep.1958.2284. Publisher: ICE Publishing.

J. D. Fenton. Velocity Distributions in Open Channels and the Calculation of Discharge. *Journal of Irrigation and Drainage Engineering*, 151(2):04025002, Apr. 2025. doi: 10.1061/JIDEDH.IRENG-10426. URL https://ascelibrary.org/doi/10.1061/JIDEDH.IRENG-10426. Publisher: American Society of Civil Engineers.

A. Ferrari. SPH simulation of free surface flow over a sharp-crested weir. *Advances in Water Resources*, 33(3):270–276, Mar. 2010. ISSN 0309-1708. doi: 10.1016/j.advwatres.2009.12.005. URL https://www.sciencedirect.com/science/article/pii/S0309170809002048.

V. Ferro. New Theoretical Solution of the Stage-Discharge Relationship for Sharp-Crested and Broad Weirs. *Journal of Irrigation and Drainage Engineering*, 138(3):257–265, Mar. 2012. ISSN 0733-9437. doi: 10.1061/(asce)ir.1943-4774.0000397. URL https://ascelibrary.org/doi/abs/10.1061/%28ASCE%29IR.1943-4774.0000397. Publisher: American Society of Civil Engineers (ASCE).

Floodlist News. UK – City of Leeds Installs Innovative Moveable Weirs – FloodList, Apr. 2017. URL https://floodlist.com/protection/leeds-flood-alleviation-moveable-weirs.

Flow Science, Inc. *FLOW-3D 2023R2 User Manual*. Flow Science, Inc., Santa Fe, NM, 2023. URL https://www.flow3d.com/wp-content/uploads/2020/10/FLOW-3D_HYDRO_installation_instructions.pdf.

R. Ghobadian, A. Fattahi, M. Farmanifard, and A. Ahmadi. Effect of Crest Roughness on Flow Characteristics over Circular Weirs. *Civil Engineering Infrastructures Journal*, 46(2):199–207, Dec. 2013. ISSN 2322-2093. doi: 10.7508/ceij.2013.02.007. URL https://ceij.ut.ac.ir/article_40505.html. Publisher: University of Tehran.

J. A. González-Castro and K. Lee. Uncertainty estimates in point-velocity measurements due to exposure time by functions that assimilate ISO-1088 data & statistically based on the time scale of the very-large-scale flow motions. *Flow Measurement and Instrumentation*, 71:101676, Mar. 2020. ISSN 0955-5986. doi: 10.1016/J.FLOWMEASINST.2019.101676. URL https://doi.org/10.1016/j.flowmeasinst.2019.101676. Publisher: Elsevier.

J. A. González-Castro and M. Muste. Framework for estimating uncertainty of ADCP measurements from a moving boat by standardized uncertainty analysis. *Journal of Hydraulic*

Engineering, 133(12):1390–1410, 2007. ISSN 0733-9429. URL https://doi.org/10.1061/(ASCE)0733-9429(2007)133:12(1390). Publisher: American Society of Civil Engineers.

J. A. González-Castro, J. Buzard, and M. Asif. RiverFlowUA-a Package to Estimate Total Uncertainty in ADCP Discharge Measurements by FOTSE-with an Application in Hydrometry. In *International Conference on Fluvial Hydraulics*, St. Louis, MO, USA, 2016. IAHR. URL https://doi.org/10.1201/9781315644479.

J. Guo and P. Y. Julien. Application of Modified Log-Wake Law in Open-Channels. In *Examining the Confluence of Environmental and Water Concerns*, pages 1–9, Omaha, NE, USA, 2006. ASCE. doi: 10.1061/40856(200)200. URL https://doi.org/10.1061/40856(200)200. Publisher: American Society of Civil Engineers.

W. H. Hager. Hydraulics of Plane Free Overfall. *Journal of Hydraulic Engineering*, 109(12):1683–1697, Dec. 1983. ISSN 0733-9429. doi: 10.1061/(ASCE)0733-9429(1983)109:12(1683). URL https://ascelibrary.org/doi/10.1061/%28ASCE%290733-9429%281983%29109%3A12%281683%29. Publisher: American Society of Civil Engineers.

W. H. Hager. Dammüberfälle [Dam Overfalls]. *Wasser und Boden [Water and Land]*, 46(2):33–36, 1994. ISSN 0043-0951. Place: Heidelberg Publisher: Springer.

S. M. Hajimirzaie and J. A. González-Castro. Discussion of "Experimental Modeling of Submerged Pivot Weir" by M. Bijankhan and V. Ferro. *Journal of Irrigation and Drainage Engineering*, 147(1):07020012, 2020. ISSN 0733-9437. URL https://doi.org/10.1061/(ASCE)IR.1943-4774.0001523. Publisher: American Society of Civil Engineers.

R. E. Horton. *Weir experiments, coefficients, and formulas*, volume 16. US Government Printing Office, 1906. URL https://pubs.usgs.gov/wsp/0150/report.pdf.

H. Huang. Uncertainty Model for In Situ Quality Control of Stationary ADCP Open-Channel Discharge Measurement. *Journal of Hydraulic Engineering*, 138(1):4–12, 2012. ISSN 0733-

9429. doi: 10.1061/(asce)hy.1943-7900.0000492. URL https://doi.org/10.1061/(ASCE)HY.1943-7900.0000492.

A. T. Ippen. Channel Transitions and Controls. In *Proceedings of the Fourth Hydraulics Conference*, Iowa Institute of Hydraulics Research, 1950. John Wiley and Sons Inc., New York, NY.

S. C. Jain. *Open-channel flow*. John Wiley & Sons, 2001. ISBN 0-471-35641-7. URL https://www.wiley.com/en-us/Open-Channel+Flow-p-9780471356417.

M. C. Johnson. *Discharge coefficient scale effects analysis for weirs*. Ph.D thesis, Utah State University, Dept. of Civil and Environmental Engineering, Logan, Utah, 1996. URL https://digitalcommons.usu.edu/etd/7604/. ISBN: 9780591027167.

M. C. Johnson. Discharge coefficient analysis for flat-topped and sharp-crested weirs. *Irrigation Science*, 19(3):133–137, 2000. ISSN 03427188. doi: 10.1007/s002719900009. URL https://doi.org/10.1007/s002719900009.

P. Y. Julien. *River mechanics*. Cambridge University Press, 2018. ISBN 1-108-65401-0. URL https://doi.org/10.1017/9781316107072.

P. K. Kandaswamy and H. Rouse. Characteristics of Flow over Terminal Weirs and Sills. *Journal of the Hydraulics Division*, 83(4):1345–13, Aug. 1957. doi: 10.1061/JYCEAJ.0000101. URL https://ascelibrary.org/doi/10.1061/JYCEAJ.0000101.

H. Khalili Shayan, Y. Aminpour, P. Peysokhan, and M. Bayrami. Discussion of “Extraction of the Flow Rate Equation under Free and Submerged Flow Conditions in Pivot Weirs with Different Side Contractions” by N. Sheikh Rezazadeh Nikou, M. J. Monem, and K. Safavi. *Journal of Irrigation and Drainage Engineering*, 144(4):07018008, 2018. ISSN 0733-9437. doi: 10.1061/(asce)ir.1943-4774.0001249. URL https://doi.org/10.1061/(ASCE)IR.1943-4774.0001249.

B. Khatamipour, M. R. Kavianpour, A. Khosrojerdi, and M. Ghodsi Hassanabad. Numerical Study of Flow Characteristics Over Pivot Weirs. *Journal of Hydraulic Structures*, 8(3): 17–32, Oct. 2022. ISSN 2345-413X. doi: 10.22055/jhs.2022.41058.1216. URL https://jhs.scu.ac.ir/article_18012.html. Publisher: Shahid Chamran University of Ahvaz.

H. T. Kim, S. J. Kline, and W. C. Reynolds. The production of turbulence near a smooth wall in a turbulent boundary layer. *Journal of Fluid Mechanics*, 50(1):133–160, 1971. doi: 10.1017/S0022112071002490. URL http://journals.cambridge.org/FLM.

C. E. Kindsvater and R. W. Carter. Discharge Characteristics of Rectangular Thin-Plate Weirs. *Transactions of the American Society of Civil Engineers*, 124(1):772–801, Jan. 1959. doi: 10.1061/TACEAT.0007696. URL https://ascelibrary.org/doi/10.1061/TACEAT.0007696. Publisher: American Society of Civil Engineers.

H. W. King, F. A. Nagler, A. Streiff, R. L. Parshall, W. S. Pardoe, R. E. Ballester, G. S. Williams, T. Rehbock, E. G. W. Lindquist, and C. Herschel. Discussion of “Precise Weir Measurements”. *Transactions of the American Society of Civil Engineers*, 93(1):1111–1179, Jan. 1929. doi: 10.1061/TACEAT.0004045. URL https://ascelibrary.org/doi/10.1061/TACEAT.0004045.

G. Kirkil, S. G. Constantinescu, and R. Ettema. Coherent Structures in the Flow Field around a Circular Cylinder with Scour Hole. *Journal of Hydraulic Engineering*, 134(5):572–587, May 2008. ISSN 0733-9429. doi: 10.1061/(ASCE)0733-9429(2008)134:5(572). URL https://ascelibrary.org/doi/10.1061/%28ASCE%290733-9429%282008%29134%3A5%28572%29. Publisher: American Society of Civil Engineers.

V. Kitsios, A. Sekimoto, C. Atkinson, J. A. Sillero, G. Borrell, A. G. Gungor, J. Jiménez, and J. Soria. Direct numerical simulation of a self-similar adverse pressure gradient turbulent boundary layer at the verge of separation. *Journal of Fluid Mechanics*, 829:392–419, Oct. 2017. ISSN 0022-1120, 1469-7645. doi: 10.1017/jfm.2017.549. URL https://doi.org/10.1017/jfm.2017.549.

A. N. Kolmogorov, V. Levin, J. C. R. Hunt, O. M. Phillips, and D. Williams. The local structure of turbulence in incompressible viscous fluid for very large Reynolds numbers (translated). *Proceedings of the Royal Society of London. Series A: Mathematical and Physical Sciences*, 434(1890):9–13, 1941. doi: 10.1098/rspa.1991.0075. URL https://royalsocietypublishing.org/doi/abs/10.1098/rspa.1991.0075. Publisher: Royal Society.

S. Kolupaila, R. W. Powell, J. W. Paull, and I. Oki. Discussion of "Discharge Characteristics of Rectangular Thin-Plate Weirs". *Journal of the Hydraulics Division*, 84(3):21–30, June 1958. doi: 10.1061/JYCEAJ.0000212. URL https://ascelibrary.org/doi/10.1061/JYCEAJ.0000212. Publisher: American Society of Civil Engineers.

P. K. Kundu, I. M. Cohen, and D. R. Dowling. *Fluid Mechanics*. Elsevier, 2016. URL https://doi.org/10.1016/C2012-0-00611-4.

C. Kutlu. Calibration and Uncertainty of a Head-discharge Relationship for Overshot Gates Under Field Conditions. Master's thesis, Colorado State University, United States – Colorado, 2019. URL https://mountainscholar.org/items/af5602a3-2a22-447f-a206-e411251191c0. ISBN: 9781088333204.

T. W. Lau and N. R. Afshar. Effect of Roughness on Discharge. *Journal of Civil Engineering, Science and Technology*, 4(3):29–33, 2013. URL https://publisher.unimas.my/ojs/index.php/JCEST/article/view/124.

A. Lauck. Der Uberfall uber ein Wehr [The Overfall of a Weir]. *Zeitschrift fur Angewandte Mathematik und Mechanik*, 5:1–16, 1925. URL https://doi.org/10.1002/zamm.19250050102.

K. S. Lee. Experimental analysis of the sedimentation processes by variation of standing angle in the improved-pneumatic-movable weir. *Journal of Korea Water Resources Association*, 51(9):795–802, Sept. 2018. ISSN 2799-8746, 2799-8754. doi: 10.3741/JKWRA.2018.

51.9.795. URL https://jkwra.or.kr/articles/xml/oj7E/jkwra.or.kr/articles/article/oj7E/. Publisher: Korea Water Resoureces Association.

K.-S. Lee, C.-L. Jang, N. Lee, and S. Ahn. Analysis of Flow Characteristics of the Improved-Pneumatic-Movable Weir through the Laboratory Experiments. *Journal of Korea Water Resources Association*, 47:1007–1015, Nov. 2014. doi: 10.3741/JKWRA.2014.47.11.1007. URL https://doi.org/10.3741/JKWRA.2014.47.11.1007.

K. S. Lee, C.-L. Jang, and N. Lee. Analysis of submerged flow characteristics of the improved-pneumatic-movable weir through the laboratory experiments. *Journal of Korea Water Resources Association*, 49(7):615–623, July 2016. ISSN 2799-8746, 2799-8754. doi: 10.3741/JKWRA.2016.49.7.615. URL https://jkwra.or.kr/articles/xml/q7Q7/jkwra.or.kr/articles/article/q7Q7/. Publisher: Korea Water Resoureces Association.

A. Mahdavi and N. Shahkarami. SPH Analysis of Free Surface Flow over Pivot Weirs. *KSCE Journal of Civil Engineering*, 24(4):1183–1194, Apr. 2020. ISSN 19763808. doi: 10.1007/s12205-020-0095-1. URL https://doi.org/10.1007/s12205-020-0095-1. Publisher: Springer Verlag.

J. Martínez, J. Reca, M. T. Morillas, and J. G. López. Design and Calibration of a Compound Sharp-Crested Weir. *Journal of Hydraulic Engineering*, 131(2):112–116, Feb. 2005. ISSN 0733-9429. doi: 10.1061/(ASCE)0733-9429(2005)131:2(112). URL https://ascelibrary.org/doi/10.1061/%28ASCE%290733-9429%282005%29131%3A2%28112%29. Publisher: American Society of Civil Engineers.

B. D. Mater, S. M. Schaad, and S. K. Venayagamoorthy. Relevance of the Thorpe length scale in stably stratified turbulence. *Physics of Fluids*, 25(7):076604, July 2013. ISSN 1070-6631. doi: 10.1063/1.4813809. URL https://aip.scitation.org/doi/abs/10.1063/1.4813809. Publisher: American Institute of PhysicsAIP.

G. D. Matthew. On the influence of curvature, surface tension and viscosity on flow over round-crested weirs. *Proceedings of the Institution of Civil Engineers*, 25(4):511–524, Aug. 1963. doi: 10.1680/iicep.1963.10545. URL https://www.icevirtuallibrary.com/doi/abs/10.1680/iicep.1963.10545. Publisher: ICE Publishing.

E. McLean, R. Bowles, B. Scheichl, and J.-M. Vanden-Broeck. Improved calculations of waterfalls and weir flows. *Journal of Fluid Mechanics*, 941:A27, June 2022. ISSN 0022-1120, 1469-7645. doi: 10.1017/jfm.2022.305. URL https://www.cambridge.org/core/journals/journal-of-fluid-mechanics/article/improved-calculations-of-waterfalls-and-weir-flows/EC6EFA0CC1A68486D81578B9ADC8160A.

J. S. McNown, E.-Y. Hsu, and C.-S. Yih. Applications of the Relaxation Technique in Fluid Mechanics. *Transactions of the American Society of Civil Engineers*, 120(1):650–669, Jan. 1955. doi: 10.1061/TACEAT.0007201. URL https://ascelibrary.org/doi/10.1061/TACEAT.0007201.

H. Mishra and S. K. Venayagamoorthy. New Method to Calculate Friction Velocity in Smooth Channel Flows Using Direct Numerical Simulation Data. *Journal of Hydraulic Engineering*, 150(4):04024019, July 2024a. doi: 10.1061/JHEND8.HYENG-13754. URL https://ascelibrary.org/doi/10.1061/JHEND8.HYENG-13754. Publisher: American Society of Civil Engineers.

H. Mishra and S. K. Venayagamoorthy. On the turbulent viscosity parameter C in the k– model. *Flow*, 4:E16, Jan. 2024b. ISSN 2633-4259. doi: 10.1017/flo.2024.15. URL https://www.cambridge.org/core/journals/flow/article/on-the-turbulent-viscosity-parameter-c-in-the-k-model/BE7D63A7E4C86DEA9853CD52CB6773D3.

S. Montes. *Hydraulics of open channel flow*. American Society of Civil Engineers, Baltimore, MD, July 1998. URL https://search.worldcat.org/title/39195317.

D. S. Mueller. QRev—Software for computation and quality assurance of acoustic doppler current profiler moving-boat streamflow measurements—Technical manual for version 2.8. Technical Report 2016-1068, U.S. Geological Survey, 2016. URL https://pubs.usgs.gov/publication/ofr20161068.

D. S. Mueller, C. R. Wagner, M. S. Rehmel, K. A. Oberg, and F. Rainville. *Measuring discharge with acoustic Doppler current profilers from a moving boat*. US Department of the Interior, US Geological Survey Reston, Virginia (EUA), 2013. URL https://pubs.usgs.gov/tm/3a22/.

Y. Na and P. Moin. The structure of wall-pressure fluctuations in turbulent boundary layers with adverse pressure gradient and separation. *Journal of Fluid Mechanics*, 377: 347–373, Dec. 1998. ISSN 1469-7645, 0022-1120. doi: 10.1017/S0022112098003218. URL https://doi.org/10.1017/S0022112098003218.

G. Naudet, G. Pierrefeu, T. Berthet, T. Triol, K. Delamarre, and B. Blanquart. OURSIN : OUtil de Répartition deS INcertitudes de mesure de débit par aDcp mobile. *La Houille Blanche*, 105(3-4):93–101, Oct. 2019. ISSN 0018-6368. doi: 10.1051/lhb/2019056. URL https://doi.org/10.1051/lhb/2019056.

N. S. R. Nikou, M. J. Monem, and K. Safavi. Extraction of the Flow Rate Equation under Free and Submerged Flow Conditions in Pivot Weirs with Different Side Contractions. *Journal of Irrigation and Drainage Engineering*, 142(8):04016025, Aug. 2016. ISSN 0733-9437. doi: 10.1061/(asce)ir.1943-4774.0001027. URL https://doi.org/10.1061/(ASCE)IR.1943-4774.0001027. Publisher: American Society of Civil Engineers (ASCE).

J. Pařílková, J. Říha, and Z. Zachoval. The Influence of Roughness on the Discharge Coefficient of a Broad-Crested Weir. *Journal of Hydrology and Hydromechanics*, 60(2):101–114, May 2012. doi: 10.2478/v10098-012-0009-0. URL https://sciendo.com/article/10.2478/v10098-012-0009-0.

J. A. Perry, Jr. Critical Flow Through Sharp-Edged Orifices. *Transactions of the American Society of Mechanical Engineers*, 71(7):757–763, Oct. 1949. ISSN 0097-6822. doi: 10.1115/1.4017216. URL https://doi.org/10.1115/1.4017216.

S. B. Pope. *Turbulent flows*. Cambridge University Press, 2000. ISBN 978-0-511-84053-1. URL https://doi.org/10.1017/CBO9780511840531.

M. N. S. Prakash, M. B. Ananthayya, and G. M. Kovoor. Inclined Rectangular Weir-Flow Modeling. *Earth Science India*, 4(2):57–67, 2011. URL http://earthscienceindia.info/pdfupload/tech_pdf-1325.pdf.

J. E. Pugh, T. K. Gates, and S. K. Venayagamoorthy. Refined protocols to mitigate user-induced uncertainty for ADCP moving-boat discharge measurement in irrigation canals. *Flow Measurement and Instrumentation*, 82:102060, Dec. 2021. ISSN 0955-5986. doi: 10.1016/j.flowmeasinst.2021.102060. URL https://www.sciencedirect.com/science/article/pii/S0955598621001631.

J. E. Pugh, S. K. Venayagamoorthy, T. K. Gates, C. Berni, and M. Rastello. A Novel and Enhanced Calibration of the Tilting Weir as a Flow Measurement Structure. *Journal of Hydraulic Engineering*, 150(2):04023064, Mar. 2024. doi: 10.1061/JHEND8.HYENG-13796. URL https://ascelibrary.org/doi/10.1061/JHEND8.HYENG-13796.

J. E. Pugh, S. K. Venayagamoorthy, and T. K. Gates. Demystifying the Discharge Coefficient for Flow Over Thin Weirs and Sills (Preprint). *Flow*, 2025.

S.-t. Qian, Y. Zhang, H. Xu, X.-s. Wang, J.-g. Feng, and Z.-x. Li. Effects of surface roughness on overflow discharge of embankment weirs. *Journal of Hydrodynamics*, 33(4):773–781, Aug. 2021. ISSN 1878-0342. doi: 10.1007/s42241-021-0068-y. URL https://doi.org/10.1007/s42241-021-0068-y.

G. W. Rafter. On the Flow of Water Over Dams. *Transactions of the American Society of Civil Engineers*, 44(2):220–314, Jan. 1900. doi: 10.1061/TACEAT.0001434. URL https://doi.org/10.1061/TACEAT.0001434. Publisher: American Society of Civil Engineers.

N. Rajaratnam and D. Muralidhar. Characteristics Of The Rectangular Free Overfall. *Journal of Hydraulic Research*, 6(3):233–258, Jan. 1968. ISSN 0022-1686. doi: 10.1080/00221686809500236. URL https://doi.org/10.1080/00221686809500236.

N. Rajaratnam and D. Muralidhar. Pressure And Velocity Distribution For Sharp-Crested Weirs. *Journal of Hydraulic Research*, 9(2):241–248, Jan. 1971. ISSN 0022-1686. doi: 10.1080/00221687109500348. URL https://doi.org/10.1080/00221687109500348.

N. Rajaratnam, D. Muralidhar, and S. Beltaos. Roughness Effects on Rectangular Free Overfall. *Journal of the Hydraulics Division*, 102(5):599–614, May 1976. doi: 10.1061/JYCEAJ.0004539. URL https://ascelibrary.org/doi/10.1061/JYCEAJ.0004539. Publisher: American Society of Civil Engineers.

A. S. Ramamurthy, U. S. Tim, and M. V. J. Rao. Flow Over Sharp Crested Plate Weirs. *Journal of Irrigation and Drainage Engineering*, 113(2):163–172, May 1987. ISSN 0733-9437. doi: 10.1061/(ASCE)0733-9437(1987)113:2(163). URL https://ascelibrary.org/doi/10.1061/%28ASCE%290733-9437%281987%29113%3A2%28163%29.

K. G. Ranga Raju and G. L. Asawa. Viscosity and surface tension effects on weir flow. *Journal of the Hydraulics Division*, 103(10):1227–1231, 1977. URL https://doi.org/10.1061/JYCEAJ.0004857. Publisher: American Society of Civil Engineers.

N. S. L. Rao. Theory of Weirs. In V. T. Chow, editor, *Advances in Hydroscience*, volume 10, pages 309–406. Elsevier, Jan. 1975. doi: 10.1016/B978-0-12-021810-3.50009-6. URL https://www.sciencedirect.com/science/article/pii/B9780120218103500096.

M. Rastello, M. R. Klema, A. B. Carpenter, A. Garanaik, S. K. Venayagamoorthy, T. K. Gates, and J. L. Marié. Velocity measurements in developing narrow open-channel flows with high free-stream turbulence: Acoustic Doppler Velocimetry (ADV) vs Laser Doppler Anemometry (LDA). *Flow Measurement and Instrumentation*, 87:102206, Oct. 2022. ISSN 0955-5986. doi: 10.1016/j.flowmeasinst.2022.102206. URL https://www.sciencedirect.com/science/article/pii/S0955598622000814.

J. A. Replogle. Some Observations on Irrigation Flow Measurements at the End of the Millennium. *Applied Engineering in Agriculture*, 18(1):47–, 2002. doi: 10.13031/2013.7710. URL https://elibrary.asabe.org/azdez.asp?JID=3&AID=7710&CID=aeaj2002&v=18&i=1&T=1. Publisher: American Society of Agricultural and Biological Engineers.

L. F. Richardson. *Weather Prediction by Numerical Process.* Cambridge University Press, 1922. URL https://search.worldcat.org/title/1158279354. Google-Books-ID: cWXWhffn-UokC.

B. Ridder. Worst-Case Propagation of Uncertainty, 2025. URL https://www.mathworks.com/matlabcentral/fileexchange/48139-worst-case-propagation-of-uncertainty.

H. Rouse. The distribution of hydraulic energy in weir flow with relation to spillway design. Master's thesis, Massachusetts Institute of Technology, Cambridge, Massachusets, 1932. URL http://hdl.handle.net/1721.1/72792.

H. Rouse. Discharge Characteristics of the Free Overfall. *Civil Engineering*, 6(4):257–260, 1936. URL https://archive.org/details/sim_civil-engineering-1930_1936-04_6_4/page/256/mode/2up.

H. Rouse. *Fluid mechanics for hydraulic engineers.* Engineering societies monographs. McGraw-Hill Book Company, New York, lst ed. edition, 1938. URL https://archive.org/details/in.ernet.dli.2015.15003/page/n7/mode/2up.

H. Rouse. Effects of Viscosity on Fluid Motion. In *Elementary Fluid Mechanics*, pages 167–168. John Wiley and Sons Inc., New York, NY, 1946a. URL https://archive.org/details/elementarymechan0000hunt_l7y5/page/n7/mode/2up.

H. Rouse. *Elementary Mechanics of Fluids*. John Wiley and Sons Inc., New York, NY, 1946b. URL https://archive.org/details/elementarymechan0000hunt_l7y5/page/n7/mode/2up.

H. Rouse. Pressure Variation in Accelerated Flow. In *Elementary Fluid Mechanics*, page 57. John Wiley and Sons Inc., New York, NY, 1946c. URL https://archive.org/details/elementarymechan0000hunt_l7y5/page/n7/mode/2up.

H. Rouse. Distribution of energy in regions of separation. *La Houille Blanche*, 46(3):221–246, May 1960. ISSN 0018-6368. doi: 10.1051/lhb/1960036. URL https://doi.org/10.1051/lhb/1960036. Publisher: Taylor & Francis _eprint: https://doi.org/10.1051/lhb/1960036.

H. Rouse. Flow in Open Channels. In *Fluid Mechanics for Hydraulic Engineers*, Engineering Societies Monographs, page 312. Dover Publications, New York, 2nd edition, 1961. URL https://archive.org/details/in.ernet.dli.2015.15003/page/n7/mode/2up.

H. Rouse. Discussion of "Solution of Highly Curvilinear Gravity Flows". *Journal of the Engineering Mechanics Division*, 90(5):467–470, Oct. 1964. doi: 10.1061/JMCEA3.0000552. URL https://ascelibrary.org/doi/10.1061/JMCEA3.0000552. Publisher: American Society of Civil Engineers.

H. Rouse and S. Ince. *History of hydraulics*. Dover Publications, New York, 1963. URL https://archive.org/details/historyofhydraul0000rous.

E. J. Sarginson. The influence of surface tension on weir flow. *Journal of Hydraulic Research*, 10(4):431–446, Oct. 1972. ISSN 0022-1686. doi: 10.1080/00221687209500034. URL https://doi.org/10.1080/00221687209500034.

L. Schmocker, B. R. Halldórsdóttir, and W. H. Hager. Effect of Weir Face Angles on Circular-Crested Weir Flow. *Journal of Hydraulic Engineering*, 137(6):637–643, June 2011. ISSN 1943-7900. doi: 10.1061/(ASCE)HY.1943-7900.0000346. URL https://ascelibrary.org/doi/10.1061/%28ASCE%29HY.1943-7900.0000346. Publisher: American Society of Civil Engineers.

E. W. Schoder and K. B. Turner. Precise Weir Measurements. *Transactions of the American Society of Civil Engineers*, 93(1):999–1110, Jan. 1929. doi: 10.1061/TACEAT.0004066. URL https://ascelibrary.org/doi/10.1061/TACEAT.0004066.

E. Scimemi. Sulla forma delle vene tracimanti (On the form of overflowing nappes). *L'Energia elettrica*, 7(4):293–305, Apr. 1930. ISSN 0013-7308.

D. Shubing and J. Sheng. Hydraulics of free overfall in steeply sloping rough rectangular channel: A general computational approach. *Flow Measurement and Instrumentation*, 69:101625, Oct. 2019. ISSN 0955-5986. doi: 10.1016/j.flowmeasinst.2019.101625. URL https://www.sciencedirect.com/science/article/pii/S0955598619300883.

J. M. Sinclair, S. K. Venayagamoorthy, and T. K. Gates. Some Insights on Flow over Sharp-Crested Weirs Using Computational Fluid Dynamics: Implications for Enhanced Flow Measurement. *Journal of Irrigation and Drainage Engineering*, 148(6):04022011, June 2022. ISSN 1943-4774. doi: 10.1061/(ASCE)IR.1943-4774.0001652. URL https://ascelibrary.org/doi/10.1061/%28ASCE%29IR.1943-4774.0001652.

H. Smith. *Hydraulics, the flow of water through orifices over weirs, and through open conduits and pipes.* Wiley, New York, 1886. URL https://archive.org/details/hydraulicsfloww00smitgoog/page/n5/mode/2up.

K. X. Soulis and N. Dercas. Field Calibration of Weirs Using Partial Volumetric Flow Measurements. *Journal of Irrigation and Drainage Engineering*, 138(5):481–484, May 2012. ISSN 1943-4774. doi: 10.1061/(ASCE)IR.1943-4774.0000424. URL https://ascelibrary.org/doi/10.1061/%28ASCE%29IR.1943-4774.0000424. Publisher: American Society of Civil Engineers.

M. Sterling. *A study of boundary shear stress, flow resistance and the free overfall in open channels with a circular cross-section.* Ph.D., University of Birmingham (United Kingdom), England, 1998. URL https://www.proquest.com/docview/301533266?pq-origsite=primo&parentSessionId=neQ4f%2FjdgjKeqX8U0JKtihUIspHQiX0wnbsXnM9H2nE%3D.

R. L. Street, G. Z. Watters, and J. K. Vennard. *Elementary fluid mechanics*. J. Wiley, New York, 7th ed. edition, 1996. ISBN 978-0-471-01310-5. URL https://www.wiley.com/en-us/Elementary+Fluid+Mechanics%2C+7th+Edition-p-9780471013105.

V. L. Streeter. *Fluid Mechanics*. McGraw-Hill, New York, 8th ed. edition, 1985. ISBN 978-0-07-062242-5. URL https://archive.org/details/fluidmechanics00stre_0/page/n7/mode/2up.

T. S. Strelkoff. *Irrotational Flow Over Weirs*. Ph.D., The University of Iowa, United States – Iowa, 1962. URL https://www.proquest.com/docview/302093453/citation/ED1860F3CF154A22PQ/1.

T. S. Strelkoff. Solution of Highly Curvilinear Gravity Flows. *Journal of the Engineering Mechanics Division*, 90(3):195–221, June 1964. doi: 10.1061/JMCEA3.0000487. URL https://ascelibrary.org/doi/10.1061/JMCEA3.0000487.

B. L. Stringam and T. Gill. Simplified Overshot Gate Constructed and Maintained by Irrigation Districts. *Irrigation and Drainage*, 61(5):666–672, 2012. ISSN 1531-0361. doi: 10.1002/ird.1671. URL https://onlinelibrary.wiley.com/doi/abs/10.1002/ird.1671.

T. W. Sturm. *Open Channel Hydraulics*. McGraw-Hill, New York, NY, 1 edition, 2001. URL https://archive.org/details/openchannelhydra0000stur/page/n9/mode/2up.

P. K. Swamee. Generalized Rectangular Weir Equations. *Journal of Hydraulic Engineering*, 114(8):945–949, Aug. 1988. doi: 10.1061/(ASCE)0733-9429(1988)114:8(945). URL https://ascelibrary.org/doi/abs/10.1061/%28ASCE%290733-9429%281988%29114%3A8%28945%29. Publisher: American Society of Civil Engineers.

P. K. Swamee, S. K. Pathak, and M. Ghodsian. Viscosity and Surface Tension Effects on Rectangular Weirs. *ISH Journal of Hydraulic Engineering*, 7(2):45–50, Jan. 2001. ISSN 0971-5010. doi: 10.1080/09715010.2001.10514697. URL https://doi.org/10.1080/09715010.2001.10514697. Publisher: Taylor & Francis _eprint: https://doi.org/10.1080/09715010.2001.10514697.

E. O. Tuck. The shape of free jets of water under gravity. *Journal of Fluid Mechanics*, 76 (4):625–640, Aug. 1976. ISSN 1469-7645, 0022-1120. doi: 10.1017/S0022112076000815. URL https://www.cambridge.org/core/journals/journal-of-fluid-mechanics/article/abs/shape-of-free-jets-of-water-under-gravity/952B99F9999454DA205956152855400B.

J.-M. Vanden-Broeck and J. B. Keller. Weir flows. *Journal of Fluid Mechanics*, 176: 283–293, Mar. 1987. ISSN 1469-7645, 0022-1120. doi: 10.1017/S0022112087000673. URL https://www.cambridge.org/core/journals/journal-of-fluid-mechanics/article/abs/weir-flows/D73B21DB1E7DC3CEF5FBBACE43E45553. Publisher: Cambridge University Press.

S. K. Venayagamoorthy and O. B. Fringer. On the formation and propagation of nonlinear internal boluses across a shelf break. *Journal of Fluid Mechanics*, 577: 137–159, Apr. 2007. ISSN 1469-7645, 0022-1120. doi: 10.1017/S0022112007004624. URL https://www.cambridge.org/core/journals/journal-of-fluid-mechanics/article/on-the-formation-and-propagation-of-nonlinear-internal-boluses-across-a-shelf-break/3E623A77F7ED5A4324EC091EEB92BCBD. Publisher: Cambridge University Press.

T. Wahl, J. Replogle, and M. Bos. WINFLUME—Windows-based software for the design of long-throated measuring flumes. In *4th Decennial National Irrigation Symposium*, Phoenix, Arizona, USA, 2000. URL https://www.researchgate.net/publication/228368826_WINFLUME-Windows-based_software_for_the_design_of_long-throated_measuring_flumes.

T. L. Wahl, A. J. Clemmens, J. A. Replogle, and M. G. Bos. Simplified design of flumes and weirs. *Irrigation and Drainage*, 54(2):231–247, 2005. ISSN 1531-0361. doi: 10.1002/ird.160. URL https://onlinelibrary.wiley.com/doi/abs/10.1002/ird.160.

B. T. Wahlin and J. A. Replogle. Flow Measurement Using An Overshot Gate. Technical Report 1, United States Bureau of Reclamation, Denver, CO, 1994. URL https://www.engr.colostate.edu/CIVE514/Papers%20and%20Reports/Flow%20Measurement%20Using%20an%20Overshot%20Gate.pdf.

D. C. Wilcox. Reassessment of the scale-determining equation for advanced turbulence models. *AIAA Journal*, 26(11):1299–1310, Nov. 1988. ISSN 0001-1452, 1533-385X. doi: 10.2514/3.10041. URL https://arc.aiaa.org/doi/10.2514/3.10041.

Z. Zachoval, I. Mistrová, L. Roušar, J. Šulc, and P. Zubík. Zone of flow separation at the upstream edge of a rectangular broad-crested weir / Oblast odtržení proudu na návodní hraně pravoúhlého přelivu se širokou korunou. *Journal of Hydrology and Hydromechanics*, 60(4):288–298, Nov. 2012. doi: 10.2478/v10098-012-0025-0. URL https://sciendo.com/article/10.2478/v10098-012-0025-0.

J. Zeng, M. Ansar, Z. Rakib, M. Wilsnack, and Z. Chen. Applications of Computational Fluid Dynamics to Flow Rating Development at Complex Prototype Hydraulic Structures: Case Study. *Journal of Irrigation and Drainage Engineering*, 145(12):05019009, Dec. 2019. ISSN 0733-9437. doi: 10.1061/(asce)ir.1943-4774.0001417. URL https://ascelibrary.org/doi/abs/10.1061/%28ASCE%29IR.1943-4774.0001417. Publisher: American Society of Civil Engineers (ASCE).

Y. T. Zerihun. Free-flow discharge characteristics of an overshot gate: A non-hydrostatic numerical modeling approach. *Acta hydrotechnica*, 35(63):101–115, 2022. doi: 10.15292/acta.hydro.2022.08. URL https://actahydrotechnica.fgg.uni-lj.si/en/paper/a35yz.

X. Zhang, L. Yuan, R. Peng, and Z. Chen. Hydraulic Relations for Clinging Flow of Sharp-Crested Weir. *Journal of Hydraulic Engineering*, 136(6):385–390, June 2010. ISSN 0733-9429. doi: 10.1061/(ASCE)HY.1943-7900.0000186. URL https://ascelibrary.org/doi/10.1061/%28ASCE%29HY.1943-7900.0000186. Publisher: American Society of Civil Engineers.

J. Zhou, C. Cenedese, T. Williams, M. Ball, S. K. Venayagamoorthy, and R. I. Nokes. On the propagation of gravity currents over and through a submerged array of circular cylinders. *Journal of Fluid Mechanics*, 831:394–417, 2017. doi: 10.1017/jfm.2017.604. URL https://doi.org/10.1017/jfm.2017.604. Publisher: Cambridge University Press.

Appendix A

Lookup Table

Table A.1: Values of $C_{d\theta F}$ from Eq. 8.3 for various values of h/p, and values of k_θ from Eq. 8.5 for various values of θ.

h/p	$C_{d\theta F}$	θ (°)	k_θ
0.5	0.640	20	1.069
0.55	0.643	25	1.069
0.6	0.647	30	1.067
0.65	0.651	32	1.066
0.7	0.655	34	1.065
0.75	0.658	36	1.064
0.8	0.662	38	1.062
0.85	0.666	40	1.060
0.9	0.670	42	1.059
0.95	0.673	45	1.055
1	0.677	47	1.053
1.05	0.681	49	1.050
1.1	0.685	51	1.047
1.15	0.688	53	1.045
1.2	0.692	55	1.041
1.25	0.696	57	1.038
1.3	0.700	60	1.033
1.35	0.703	62	1.030
1.4	0.707	64	1.027
1.45	0.711	66	1.023
1.5	0.715	68	1.020
1.55	0.718	70	1.017
1.6	0.722	72	1.014
1.65	0.726	75	1.010
1.7	0.730	77	1.008
1.75	0.733	79	1.006
1.8	0.737	81	1.004
1.85	0.741	83	1.002
1.9	0.745	85	1.001
1.95	0.748	87	1.000
2	0.752	90	1.000

Appendix B

Field Site Photos

To illustrate the site-specific conditions influencing discharge calibration, Appendix B Figs. B.1-B.3 show field photos of the study sites. These highlight key characteristics such as sedimentation, bed roughness, vegetation, flow separation, and blade characteristics; all of which contribute to the need for field correction factors.

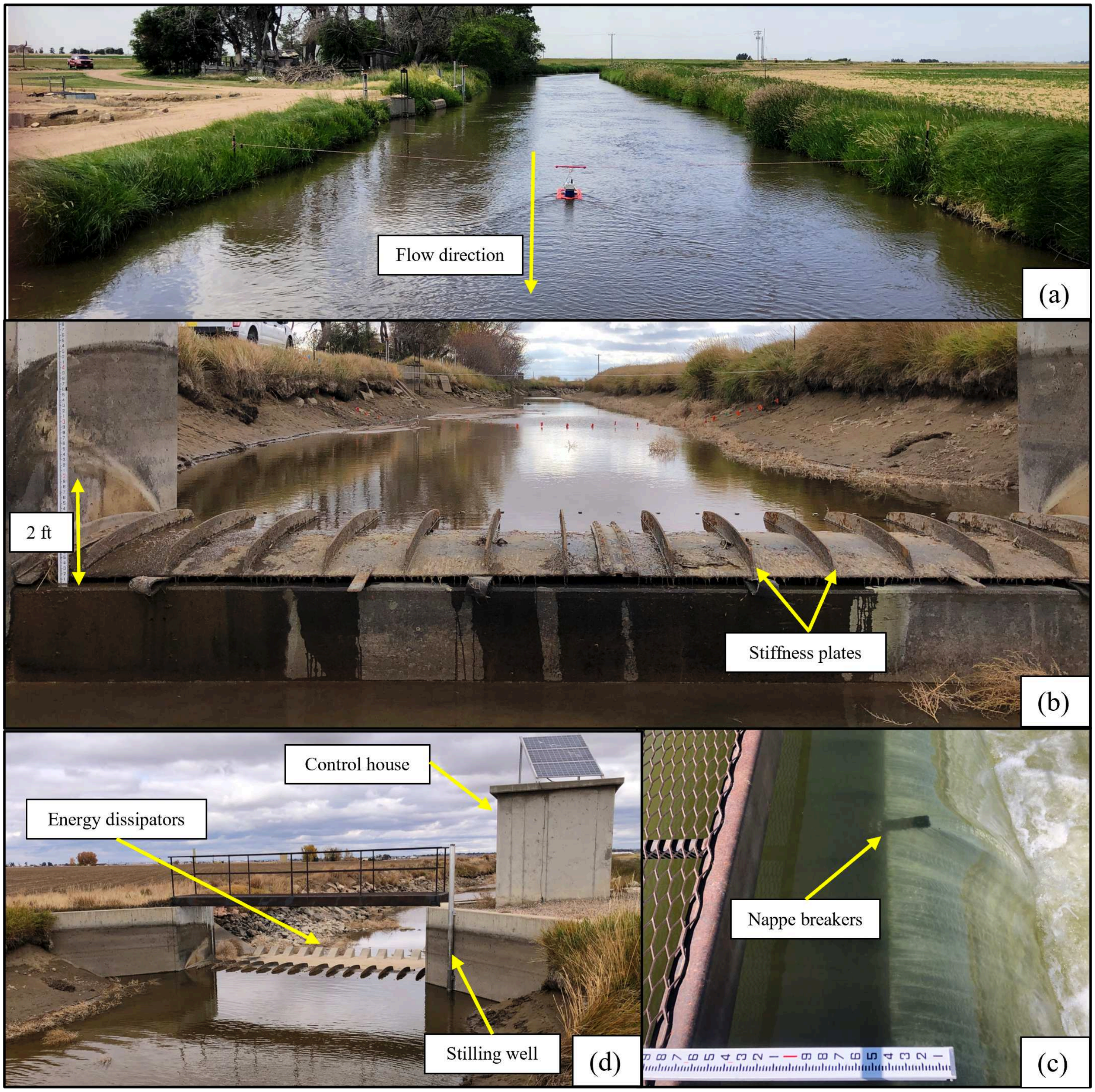

Figure B.1: Site characteristics at Weir A. a) Approach flow conditions looking upstream, with evidence of surface waves due to wind shear. b) Bed elevation drop downstream of weir. c) Nappe breakers providing aeration to flow. d) Approach to the weir looking downstream, with location of energy dissipators, stilling well, and control house shown.

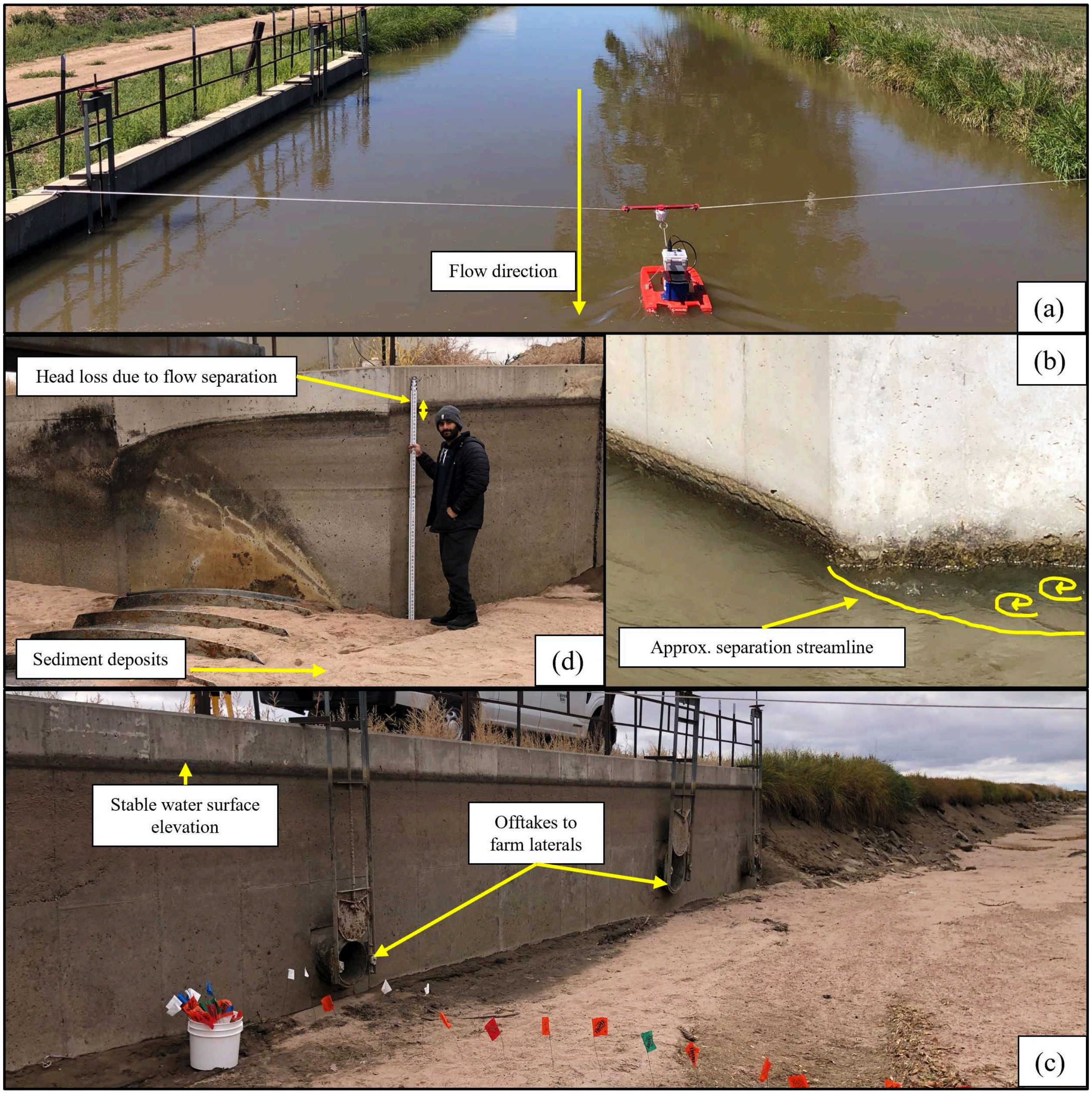

Figure B.2: Site characteristics at Weir B. a) Approach flow conditions looking upstream, evidence of quiescent flow. b) Evidence of flow separation on the left-hand-side approach. c) Sluice gates for lateral offtakes. d) Evidence of sediment deposition and head loss due to flow separation.

Figure B.3: Site characteristics at Weir C. a) Approach flow conditions looking upstream, some curvature in channel approach can be seen. b) Evidence of aeration due to divergent sidewalls downstream of crest. c) Corrosion on surface of weir blade. d) Rip-rap placement downstream of weir to dissipate energy. e) Mounted weir structure on bottom concrete sill.